UNIVERSIDAD DE CONCEPCIÓN
FACULTAD DE CIENCIAS FÍSICAS Y MATEMÁTICAS
MAGÍSTER EN ASTRONOMÍA

A 22 GHz Pseudo-correlation Water Vapor Radiometer.

Un radiómetro de vapor de agua a 22 GHz de pseudo-correlación.

Autora:

Leidy Peña Contreras

Profesor Guía:

Prof. Rodrigo Reeves

Comisión:

Dr. Rodrigo Reeves, Dr. Rafael Rodríguez, Dr. Ricardo Demarco.

Tesis para ser presentada a la Dirección de Postgrado de la Universidad de Concepción para optar al grado académico de Magíster en Astronomía

CONCEPCIÓN, CHILE
2023

Aún en los momentos adversos siempre has estado ahí. Tu confianza en mí movió el mundo, y siempre lo agradeceré. Amor grande y alegría diaria. Astrofer 28/10/11.

Acknowledgements

Quiero agradecer a todos los que hicieron posible mi Magíster y el desarrollo de mi tesis:

-A mi familia. Todos contribuyeron a que esta meta pudiera realizarse: a mi madre por sus consejos, a mi padre por ser ejemplo de vida profesional, a mi esposo e hija por esta gran aventura juntos migrando siendo un gran equipo; nena eres mi motor de vida; a mi hermano y Josy por su valiosa ayuda cuando lo necesité, a mis hermanas por ser su yayi y hacerme sentir que soy ejemplo en sus vidas, a mis abuelos y tíos en Venezuela que siempre han creído en mí, a Ramón por su confianza y, a Yulervis y su familia por darme alegría cuando lo necesité.

-A mi profesor guía, Rodrigo Reeves, por su gran apoyo y consideración. Quien me aceptó sin conocerme de antemano, sin tener la menor idea que ayudaba una familia impulsando su futuro. Gracias por su paciencia y por su humanidad ante todo.

-A los profesores Rafael Rodríguez y Roger Leiton, quienes con sus consejos, clases y hasta terapias psicológicas lograron que cada día me animara a continuar.

-A Marcela Sanhueza, secretaria del postgrado, por la empatía que siempre tuvo conmigo; y, a los profesores del Departamento, en especial a Douglas Geisler, Rodrigo Herrera, Sandro Villanova, Ricardo Demarco y Neil Nagar, quienes estuvieron en momentos claves de mi avance en el postgrado, y en casos especiales de mi situación migratoria.

-A mis compañeros y amigos del laboratorio CePIA y del Magíster, en especial énfasis a Katty quien ha sido un gran soporte de principio a fin, a David que con sus correcciones me hizo mejor estudiante, a Bodo por su alegría, a Katty Andrea por levantarme cada vez que lo necesité, a Nicol por tu magia, a Lili por tu apoyo, a Gonzalo por tu solidaridad, a Phillipe por su ayuda incondicionable, Wagner, Miguel, Ceci, Naty, Lenin, Nicolás, Ale, Brian y Claudio por la compañía y la fraternidad en este recorrido.

-A mis amigos de siempre: Elimar, Paola, Daniel, Deivis y Dexy que a pesar de la distancia y de las situaciones de la adultez, seguimos siendo pilar uno del otro en momentos de alegría, tristeza y aventura.

-Al FONDEF por su acreditación IDEA I+D 19I10300, que me permitió avanzar con confianza. Al Departamento de Astronomía, al Magíster en Astronomía y a la Universidad de Concepción, a todos sus implicados, gracias por darme esta enorme oportunidad.

-A todo aquel que se sienta directa e indirectamente parte de este logro, gracias.

A 22 GHz Pseudo-correlation Water Vapor Radiometer

Abstract

The radiation that comes from celestial objects is affected by different atmospheric components, mainly by water vapor, which is a highly variable component. This molecule can scatter, absorb and re-emit radiation and, therefore, attenuate it, affecting astronomical observations. Water vapor radiometry is an accurate method to measure the water vapor content in the atmosphere and, at altitudes < 4000 masl, the 22 GHz emission line is chosen to estimate the amount of water vapor present in the at the time of the astronomical observation. This instrument, which is under development at CePIA UdeC laboratory, will provide a notable improvement in the measurement of the line profile of water vapor and will allow atmospheric characterizations that can be validated with other instruments in places where this quantity is relevant.

The architecture designed for this project corresponds to a self-calibrated instrument, heterodine and is based on the pseudo-correlation principle. It consists of three parts: frontend, where incoming the RF signal is at a frequency range of 20 - 26 GHz; analog backend, where the RF signal is converted to a manageable frequency range of 0 - 6 GHz, called Intermediate Frequency (IF); and finally, the digital backend where the IF signal is processed in real-time through FFT, with a high spectral resolution of 62.5 kHz; the spectrum is divided intro three bands of 2 GHz each, in different Nyquist zones. Each output of the spectrometer is directly proportional to the brightness temperature of the load or the input, that provides a stable output measurement over time.

Design simulations are carried out, mathematical analyzes, data was generated to confirm the proper operation of the radiometer, commercial components are currently acquired, integration of the system is happening, simulations of the expected input signal; and, simulations of vertical water vapor recovery development techniques are used that will later lead to a prototype of a high-sensitivity tuned 22 GHz precipitable water vapor radiometer.

Contents

List of Figures

List of Tables

Chapter 1

Introduction

Water vapor is perhaps the most influential atmospheric gas from the perspective of climate and climatic processes due to its high temporal and spatial variability in the lower troposphere and its role in energy transfer Karmakar (2019); Blackwell and Chen (2009). Water vapor in the troposphere plays a critical role in radio propagation and, it's refractivity is approximately twenty times higher in the radio range than in near-infrared or optical systems Olmi (2001); Thompson et al. (2017). Therefore, observations are critical to the understanding atmospheric water vapor because it contributes to the atmospheric refractive index for astronomical observations, is highly dispersive, and can introduce errors in the length of the optical path that affects high precision observing modes.

The water molecular rotational transitions used for remote sensing of the atmosphere are at 22.235 GHz, 183.310 GHz, 448.001 GHz, and 556.936 GHz Kämpfer (2012). The water vapor profiles in the atmosphere can be retrieved from spectral measurements obtained by microwave radiometers. Radiometers are instruments that measure the electromagnetic power radiating from an object in the microwave region, the thermally radiated energy is linearly proportional to its physical temperature, if the measurement object is considered as a black body whose opacity is high; therefore, by measuring the radiated power, a radiometer provides a measure of the object's temperature through Rayleigh-Jeans approximation Kämpfer (2012). For water vapor profiling from the ground the rotational transition at 22 GHz is typically used and therefore this line can be observed even from sea level Straub et al. (2010).

Applications of passive radiometric profiling include weather forecasting and now-casting Karmakar (2019). These instruments observe the pressure broadened emission lines of water vapor rotational transitions at specific frequencies in the microwave part of the spectrum Kämpfer (2012). Radiometers observe different atmospheric layers to provide vertical profiles from a location.

Ground based instruments are characterized by long operational lifetimes while the lifetime for satellites is typically limited to less than 10 years; therefore, measurements from the ground are important for long term monitoring of water vapor and the merging of consecutive satellite missions Straub et al. (2010). Radiometers also make it possible to study the trend of atmospheric gases (particularly water vapour) and seasonal variations Haefele et al. (2009).

Hence, the use of microwave radiometers will be the method developed at CePIA (Centro Para la Instrumentación Astronómica, in Spanish) of the Department of Astronomy to

measure and retrieve atmospheric water vapor. Therefore, for the study of water vapor in the atmosphere it is necessary to address aspects associated with the Earth's atmosphere, its layers and constituents, in addition to the importance of the vertical distribution of this gas, and the rol of passive radiometry as support for astronomical observations.

1.1   Terrestrial atmosphere

The Earth's atmosphere is a gaseous layer that surrounds the planet and extends more than 100 km from its surface, it is relatively transparent to incoming solar radiation and opaque to outgoing radiation emitted from the Earth's surface Wallace and Hobbs (2006). It is made up of a wide variety of gases, and each gas characteristically interacts with electromagnetic radiation at a given frequency. Therefore, this relationship constitutes the physical basis by which the atmosphere can be characterized by observing radiation of different frequencies that have been emitted and transmitted through the atmosphere Blackwell and Chen (2009). It is a relatively stable mixture of several types of gases from different origins, it has about $5.15x10^{15}$ tons held to the planet by gravitational attraction Mohanakumar (2008).

Atmospheric density decreases with altitude due to the Earth's gravitational field. Assuming a condition of static equilibrium, the relationship between density and pressure as a function of altitude can be expressed by the following differential equation:

$$dp = -g\rho dz \tag{1.1}$$

where p and ρ are the pressure and density respectively, at altitude z measured vertically upward from the surface, equation (1.1) is called *the barometric law* Brekke (2012). The ideal gas equation $pV = nRT$ can be used to relate the density of an ideal gas of molecular weight M_r to its temperature and pressure:

$$\rho = \frac{M_r p}{RT} \tag{1.2}$$

where R is the gas constant per mole and T is the temperature. Equation (1.1) can be expressed as:

$$\frac{dp}{p} = -\frac{dz}{H} \tag{1.3}$$

Therefore, it is integrated to find the pressure p at altitude z, leaving:

$$p = p_0 exp\left\{-\int_0^z \frac{dz}{H}\right\} \tag{1.4}$$

where p_0 is the surface pressure and $H = RT/M_r g$ is known as the scale height, which is the increase in altitude needed to reduce the pressure by a factor of e. In the troposphere, H typically varies between 6 km at T=210 K and 8.5 km at T=290 K Blackwell and Chen (2009). On the Chajnantor Plateau the scale height was found to be on average $H = 1537m$ Cortés et al. (2020)

The temperature between the ground and 100 km altitude varies quite markedly, and, above 100 km, the temperature increases drastically, and the molecules dissociate due to solar radiation so that the molecular mass decreases. For a constant temperature and mean
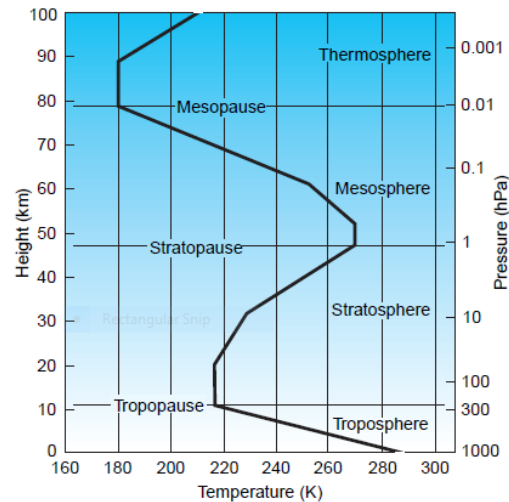
FIGURE 1.1. A typical mid-latitude vertical temperature profile, the central black line distinguishes this temperature profile variation. The different atmospheric layers are shown. In addition, the decrease in pressure with respect to height is denoted. Source: Wallace and Hobbs (2006).

mass of the molecules; the mass density will decrease exponentially at the same rate as the pressure. For an isothermal atmosphere with constant molecular mass, the mass density is given by equation (1.4) and the scale height is constant as long as the acceleration of gravity is constant Brekke (2012).

1.1.1 Atmospheric layers

Because the pressure and density of the Earth's atmosphere can vary substantially in the vertical dimension, that is, the atmospheric density decreases with altitude due to the Earth's gravitational field, just like the pressure Blackwell and Chen (2009), it is helpful to define a standard structure for the atmosphere, which is expected to change as a function of height.

The Earth's atmosphere can be classified into four layers according to the thermal and chemical phenomena. These layers are (in increasing altitude) the troposphere, the stratosphere, the mesosphere, and the thermosphere. The boundaries between each layer are generally not well defined but show specific characteristics Blackwell and Chen (2009), such as the temperature variation dependent on height, as shown in figure (1.1).

About 90% of the Earth's atmosphere is within the troposphere, a thin layer about 15 km of thickness Woodhouse (2017), and is characterized by a constant decrease in temperature, it starts at about 290 K at the ground and reaches a minimum of 215 K at the tropopause Brekke (2012). However, within it, it can find thin layers in which the temperature increases with height (that is, the rate of fall for temperature is negative), which is called temperature inversion Wallace and Hobbs (2006).

Vertical heat transfer in the troposphere consists mainly of thermal radiation emitted from the Earth's surface Kämpfer (2012). The temperature in this layer of the atmosphere

drops fairly monotonically until the tropopause, this is due to the fact that the infrared radiation from the ground, which is absorbed in the atmosphere, is fairly constant because the surface temperature of the globe is constant, and therefore heat expands in the atmosphere in radial directions, the heat will then be distributed in larger volumes and thus the temperature must decrease Brekke (2012). The main physical processes at and near the tropopause are radiation, convection, turbulence, advection, and vertical convergence Mölders and Kramm (2014).

The troposphere contains 99% of the water vapor in the atmosphere. However, the water vapor content decreases rapidly with altitude Mohanakumar (2008), furthermore the water vapor at this altitude influences the size and composition of the hygroscopic particles, aerosols and in the heterogeneous reactions of gases with aerosols Kämpfer (2012) .

Above the tropopause is the stratosphere, which extends to an altitude of about 40 km, and the temperature rises to a maximum near 280 K, until the stratopause Brekke (2012). It is characterized by high concentrations of ozone, therefore, heating by absorption of ultraviolet solar radiation due to ozone molecules is responsible for the temperature increase in the stratopause Brasseur (2013); since O_2 photodissociates, resulting in atomic oxygen and very rapidly recombines with molecular oxygen giving rise to ozone O_3. These "recombination type" chemical reactions are exothermic and release so much heat that they transform the vertical stratification of the atmosphere into the stratosphere, here the content of water vapor in this layer is very low Ménard et al. (2020).

On the other hand, in the stratosphere, the distribution of water vapor is due to dry air entering through the tropical tropopause and a source of water vapor from methane oxidation in the upper stratosphere Mohanakumar (2008), each CH_4 molecule entering the stratosphere is oxidized or photodissociated, resulting in the production of two H_2O molecules Le Texier et al. (1988); Chabrillat and Fonteyn (2003). VMR is the mixing ratio of a given volume of a gas in the atmosphere expressed in ppmv units (parts per million volume). Methane oxidation is the dominant VMR formation mechanism of mean atmospheric water vapor leading to a positive vertical VMR gradient throughout the stratosphere Straub et al. (2011). This VMR relationship is generally used in the comparison of time series of atmospheric gases at different altitude levels that show a similar evolution and can be captured by ground-based and satellite-based instruments.

The mesosphere extends from approximately 40 to 80 km and is characterized by a decreasing temperature with altitude. The decrease in atmospheric temperature in the mesosphere is the result of ozone depletion and increased cooling rates of CO_2 infrared radiation Brasseur (2013); this temperature may be as low as 160 K or even lower at occasions Brekke (2012). Photodissociation due to solar Lyman absorption is the relevant sink of water vapor in the middle atmosphere, leading to a negative vertical VMR gradient throughout the mesosphere Straub et al. (2011).

Finally, the thermosphere, which is the upper layer, goes from mesopause to local interplanetary space. In this layer, the temperature rises again due to the interaction of high-energy radiation from the sun with the dissociation of diatomic nitrogen and oxygen molecules

(photodissociation and photoionization) Wallace and Hobbs (2006).

Above 100 km the mixing of air parcels is dominated by molecular diffusion. Gas molecules are influenced by gravity, leading to lighter molecules in the outer layer and heavier molecules closer to the Earth, consequently the composition of the atmosphere beyond the middle atmosphere is not uniform and is also known as heterosphere, unlike the atmosphere below 100 km, where the gas constituents mix completely into a homogeneous gas, this being the homosphere. Mohanakumar (2008). Temperature can reach more than 1000 K at 400 km, above this region, the temperature is fairly constant with respect to height Brekke (2012).

1.1.2 Atmospheric constituents

The atmosphere is made up of different gases, and the concentrations of these gases vary in time and space. In table (1.1), the composition of the atmosphere below 100 km is shown; it can be seen that the major constituents are nitrogen, oxygen, and argon, which make up 99.96% of the total atmospheric composition Mohanakumar (2008). In the same way, figure (1.2) show the distribution and the variation of some relevant atmospheric gases as a function of height.

TABLE 1.1. Constant and variable concentrations of atmospheric constituents. Note that in addition to gases, the atmosphere is composed of aerosols (particles in suspension), dust and possible hygrometers (drops, snow, hail, etc.). Source: Mohanakumar (2008).

Constituent	Percentage by volume	Molecular weight ($g \cdot mol^{-1}$)
(A) Constant concentrations		
Nitrogen (N_2)	78.08	28.01
Oxygen (O_2)	20.95	32
Argon (Ar)	0.933	39.95
Carbon dioxide (CO_2)	0.033	44.01
Neon (Ne)	$18.2x10^{-4}$	20.18
Helium (He)	$5.2x10^{-4}$	4.02
Kryton (Kr)	$1.1x10^{-4}$	83.8
Xenon (Xe)	$0.089x10^{-4}$	131.29
Hidrogen (H_2)	$0.5x10^{-4}$	2.02
Methane (CH_4)	$1.5x10^{-4}$	16.04
Nitrous oxide (N_2O)	$0.27x10^{-4}$	44.01
Carbon monoxide(CO)	$0.19x10^{-4}$	28.01
(B) Variable concentrations		
Water vapor (H_2O)	0-4	18.02
Ozone (O_3)	$0 - 4x10^{-4}$	48.02
Ammonia (NH_4)	$0.004x10^{-4}$	17.02
Sulphur dioxide (SO_2)	$0.001x10^{-4}$	64.06
Nitrogen dioxide (NO_2)	$0.001x10^{-4}$	46.05
Other gases	Trace amounts	
Aerosol, dust, gases	Highly variable	

Electromagnetic radiation at microwave frequencies interacts with suspended atmospheric molecules, particularly oxygen and water vapor Blackwell and Chen (2009). At the ground the atmosphere is composed of close to 80% N_2 and 20% O_2, while the contribution from other gases is less than 1%. This mixture holds all the way up to about 100 km. Above 100 km, molecules start to dissociate, the latter reflecting the fact that the different species have
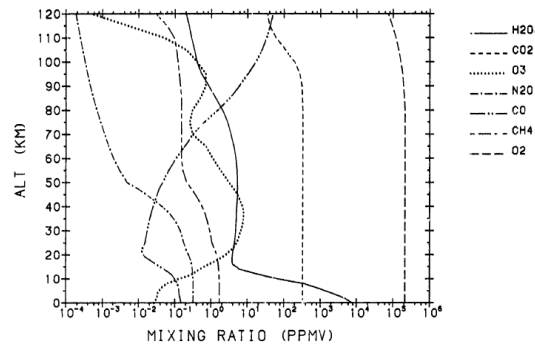
FIGURE 1.2. Standard Model Atmosphere Profiles. Here it is shown the characterization of the water vapor, ozone and other gases retrieval in specific vertical distribution, they are expressed in volume mixing ratio (ppmv), defined as the number density of the gas divided by the total number density of air. Note that in the atmospheric water vapor, the decrease of this gas with height; it is also observed that a large part is concentrated in the troposphere, in the first 10 km. For ozone, it is observed that its highest concentration (around 90%) is found in the stratosphere, between 10-50 km. Source: Anderson et al. (1986).
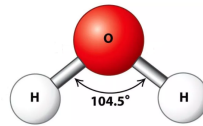
FIGURE 1.3. Water molecule. Its dipolar structure is shown with two positively charged hydrogen atoms covalently bonded to one negatively charged oxygen atom. Source: https://alevelbiology.co.uk/notes/water-structure-properties/

different scale heights or barometric heights Brekke (2012).

Water vapor is the most important variable in terms of its quantity, which can vary between 0% in cold regions and 4% in dry regions; this gas shows a decrease with height, almost all the content of water vapor is found in the troposphere, being the largest contributor to atmospheric microwave opacity Mohanakumar (2008).

1.1.3   The water vapor molecule

The water molecule is made up of two hydrogen atoms and one oxygen atom; oxygen is located at one vertex of a 104,5° angle formed with the hydrogens, thus are in equivalent positions, figure (1.3). This molecule has a very small moment of inertia on rotation giving rise to combined vibrational-rotational spectra in the vapor containing many absorption lines Hall and Dowling (1967).

These vibratory movements correspond to contractions or extensions of equal or different amounts of the distance between the hydrogen atoms and the oxygen atom. Moreover, the bending movements correspond to the angle variation between the hydrogen atoms. Hence, vibrations of water molecules occur in three modes, including symmetric stretching ν_1, asymmetric stretching ν_3 and bending ν_2 (figure 1.4) Braun and Smirnov (1993). The energy for these vibrations is obtained by absorption of radiation and, vibrations are most intense at wavelengths matching the specific energy requirements of these motions. These wavelengths can be recognized as peaks in the absorption spectrum of pure water (figure 1.5) Stomp et al. (2007).
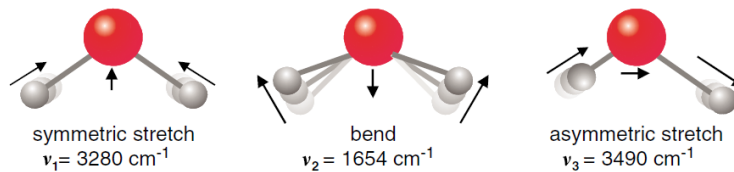
FIGURE 1.4. The simple vibrational modes of the water molecule. From left to right: symmetric stretch, bend and asymmetric stretch. The atoms move in the directions indicated by arrows. Source: Stomp et al. (2007)

.
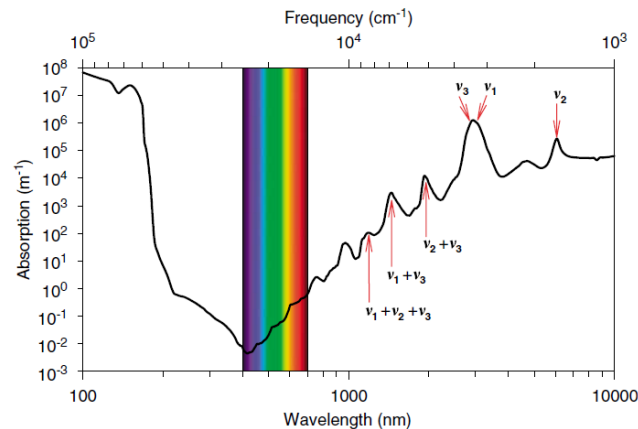
FIGURE 1.5. Absorption spectrum of pure water. Peaks in the absorption spectrum correspond to the fundamental frequencies and higher harmonics of the vibrations of the water molecules. Sources: Segelstein (1981); Hale and Querry (1973); Pope and Fry (1997); Stomp et al. (2007)

The rotation spectrum of water vapor extends into the microwave region. Water has a broad absorption spectrum in the microwave region, which has been explained in terms of changes in the hydrogen bond network giving rise to a broad, featureless, microwave spectrum Kaatze et al. (2002). The rotation is done around the center of mass of the molecule and the axis must allow the conservation of angular momentum, in simple cases this can be recognized through symmetry, as with the water molecule.

A pure rotation spectrum can only arise when the molecule possesses a permanent electric dipole moment. Since molecular bond lengths remain constant in pure rotation, the magnitude of a molecule's dipole cannot change. However, since the electric dipole is a vector quantity (it has size and direction), rotation can cause a permanent dipole to change direction and therefore observe its spectra.

The molecular dipole is the presence of charge imbalance in a molecule. If a molecule has a permanent dipole, which lies along the principal axis of rotation, then the molecule will not have a rotation spectrum like that of a water molecule. However, it may take time to determine where the dipole came from and what it is. The lack of a uniform charge distribution leads to a potential difference between molecule regions.

A simple example of a molecule with a permanent molecular dipole is water, where the vector sum of the bond dipole moments does not equal 0. This molecular dipole is permanent so it could appear in pure rotational spectroscopy. However, since this dipole vector contains the central axis of rotation of the molecule, the molecular dipole remains static while

the molecule rotates.

In pure rotational spectroscopy for a simple diatomic molecule, the energy levels – as displayed below – are given by $E_j = BJ(J+1)$, where J is the rotational quantum number, B is the rotational constant for the particular molecule given by $B = h^2/8\pi^2 I$ with the unit of Joules, where I is the moment of inertia, given by $I = \mu r^2$, where r is the bond length of this particular diatomic molecule and μ is the reduced mass, given by $\mu = m_1 m_2/m_1 + m_2$

Most energy level transitions in spectroscopy come with selection rules. These rules prevent specific transitions from occurring, though they can often be broken. In pure rotational spectroscopy, the selection rule is $\Delta J = \pm 1$.

A rotational spectrum would have the following appearance, figure (1.6). Each line corresponds to a transition between energy levels, as shown. Notice that there are no lines for, for example, $J = 0$ to $J = 2$, etc. This is because the pure rotation spectrum obeys the selection rule $\Delta J = \pm 1$. The energy gap between each level increases by $2B$ as the energy levels we consider increase by $J = 1$. This leads to the line spacing of $2B$ in the spectrum. Each transition has an energy value of $2B$ more than the previous transition Liverpool (2023).
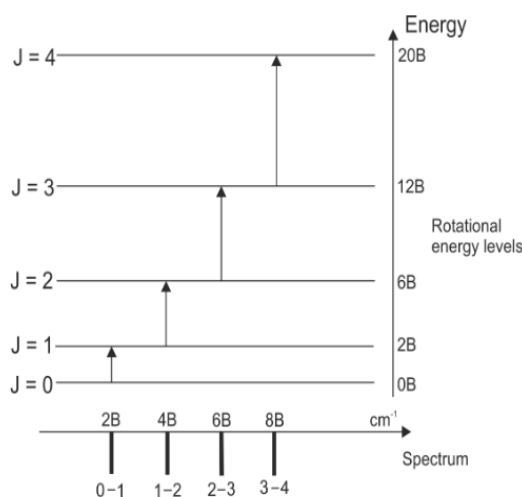
FIGURE 1.6. A rotational spectrum. Source: https://www.chemtube3d.com/rotational-spectroscopy-introduction/

If there is no interaction between molecules, we consider quantum states of being the products of states of isolated molecules; therefore, the dipole moments of different molecules are not correlated, and the orientation of a molecule concerning a set of axes fixed in space can be specified by the three Euler angles, θ, ϕ, and x (they constitute a set of three angular coordinates that serve to specify the orientation of a reference system with orthogonal axes, usually mobile, to another reference system with orthogonal axes, typically fixed). Rotational wave functions are symmetric or antimetric for a rotation of $180°$ about a principal axis of the molecule.

So, suppose a $180°$ rotation about one of a molecule's principal axes has the sole effect of exchanging two equivalent nuclei. In that case, that axis must contain the electric dipole moment (if the molecule has one). Hence, the statistical weights due to the nuclear spin of

the two states in a radiating transition are equal.

The motion of the particles (nuclei and electrons)constituting a molecule can be described by a wave function ψ that depends on the coordinates of all the particles. The Born-Oppenheimer approximation is implemented then considering the electronic motion with internuclear distances as parameters and the motion of the nuclei with the prespecified electronic state; therefore, the wave function is separated into an electronic part and a part for vibration, rotation, and nuclear spin: $\psi = \psi_{elec}\psi_{vib-rot-nuc}$; and, in simple molecules such as those that make up the atmosphere, the vibrational energy levels are generally more widely spaced than the rotational energies, therefore separating ψ_{vib} from ψ_{rot} and ψ_{nuc} is appropriate. Then the rotational energy eigenvalue problem can be solved for a prespecified vibrational state and vice versa.

In the H_2O molecule, the oxygen nucleus is at the vertex of a almost $105°$ angle formed with the hydrogen nuclei in equivalent positions. Protons obey the Fermi-Dirac statistics, so the total wave function ψ; must be antimetric concerning the exchange of hydrogen nuclei. This operation involves a $180°$ rotation around the axis with an intermediate moment of inertia. The ground state electronic wave function is symmetric.

Consider the symmetry properties of ψ_{nuc} for $H_2^{16}0$. The $^{16}0$ nucleus has spin zero. Each hydrogen nucleus has a spin quantum number $= 1/2$. The component of the spin operator along a fixed axis in space has an eigenvalue $\pm\frac{1}{2}\hbar$. Thus, the space of possible wave functions has four dimensions: 1) the spin symmetric wave function subspace is three-dimensional and divided by three wave functions, and 2) the wave function subspace of antisymmetric spin is one-dimensional.

To obtain a ψ wave function, which is antimetric for the exchange of hydrogen nuclei, the symmetric ψ_{nuc}; it must be combined with the ψ_{rot} (which is the wave function for an asymmetric rotor) which are antisymmetric to the axis with an intermediate moment of inertia; and, the antisymmetric ψ_{nuc} is combined with rotational states that are symmetric about one of the axes that have the same parity.

Due to the small moments of inertia of water vapor, most of its strong rotational transitions are at submillimeter and infrared wavelengths. The two important microwave transitions are at 22.235 and 183.310 GHz Janssen (1994).

Therefore, if we have an axis of the molecule fixed in space and we consider the orthogonality properties of the functions in such a way that the dipole moment is different from zero, in addition to having the asymmetric rotor function, then a rotation is possible wave function for all molecular shapes that require it.

1.2   Importance of water vapor

Water vapor plays a crucial role in atmospheric processes through its radiative, chemical and dynamical properties Kämpfer (2012). From the study of mathematical models that involve the retrievals of atmospheric parameters, it is possible to characterize the layers of the

atmosphere and evaluate its characteristics.

Water vapor to being extremely important in the Earth's radiative budget as it is the most important natural greenhouse gas in the troposphere Straub et al. (2011); Deuber et al. (2005); Müller et al. (2008), it accounts for about 60% of this natural greenhouse effect, and it provides the most significant positive feedback in model projections of climate change Solomon et al. (2007).

It is extremely important in the processes of radiative absorption and emission in the atmosphere. Relatively small amounts of water vapor can produce large variations in climate, Mohanakumar (2008), therefore any disturbance in its abundance can have different impacts Mote et al. (1996).

It is a source of clouds and precipitation, which directly affect the climate Kämpfer (2012), no projection of climate change is complete without considering the effects of future changes in water vapour Morland et al. (2006). Decades-long variations in water vapor in some layers are still puzzling Sherwood et al. (2010).

The variability in water vapor in the troposphere is closely tied to changes in surface temperatures and is affected by the temperature of the underlying ocean. There is a connection between sea surface temperature and temperature in the lower stratosphere and thus in the water vapor content Rosenlof and Reid (2008).

Chemically, water vapor is an important source of the hydroxyl radical, the main oxidant in the troposphere that can react with most pollutants Kämpfer et al. (2003). Water vapor is also a valuable indicator of atmospheric motion due to its long chemical life Kämpfer et al. (2003); Straub et al. (2011); Tschanz et al. (2013); Brasseur et al. (1999) in the stratosphere and mesosphere Straub et al. (2011); Tschanz et al. (2013); Brasseur et al. (1999). This allows studying stratosphere-troposphere exchange, as well as changes in global atmospheric circulation Golchert et al. (2010). It is also involved in several chemical processes, one of which is ozone depletion Straub et al. (2010); Müller et al. (2008); Deuber et al. (2005).

The most significant periodic variations of H_2O in the upper mesosphere are found at higher latitudes and on seasonal and solar cycle timescales. It is for this reason that the observed variations of H_2O at these altitudes can be a useful diagnostic tool for the performance of models of radiative chemical transport and global change in the mesosphere Laštovička (2009).

Tropospheric phase fluctuation due to the water vapor content limits imaging performances of millimeter wave interferometer arrays Asaki et al. (2000). Water vapor is poorly mixed in the troposphere, and the total column density of water vapor cannot be accurately sensed, therefore, uncertainties in the water vapor content are a serious limitation to the accuracy in radio measurements Thompson et al. (2017). Hence, its study is essential because it contributes to the atmospheric refractive index.

Major achievements in astronomy are closely related to the improvement of observational equipments, however, good equipment must be installed at a site with excellent atmospheric conditions to be fully efficient, astronomers not only carefully design large telescopes, but also spend a lot of time choosing good sites. The atmospheric water content over the site is the main index to measure the quality of a millimeter wavelength observation site. The fluctuation of atmospheric noise radiation caused by the fluctuation of atmospheric water content will limit the sensitivity of the telescope. For a single antenna observation, the variation of atmospheric water content in spatial distribution will also cause variation in the antenna pointing and decrease the antenna gain Li et al. (2020).

In radio observation using full aperture telescopes is affected by anomalous refraction (AR), i.e., an apparent displacement of a radio source from its true position, caused by the phase difference introduced between the opposite extremities of the receiving aperture because the propagation paths traverse air masses of varying humidity. AR pointing effects caused by turbulence in the "wet" atmosphere are similar to the "quivering" of stars observed with visual-wavelength telescopes Olmi (2001). As a consequence, any change in its abundance can have different impacts.

Therefore, measurements from the ground are important for long-term monitoring of water vapor that allows a global approach and understanding of the convective instabilities of moisture in the atmosphere Sherwood et al. (2010), mainly in the troposphere, supported by observations in consecutive satellite missions; thus generating, long-term global data sets, which are crucial for climate research Straub et al. (2010) and support in other scientific areas, such as observational astronomy.

1.3   Water vapor radiometry: Microwave region and the water vapor line

The microwave region, along with its main atmospheric emission sources, is shown in the context of the electromagnetic spectrum in figure (1.6), including the range of about 3 GHz to 300 GHz Janssen (1994).

Within these frequencies are the resonant absorption bands of water vapor molecules at 22.235 GHz (1.35 cm) and 183.310 GHz (1.63 mm) Wilson et al. (2009), resonances at pure rotational transitions Messer et al. (1983). Therefore, for the remote detection of water vapor, it is based on the possibility of obtaining the power or measuring the brightness temperature of the sky at the frequency of 22.235 GHz and estimating thus, the amount of PWV (Precipitable Water Vapor) that produces the profile of the water vapor line. This PWV is essential in carrying out astronomical observations in radio waves (millimeter and submillimeter wavelengths) Cortés Guerrero et al. (2015). PWV is defined as the water on the measurement path of the unit section, compressed into a layer of water with a certain thickness per unit area Li et al. (2020).

The PWV is used as a diagnostic of atmospheric humidity over a specific location. In the case of this thesis work, the study location will be Cerro Ventarrones in the Antofagasta
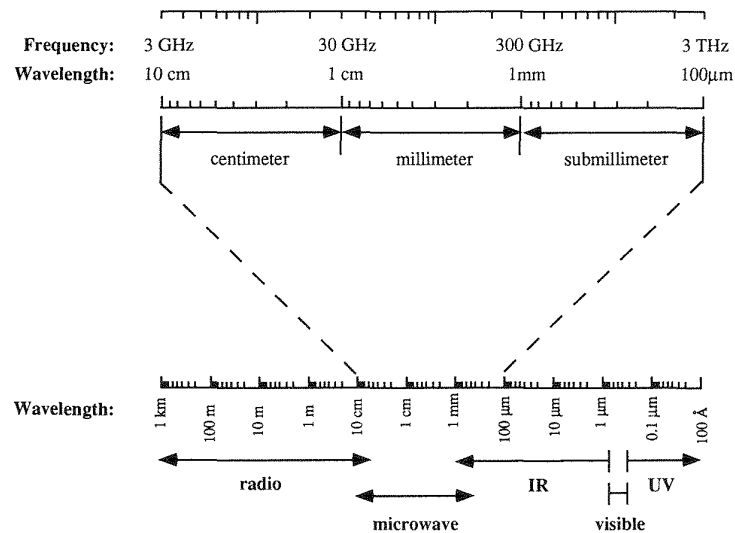
FIGURE 1.7. The microwave region. Strict spectral regimes are shown in centimeter, millimeter, and submillimeter regions. Source: Janssen (1994).

Region, which is close to the astronomical observatories, specifically the Paranal Observatory, where there are atmospheric characterization instruments such as radiometers and will allow an evaluation of the atmosphere of support that may be useful in astronomical observations. The site in question has the coordinates 24°21'17.96" S 70°13'32.614" and is located 2603 masl.

In figure (1.8), the spectral emission of the water vapor line can be observed as the number of PWV increases. This graph results from a computational simulation using the program AM (Atmospheric Model) with characteristic data of the site of interest. AM is a program for radiative transfer computations at microwave through submillimeter wavelengths, for radiation paths that can be modeled as a sequence of atmospheric layers or user-defined path segments. Spectra that can be computed with AM include absorption, thermal emission, and excess delay. The program can modify these spectra to model the response of spectrometers and receiving systems (for more detail about AM, see A).

Figure (1.8) shows the emission spectrum that represents between 0 and 300 GHz, detailing different profiles of atmospheric gases, as can be seen two lines for O_2 at 60 GHz and 119 GHz and shown with specific emphasis on 22 GHz and 183 GHz for water vapor. This model reproduces the atmospheric emission lines in Cerro Ventarrones at different values in mm of the PWV. The amounts of 1 mm are represented by the red line, 2 mm by the green line, and 3 mm by the blue line. These limits are established according to the PWV at the amounts with the highest record in Cerro Paranal in the last 12 years of data collected and evaluated (private communication of work not yet published by CePIA), whose average value of PWV is established at 2.8 mm.

Figure (1.9) shows the emission spectrum simulated with AM where the profile of the water vapor line at 22 GHz in Cerro Ventarrones is shown at different values in mm of the PWV. The increase in brightness temperature in the line profile is observed as the number of PWV increases (see legend located at the top right).
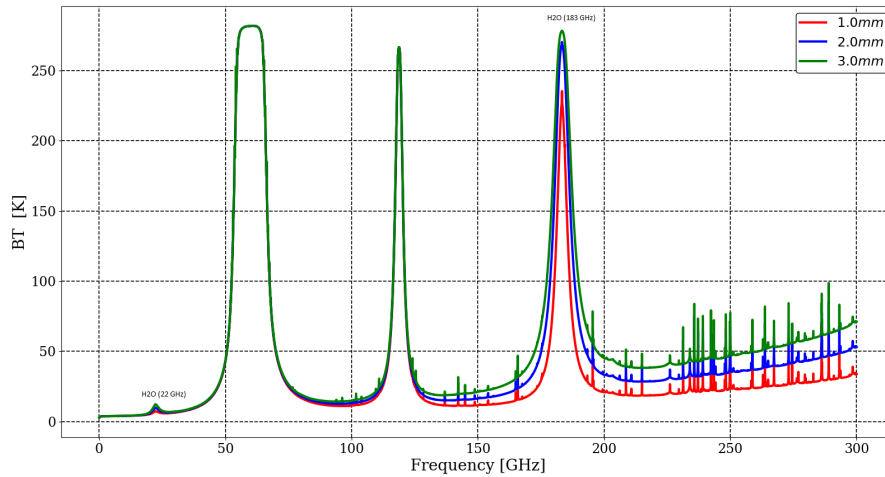
Figure 1.8. Emission spectra modeled with the AM program for the location of Cerro Ventarrones in the Antofa-gasta Region at 2603 masl, brightness temperature (BT) vs. frequency Emissions at different mm of water vapor in the atmosphere are denoted. Source: CePIA.

As the PWV increases, the different profiles of the line increase their value in brightness temperature. Similarly, it is possible to observe a characteristic peak of the water vapor line at 22.235 GHz, figure (1.10), whose detailed study can provide information on the distribution of this gas at the level of the middle atmosphere. In the same way, a spectral shift between the brightness temperature maximums for low and high atmospheres can be seen.

By laws of quantum mechanics, molecules may only attain distinct levels of rotational energy. In a transition between two such levels, E_1 and E_2, a photon that makes up for the energy difference ΔE may be absorbed or emitted,

$$\Delta E = |E_1 - E_2| = h\nu_{1,2} \tag{1.5}$$

where h is Planck's constant Golchert (2009).

A microwave radiometer detects the corresponding radiation at frequency $\nu_{1,2}$. For observations for a radiometer tuned to 22 GHz is 22.235 GHz, is corresponding to the $6_{1,6} - 5_{2,3}$ transition in H_2O (where the quantum number of the angular momentum of rotation and the pseudoquantum numbers for the asymmetric top rotor are considered) Barber et al. (2006)

The extended shape of the steam line at 22 GHz is mainly due to two main phenomena. Doppler motion, which is the thermal motion of observed gases and results in frequency shifts that are imposed on the emission/absorption line. In thermodynamic equilibrium, the relative velocities of individual molecules with respect to the observer obey the Maxwell distribution Golchert (2009). On the other hand, pressure broadening which results from molecular collisions, and shorten the lifetime of excited states, and involve a detailed consideration of the internal degrees of freedom of the colliding molecules Hartmann et al. (2021).
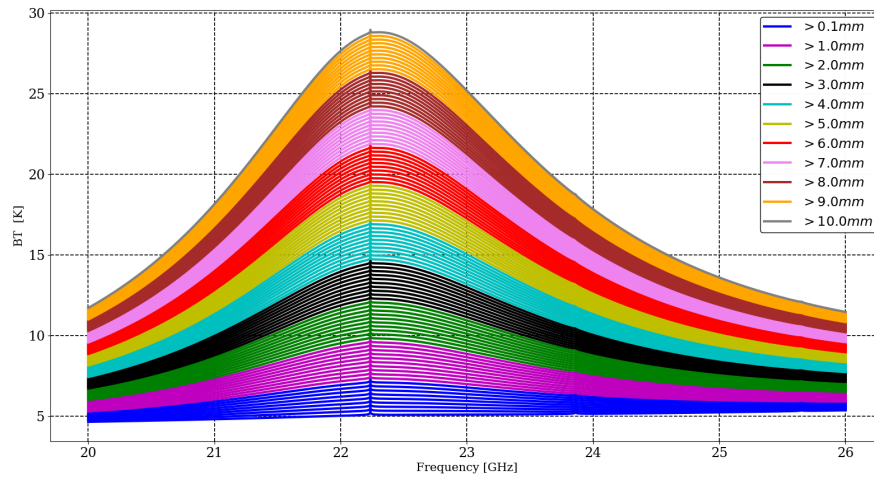
FIGURE 1.9. The model shows the profile of the water vapor line centered at 22.235 GHz made through the AM program for Cerro Ventarrones at 2603 masl (Region II). The different colors that make up the graph curves indicate the amount of PWV between 0.1 mm and 10 mm. Source: CePIA.
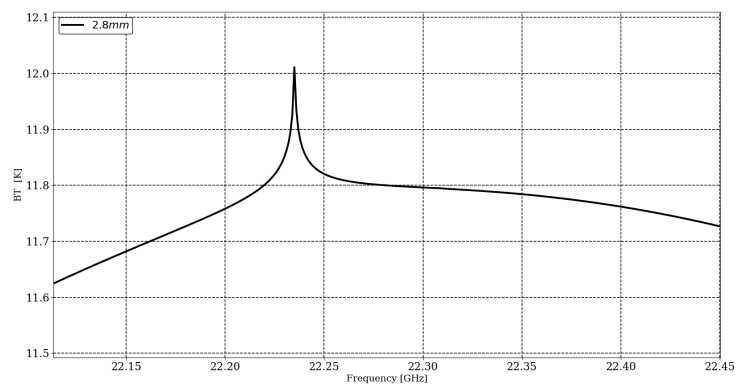
FIGURE 1.10. PWV emission line peak at 2.8mm at 22.235 GHz, line profile wings shown. Source: CePIA.
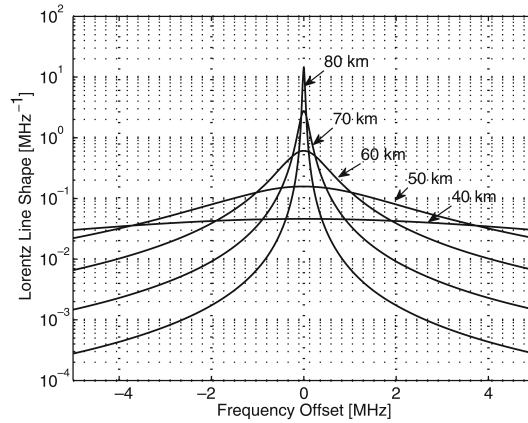
FIGURE 1.11. Pressure broadened line shape for different altitudes. Source: Kämpfer (2012).
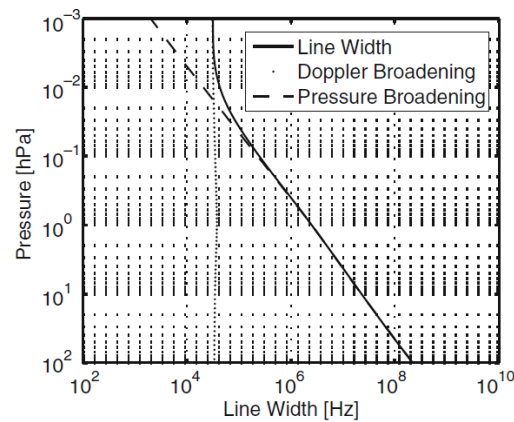
FIGURE 1.12. Line width as a function of pressure altitude in case of pressure and Doppler spread for a line frequency of 22 GHz. Source: Kämpfer (2012).

As shown in figure (1.11), the width of the line in the upper mesosphere is determined primarily by Doppler broadening, while below this the lineshape is dominated by the pressure broadening term Kämpfer (2012).

The combination of Doppler and collisional spreading can be expressed by a Voigt function, in which the purely collisional spreading line shape is integrated over all possible Doppler shifts. Figure (1.12) illustrates the enlarged pressure line shape for a range of altitudes Kämpfer (2012).

Here the pressure broadening is linear in pressure, so it decreases exponentially with altitude. However, concerning the microwave range, it is the dominant effect on the shape of the line until the stratopause. In other words, the signal at some distance from the center of the spectral line is connected to an individual altitude level, and this information can be extracted from the spectra. The contribution to the line shape of the Doppler broadening depends linearly on the frequency of the observed transition, which determines how high the spectral altitude information reaches in the mesosphere. The highest range can be reached by the lowest frequencies Golchert (2009).

The 22 GHz emission line exhibits a pronounced frequency shift that originates from

collision-induced phase shifts in the radiation Golchert (2009). Near the center of a spectral line, the collisional width is governed by the mean time τ_c between collisions affecting the phase of the radiating molecule and fits the Van Vleck-Weisskopf (VVW) line shape description Hill (1986), which is developed under the modified assumption that, post-collision, the probability distribution of the phase of the oscillating dipole is proportional to a Boltzmann factor in the interaction energy between the dipole and the instantaneous field. Since the notion of an instantaneous value of the field is only meaningful when the frequency is low compared with $1/\tau_c$, the VVW line shape is only applicable at millimeter-wave frequencies and lower, and more accurately models the 22 GHz H_2O line than the other forms of simple collision lines Paine (2012); Van Vleck and Weisskopf (1945).

Continuing with the classical harmonic oscillator picture Gross (1955), the line shape is derived under the assumption that collisions cannot instantaneously alter the position of the oscillator; only the momentum is allowed to change discontinuously. The resulting line shape is identical to that of the classical damped harmonic oscillator. The form of the Gross line shape given in the equation (1.6) and is normalized to unity Paine (2012).

$$F_{VVW-coupled} = \frac{1}{\pi} \left(\frac{\nu}{\nu_0} \right)^2 \left[\frac{\gamma_c}{\left(\nu - \nu_0' \right)^2} + \frac{\gamma_c}{\left(\nu - \nu_0' \right)^2 + \gamma_c^2} \right] \tag{1.6}$$

where $\nu_0' = \nu_0 + \Delta\nu_0$, and $\Delta\nu_0$ denotes frequency shift,

$$\Delta\nu_0 = de \left[\frac{T_0}{T} \right]^{\frac{1}{4} + \frac{3}{2}x_s} \tag{1.7}$$

where d is another empirical constant; and the broadening parameter γ_c in (1.6), involves constants, w, x, w_s, and x_s, that must be determined empirically, and is determined by,

$$\gamma_c = w \left[p - e \left(\frac{T_0}{T} \right)^x + wse \left[\frac{T_0}{T} \right]^{x_s} \right] \tag{1.8}$$

The first term governs pressure broadening due to oxygen and nitrogen, while the second one handles self broadening of the observed species, in this case water vapour, at partial pressure, e. T_0 is reference temperature, of arbitrary choice, and p is pressure.

Trends in atmospheric trace species Seele and Hartogh (2000); Nedoluha et al. (2003); Hartogh et al. (2010, 2011) or intra-seasonal oscillations of species traces can be derived using terrestrial microwave radiometry Studer et al. (2012); Scheiben et al. (2013). It is then possible to measure the spectral intensity of the pressure-broadened water vapor emission line at 22.235 GHz Deuber et al. (2004); Straub et al. (2010).

The shape of this line can be related to the vertical distribution of water vapor in the atmosphere Straub et al. (2010), since the calculation of water vapor mixing ratio profiles is based on the variation of the shape of the line with altitude Nedoluha et al. (1995). Therefore, the recovery of water vapor profiles as a function of altitude (or pressure) depends on the sensitivity of the observed spectrum to pressure broadening Nedoluha et al. (1997). In addition, the 22 GHz line is sufficiently optically thin that the core of the line, resulting from middle atmospheric water vapor, can be observed even from moderate tropospheric opacity sites. Nedoluha et al. (2011).

1.3.1   Upper and lower altitude limits in detection of water vapor

The upper limit measurement altitude of the technique is given by the frequency resolution of the spectrometer Straub et al. (2010) and is governed by the altitude at which the spectral line is predominantly Doppler, rather than the expanded pressure, which occurs at approximately 80 km for this water vapor transition, above which there is no longer a strong line shape dependence on altitude. However, the lower limit altitude for retrievals is governed by instrumental considerations and not by the physics of the measurement Nedoluha et al. (2011), it is given by the bandwidth of the spectrometer and the distortion of the spectrum by instrumental artifacts, known as the baseline Straub et al. (2010). Roughly speaking, this is given by the altitude at which the half line width spread pressure is equal to the spectral measurement bandwidth Nedoluha et al. (2011). Measurements at the tropospheric level can have difficulties in the instrumental spectral baseline due to the great variability of the water vapor profile of the troposphere.

This problem limits the accuracy of retrieval of terrestrial millimeter waves is the instrumental spectral reference line. Among the many possible causes of instrumental baseline structure are reflections in the RF and/or IF which cause a standing wave pattern in the spectrum. Furthermore, standing waves in the measurement noise budget can be important Deuber and Kämpfer (2004). Retrieval errors resulting from instrumental baseline artifacts become increasingly important with decreasing recovery altitude because an increasingly larger spectral bandwidth is required to extend the lower bound measurement altitude to the middle and lower stratosphere Nedoluha et al. (2011).

Also, tropospheric water vapor can affect the recovery of water vapor from the upper stratosphere and mesosphere. Consequently, for retrievals in the middle stratosphere and lower stratosphere, tropospheric water vapor must be treated much more carefully Kämpfer et al. (2003); Nedoluha et al. (2017); Hallgren et al. (2012).

1.4   General physical principles

1.4.1   Radiative transfer

The definition of specific intensity I_ν mainly refers to photons that travel freely through the medium per unit area per unit frequency, in a given direction, per solid angle. If one measures length along a line of sight s. In the absence of absorption and scattering, can be expressed as:

$$\frac{dI_\nu}{ds} = 0 \tag{1.9}$$

However, in reality, photons can interact with matter (gas, or in our case, the Earth's atmosphere) and could be absorbed, emitted, or scattered. This requires modifying the previous formulation to consider the different processes that affect photons before the observer receives them. The radiative transfer equation that takes into account all these processes leads to a differential form, neglecting the scattering,

$$\frac{dI_\nu}{ds} = -\alpha_\nu I_\nu + j_\nu \tag{1.10}$$

where the Einstein coefficients are shown, which are j_ν as the emission coefficient or emissivity in terms of $erg \cdot cm^{-3} \cdot sr^{-1} \cdot Hz^{-1}$, and α_ν as the absorption coefficient in terms of cm^{-1}. Both coefficients, emission, and absorption are entered as proportionality constants (empirically).

The radiative transfer equation can be written more simply with the definition of optical depth (it indicates how transparent a medium is),

$$\tau_\nu\left(s\right) = \int_0^s \alpha_\nu\left(s'\right) ds' \tag{1.11}$$

If it is divided by α_ν and the source function $S = \frac{j_\nu}{\alpha_\nu}$ introduced, the radiative transfer equation assumes the following form,

$$\frac{dI_\nu}{d\tau_\nu} = S_\nu - I_\nu \tag{1.12}$$

Rewriting in terms of intensity and source function,

$$I_\nu\left(\tau_\nu\right) = I_\nu\left(0\right)e^{-\tau_\nu} + \int_0^{\tau_\nu} e^{-\left(\tau_\nu - \tau_\nu'\right)} S_\nu\left(\tau_\nu'\right) d\tau_\nu \tag{1.13}$$

The equation (1.13) is read as the initial absorption-attenuated specific intensity plus the absorption-attenuated integrated source function.

In a simple and unrealistic case, where a homogeneous medium is considered, that is, j_ν and α_ν do not vary through the medium, which means that S_ν is constant. According to this last condition,

$$I_\nu\left(\tau_\nu\right) = I_\nu(0)e^{-\tau_\nu} + S_\nu e^{-\tau_\nu} \int_0^{\tau_\nu} e^{\tau_\nu'} d\tau_\nu' \tag{1.14}$$

Solving for the integral:

$$I_\nu\left(\tau_\nu\right) = I_\nu(0)e^{-\tau_\nu} + S_\nu\left(1 - e^{-\tau_\nu}\right) \tag{1.15}$$

The first term expresses the attenuation of the background signal, the second term expresses the added signal due to the emission from the source, and the third term describes the source's self-absorption Rybicki and Lightman (1991).

1.4.2   Black body radiation and Planck's radiation law

All objects at temperatures above absolute zero radiate thermal energy in the form of an electromagnetic wave, they can also absorb or reflect this energy.

A black body is an idealized, perfectly opaque material that absorbs all incident radiation at all frequencies Ulaby et al. (1981). It is also a perfect emitter since the energy absorbed by a material will increase its temperature.

Planck's law gives the radiation brightness of a black body, as a function of the temperature T and the frequency ν:
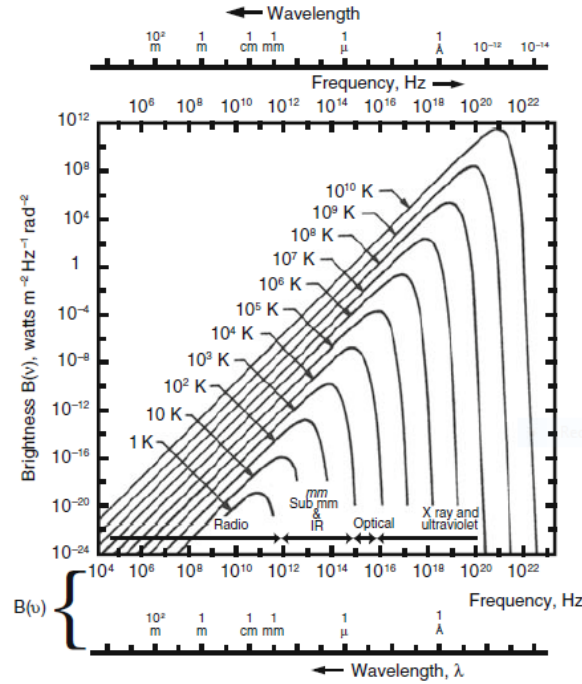
FIGURE 1.13. Planck spectrum for black bodies of different temperatures. Note that curves of brightness as a function of frequency (or wavelength) are of the same shape. Source: Wilson et al. (2009).

$$B_\nu = \frac{2h\nu^3}{c^2} \frac{1}{e^{\frac{h\nu}{kT}} - 1} \tag{1.16}$$

where $h = 6,626070x10^{-34}\ J \cdot s$ is Planck's constant, $k = 1,380649x10^{23}$ J/K is Boltzmann's constant, $c = 299,792,458$ m/s is the speed of light and ν is the frequency in cycles per second or hertz $Hz = s^{-1}$. The brightness-frequency wavelength curves of figure (1.13), are curves of the brightness spectrum as predicted by the Planck radiation law. Integrating the Planck radiation law over all frequencies yields the total brightness B_ν for a black body radiator; therefore, B_ν is the flow of energy through a unit area per unit frequency from a source seen through free space at a solid angle element $d\Omega$ Kraus et al. (1966).

1.4.3 Brightness temperature in microwaves

In the radio wavelength region, the product $h\nu$ may be very small compared to kT ($h\nu << kT$), so that the denominator of the second factor on the right side of Planck's black body radiation law can be expressed as follows Kraus et al. (1966):

$$e^{\frac{h\nu}{kT}} - 1 = 1 + \frac{h\nu}{kT} - 1 = \frac{h\nu}{kT} \tag{1.17}$$

This is known as the Rayleigh-Jeans limit; therefore, the Planck function, equation (1.16), can be written as:

$$B_\nu(T) = \frac{2\nu^2}{c^2} kT \tag{1.18}$$

One of the important features of the Rayleigh-Jeans law is the implication that the brightness and the thermodynamic temperature of the black body that emits this radiation are

strictly proportional Wilson et al. (2009).

Therefore, in equation (1.18) we can replace T by T_b that produces the same power. In such a way that the Rayleigh-Jeans expression is a linear relationship of the Planck function with the physical temperature,

$$T_b = \frac{c^2}{2k} \frac{1}{\nu^2} I_\nu \qquad (1.19)$$

The brightness temperature T_b is then the temperature for which the Planck function reproduces the observed intensity at a particular frequency. In such a way that there is a relationship with the physical properties of the source expressed in K. Therefore, for any value of $I(\nu)$ we define $T_b(\nu)$ by the relationship:

$$I_\nu = B_\nu(T_b) \qquad (1.20)$$

In such a way that the radiative transfer equation can be written in terms of temperature,

$$\frac{dT_b}{d\tau_\nu} = -T_b + T \qquad (1.21)$$

whose formal solution is:

$$T_b = T_b(0) e^{-\tau_\nu} + T\left(1 - e^{-\tau_\nu}\right) \qquad (1.22)$$

If the optical depth is large, the brightness temperature of the radiation approaches the temperature of the material Rybicki and Lightman (1991).

1.4.4   Review of techniques for observing atmospheric parameters

The analysis of the atmosphere using meteorological soundings is a compilation in real-time of all the meteorological variables of the atmosphere with the use of a sensor, providing valuable information over time.

These observations began in the 1920s with ozone measurements. With the advent of meteorological satellites, it was proposed that the vertical distribution of temperature in the atmosphere could be determined by measuring from satellites as a function of the wavelength Kaplan (1959). Thus, the remote sounding of the atmosphere has been carried out by a wide variety of instruments and, humidity is routinely measured at thousands of land-based surface observing stations Sherwood et al. (2010).

Almost all techniques involve the measurement of electromagnetic radiation, although sound propagation has also been used Rodgers (2000), and the great majority of these exploration techniques or methods are passive.

The signal from astronomical objects is attenuated by water vapor in the atmosphere, thus its measurement and the measurement of other atmospheric parameters have been important for a long time. Radiosondes have provided the longest record in the middle atmosphere humidity data, these instruments are able to capture vertical structure Rodgers (2000); Bruegge et al. (1992); Elgered et al. (1982).

Satellite-supplied water vapor data has also been widely used. HIRS (High-resolution Infrared Radiation Sounder) downward scanning instrument used several infrared wavelengths to estimate average relative humidity across broad vertical swaths of the troposphere and has proven invaluable for tracking global changes in upper tropospheric humidity Buehler et al. (2008).

Satellites have been launched to make occultations through the atmosphere and obtain vertical profiles Hajj et al. (2004). The occultations, which are measurements through the limb from a spacecraft as the Sun sets or rises, have a great advantage in vertical profiles Rodgers (2000). Filter radiometers and grating spectrometers have been used in this kind of measurement, one of the emblematic instruments of this type of measurement is the HALOE (Halogen Occultation Experiment) Russell III et al. (1993).

Techniques employing backscattered sunlight can also be used to sense total column water vapor Sherwood et al. (2010). Solar radiation which has been Rayleigh scattered, or scattered by aerosols, and partially absorbed by the target gas can be measured in various geometries, specifically in the nadir or limb from satellites, or in the zenith from the surface Rodgers (2000), that are used for the retrieval of different atmospheric gases. The most well known instrument which work on this principle in the near nadir view are the SBUV (Solar Backscatter Ultraviolet) and TOMS (Total Ozone Mapping Spectrometer) Heath et al. (1978). Has also been used, GOME (Global Ozone Monitoring Experiment) starting in 1996 and SCIAMACHY (Scanning Imaging Absorption Spectrometer for Atmospheric Chartography) starting in 2002 Mieruch et al. (2008).

Similarly, active lidar and radar sensors are able to remotely sense water vapor profiles or low-level 2-D fields via Raman backscattering and DIAL (Differential Absorption Lidar) or travel time delay, respectively Eichinger et al. (1999); Whiteman et al. (2006); Wulfmeyer et al. (2006).

More recently, Global Positioning System (GPS) technology has been useful for observing humidity by estimating the traveltime delay of routine GPS signals, which is determined by water vapor amount and temperature integrated along the signal path Wang and Zhang (2008). Through the Radio Occultation: The GPS-MET (Global Positioning System / Meteorology) instrument is basically a GPS receiver in low Earth orbit that measures the phase delay of the signal from GPS transmitters, providing a measure of the refraction of the radio signal, which depends on the refractivity of the atmosphere and the density of water vapor itself Rodgers (2000). The GPS technique has the important advantages of being an absolute measurement that does not need an independent calibration and of not being affected at all by clouds or other absorbers Sherwood et al. (2010).

Microwave radiation is less affected by clouds and thus offers a useful alternative method of moisture sounding from space Sherwood et al. (2010). The TOPEX Microwave Imager has been operating since 1992, these imagers are used to estimate the column integrated (total) water vapor. And microwave sensors that are exclusively dedicated to humidity measurements have been used since 1990, such as the SSMT/2 or the meters AMSU (Advanced Microwave Sounding Unit) nadir sounders. They are able to detect humidity averaged over

several broad layers, especially in the upper troposphere, with significant interference only from thick clouds Engelen and Stephens (1999); Susskind et al. (2003).

Other passive microwave remote sensing instruments that have allowed the study of water vapor in the atmosphere in space are the MLS (Microwave Limb Sounder) in EOS/Aura Waters et al. (2006), MIPAS (Michelson Interferometer for Passive Atmospheric Sounding) in ENVISAT Milz et al. (2005), SMR (Submillimeter wave Radiometer) in ODIN Murtagh et al. (2002) and FTS (Fourier Transform Spectrometer) Bernath et al. (2005). These satellites provide the vertical and horizontal distribution of water vapor and other trace gases.

However, the lifetime of a satellite is typically limited to less than a decade and therefore the creation of meaningful long-term observational time series from these data requires careful checking of the consistency between different instruments Straub et al. (2011). For this reason that many research groups in the world use microwave radiometers like passive microwave remote sensing instruments on the ground-based to obtain information about atmospheric water vapor.

Why use passive radiometry? Ground-based microwave radiometry is a well-established and approved remote-sensing technique commonly used to derive trends in atmospheric trace species Seele and Hartogh (2000); Nedoluha et al. (2003); Hartogh et al. (2010, 2011). The microwave radiometry offer the opportunity of continuous observations throughout a large altitude range from sea level to mesosphere Bleisch et al. (2011).

Ground-based microwave spectroscopy, using the water vapor rotational transition absorption line at 22.235 GHz, is now a mature and well proven and validated technique for measuring the water vapor profile Nedoluha et al. (2011). Besides, a further advantage of the lower frequency is the availability of low-noise amplifiers with sufficient gain allowing to amplify the atmospheric signal before down-conversion to intermediate frequencies for spectral analysis. This offers a much lower system noise than can normally be achieved at the higher frequency Deuber et al. (2004). Being the most reliable and accessible method for the analysis of atmospheric parameters, following this perspective for the purposes of this thesis, it is the case study in the concept and design of a 22 GHz radiometer.

Chapter 2

Definition of the project

To contribute state of the art in water vapor radiometry, we propose the construction of a radiometer, which function is to measure the radiated intensity from the water vapor line in small ranges in frequency and solid angle, with a real-time system, including improvements in sensitivity with respect to existing instruments, considered for scientific applications.

Therefore, within this project, we detail the development of a water vapor radiometer tuned at 22.235 GHz. The design consists of a heterodyne, SSB (single sideband) radiometer, and that is based on the pseudo-correlation principle pseudo-correlation. It will have a local reference load TL that will allow for the measurement of the atmospheric brightness temperature Tb. We aim to measure the water vapor line emission from different atmospheric layers, and include a vertical analysis covering from sea level up to 80 km, which is feasible for a 22 GHz instrument with frequency resolution higher than a MHz. The use of the instrument is targeted for sites at altitudes below 4000 masl, since the 22 GHz line is not bright enough for thiner atmospheres.

2.1   Motivations and limitations

The work presented in this thesis focuses on the conceptualization and design of an instrument that still under development.

The motivations and limitations that arose during this project are listed as follows:

- Water vapor has a highly variable concentration concentration in space and time in the atmosphere, so its measurement in real-time is an emerging topic of intense interest in supporting climate research, and of course in professional astronomical applications in astronomical observations.

- The main motivation for designing a 22 GHz radiometer in CePIA is to build a new movable instrument that can be easily transported and used during measuring campaigns at remote locations.

- To contribute to state of the art in radiometry by offering an instrument with current technology, highly sensitive, and with a low noise temperature.

- Produce a precise terrestrial instrument that can operate unattended over long periods, which is needed for the validation of measurements taken with space-borne instruments.

- Among the limitations is that the concept and design of the radiometer was carried out from the author's residence due to the pandemic; this did not allow the advancement to the stage of development and construction of the radiometer.

2.2   General objective

Design a prototype of a pseudo-correlation water vapor radiometer tuned to a frequency of 22 GHz for atmospheric characterization.

2.3   Specific objectives

1. Definition of the instrumental requirements for the characterization of the 22 GHz water line, and their corresponding validations.
2. Analysis of the sensitivity of the 22 GHz radiometer.
3. Design of the architecture of the 22 GHz radiometer of CePIA.
4. Accomplish an analytical and mathematical description of the architecture of the 22 GHz radiometer.
5. Carry out simulations to characterize main parameters such as the system gain and the noise temperature of the chain of components defined in the architecture.
6. Generate an RF input based on the measurements made at the site of interest and simulate the propagation of this input through the instrument architecture with commercial components.
7. Approach the requirements that arise at the analog and digital systems interface.
8. Search and selection of the commercial components for the development of the instrument and its verification in simulation.
9. Perform vertical recoveries using the Optimal Estimation Model (OEM) and then AM software (see A), with water vapor data collected for a decade from the NASA MERRA2 satellite.
10. Include the concept of vertical characterization of water vapor in the design of the instrument through other analyses that do not involve the OEM or the AM but rather cover greater detail in sensitivity windows such as kernels and the subsequent use of another software that can satisfy this vertical characterization with better resolution, such as ARTS; see for more detail E).

2.4   Methodology

Here we establish the methodology to be followed in the design project of the 22 GHz radiometer. It follows:

– Prototype development will be approached using NASA's System Engineering methodology, which generates awareness and consistency to advance the practice of systems engineering requirements and processes. This method requires a systematic and disciplined set of processes applied recursively and iteratively for the design, development, operation, maintenance, and shutdown of systems throughout the life cycle of programs and projects, including all system elements (i.e., hardware, software, human systems integration) Hirshorn et al. (2017).

– In parallel, meetings with project members are required to assure the progress.

– A list of references and bibliographic analyzes are generated that are essential for understanding and subsequent performance in the concept and design stages of the instrument.

– Establish the block diagram that identifies the architecture of the radiometer and expresses the mathematical equations that allow understanding the design.

– Make the corresponding simulations that can indicate the sensitivity, noise temperature, and signal analysis throughout the circuit. This is done through the AWR software, a system-level design component of the AWR Design Environment® suite that has automation tools for high-frequency electronic design and allows to know a receiver's theoretical performance (for more detail see D).

– Establish the requirements for choosing the components that will be part of the instrument. In the same way, determine the necessary characteristics and compare with the component datasheets offered in the market to finally select the electronic elements to be acquired.

– Considering the analog-digital integration, an output signal is generated by simulations with AWR, from the evaluated characteristics that indicate the power and frequency of the input to the digital system.

– Provide the concept of vertical characterization as a standard routine to take into account for data acquisition.

2.5   Outline of thesis

This section reports on the first steps in the concept and design of the CePIA 22 GHz pseudo-correlation radiometer project. The structure used here to present the work done is as follows:

Chapter 3: **Microwave radiometry**. This chapter covers the contextualization, in this case, specifically about the current instrumentation, basic concepts of radiometry and the types of receivers used in microwaves and their use in radioastronomy.

Chapter 4: **22 GHz Radiometer desing**. Corresponds to the design and simulation of the CePIA 22 GHz radiometer receiver. Modeling techniques that are part of the specific objectives are presented.

Chapter 5: **Optimal Estimation Model**. In this chapter is included part of the theory of the forward model and the Optimal Estimation Model, which is within the reach

that is available to achieve the recoveries of water vapor at atmospheric level by layers, what this model implies and the equations to consider for our example, in Cerro Ventarrones.

Chapter 6: **Conclusions, Current work and Future Work**. The thesis conclusions are listed, comparing the initial objectives with the goals achieved. In addition, defines the work that is currently being carried out and that is expected to be carried out in the immediate future.

Chapter 3

Microwave radiometry

This chapter discusses the theory required to understand typical microwave receiver architectures, associated noise, sensitivity, and the use of receivers in astronomy.

3.1 Receivers

The function of a receiver is to detect an electromagnetic signal within a specified frequency bandwidth and provide a measure of one or more of its properties Nanzer (2012). Therefore, it is essential that the receiver reliably reconstruct the properties of the input signal, although some hardware characteristics will inevitably alter this.

An ideal receiver is described as a two-port network, figure (3.1), in which the input signal $S_i(\nu)$ is observed, and its output is a reconstruction modified by a transfer function of the receiver $H(\nu)$ that alters the bandwidth of the signal and adds gain or loss of power to the signal. Also, the receiver hardware may allow changing the signal's frequency, reducing it (downconverting) Nanzer (2012).

The receivers have different combinations of components, which will go according to the need of the parameter to be measured. These components are grouped in two categories, passive that do not need the supplied energy to function; they contribute to white noise and exhibit signal loss, particularly antennas, attenuators, and cables. The active components are those that require external activation to function; they are responsible for the ΔG (gain fluctuations) and a large part of the T_N (noise temperature); they are amplifiers, mixers, oscillators, and others.
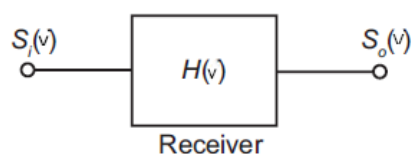
FIGURE 3.1. General receiver modeled as a two-port network. Source: Nanzer (2012).

3.1.1   Heterodyne receiver

A heterodyne receiver is one in which the received signal, called the radio frequency or RF signal, is translated to a different and usually lower frequency (the intermediate frequency, or IF signal) before it is detected Janssen (1994).

The RF signal is coupled to the receiver by an antenna, and it is usually first amplified in an RF amplifier or, in this case, in an LNA (Low Noise Amplifier); then the filtered signal according to the frequency ranges of a BPF (Bandpass Filter).

Then the signal can pass through a mixer, a non-linear device fed by a LO (local oscillator) that generates a constant frequency signal. The function of the mixer is to use the non-linearity of the active device to combine the RF signal and the LO signal and generate an output with a change in the frequency that brings the original signal.

The mixer output consists of the superposition of several components at different frequencies: a DC signal, signals at twice the signal and the local oscillator frequencies, and two components at the difference and the sum of signal and oscillator frequencies. That is $\nu_{IF} = m\nu_{RF} \pm n\nu_{LO}$, where $m = 0, 1, 2...$ and $n = 0, 1, 2...$, and reproduces two frequency bands, one above and one below the LO frequency, these bands are USB (Upper Sideband) and LSB (Low Sideband), figure (3.2b). The amplitudes of the sum and difference frequency signals are reproductions of the amplitude of the input signal. If the receiver is downconverter, and by using an appropriate bandpass filter, all signals except the desired one are suppressed at the output frequency, which is now called IF, has the form $\nu_{IF} = \nu_{RF} - \nu_{\cdot LO}$ Wilson et al. (2009); Maas (1986), figure (3.2a).

The detector, which can be a spectrometer, or in other cases, a square-law device (which squares the voltage signal), generates a rectified signal proportional to the input signal power. The voltage going into the detector can be used by an LPF (Lowpass Filter) to integrate the signal and reduce noise fluctuations.

A more typical heterodyne architecture used in modern sensors is shown in figure (3.3), where the IF signal is digitized using an ADC, and the detection process is performed in software on the digitized signal Nanzer (2012).

3.1.2   Thermal noise

The ability of a receiver to detect small amplitude signals is limited by the presence of noise. The antenna collects noise signals that are not of interest, and the receiver also generates noise.

Noise can be collected from different sources, such as galactic noise, atmospheric noise, or noise from hot electrons due to current fluctuations in strong electric fields Nanzer (2012).
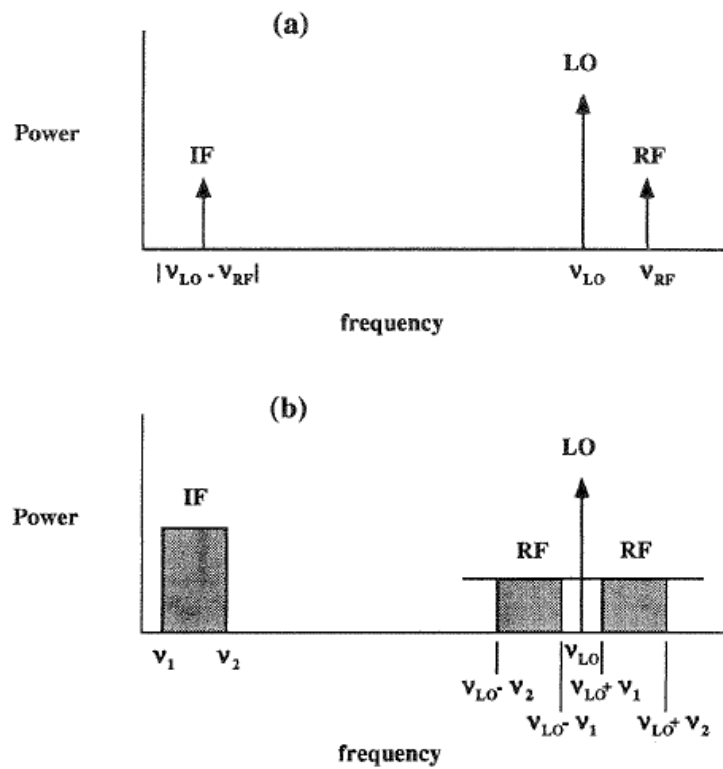
FIGURE 3.2. Frequency translation in heterodyne reception. (a) Monochromatic signal: This signal has the important property that its power is proportional to the power in the RF signal under the condition that the latter is much weaker than the LO signal. It is then filtered to exclude the unwanted products of the mixing, and amplified to produce the IF output signal. (b) Broadband noise: The two RF passbands are called the upper and lower sidebands of the receiver, which are effectively folded about the LO frequency by the mixer and translated into the IF band to create a double sideband receiver. Source: Janssen (1994).
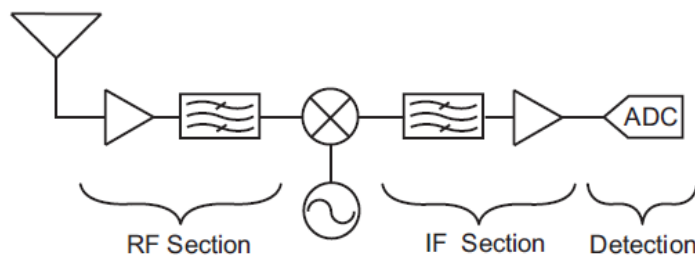
FIGURE 3.3. The architecture of a heterodyne receiver that uses digital detection is shown, note the ADC coupled at the end, after the analog stage of the receiver. Source: Nanzer (2012).

It considers a resistor (of R value) with its terminals available for measurement. The thermal agitation of the physical structure of the resistance establishes an electric current that defines the input signal of the circuit that follows it. The characteristics that define this current established by thermal origin is $< i(t) >= 0$ but the RMS value of $< i^2 > \neq 0$ Reeves (2019). This electronic noise of thermal origin is known as Johnson noise.

In 1929 this fact was proved by H. Nyquist, showing it is a problem similar to the random walk of a particle in Brownian motion, including a friction term Wilson et al. (2009).

The average power produced by the resistance of value R at the input of the circuit is:

$$P = < iv >= \frac{< v_N^2 >}{4R} \tag{3.1}$$

where the first $1/2$ comes from the criterion of maximum power transfer and load balance, and the second $1/2$ corresponds to the average factor, and v_N corresponds to the noise voltage. On the other hand, the power spectral density produced by the resistor R, $v^2/\Delta \nu = 4kTR$ Reeves (2019). Its value is constant throughout the spectrum and is known as white or thermal noise. Replacing the power spectral density in the average power produced by:

$$P = kT\Delta \nu \tag{3.2}$$

The power per unit bandwidth entering a receiver can be characterized by a temperature T, which is the physical temperature of the resistor, and defines the noise power delivered by the element to the circuit that follows it, called *noise temperature*.

Noise is additive because it has the contributions of the source, the atmosphere, the ground, and the receiver. Therefore, in a complete reception system, the contributions are added that include the equivalent temperatures to the antenna (T_A), the power inputs in it, and the receiver noise temperature (T_r), which is equivalent to a noise temperature of the total circuit, this is the system temperature or T_{sys} Salazar (2018); Ulaby et al. (1981).

$$T_{sys} = \sum T_i \tag{3.3}$$

$$T_{sys} = T_A + T_r \tag{3.4}$$

3.1.3   Noise figure and noise temperature

The purpose of a two-port network can be to add gain to a signal in the case the network represents an amplifier or to induce loss in the case of an attenuator. If the two
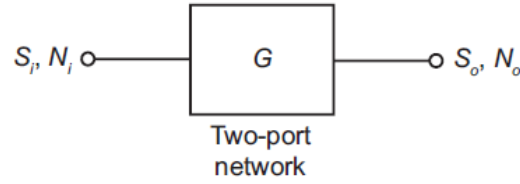
FIGURE 3.4. Generalized two-port network. Source: Nanzer (2012).

ports represent a transmission line, it should ideally not affect the signal. Several different physical processes give rise to internal noise; however, it is convenient to model the output noise in terms of a single equivalent noise temperature that encompasses the noise due to all internal noise sources rather than characterizing each noise source individually Nanzer (2012).

Figure (3.4) shows a general two-port network with input and output signals and noise powers. The quantity used to characterize the degradation of the input signal by the noise in the network is called the noise factor Nanzer (2012). This factor is defined by a relationship between the signal-noise at the input and output of the receiver so that the higher the *noise factor*, the noisier the receiver.

$$F = \frac{S_i/N_i}{S_0/N_0} \tag{3.5}$$

where S_i and S_o are the input and output signal powers, $N_i = kT_0\Delta f$ and N_o are the input and output noise powers, and S/N is the signal-to-noise ratio at the input or output.

The definition of F has been standardized by defining the input noise power as that of a temperature-matched resistor $T_0 = 290$ K, which is approximately room temperature. In most situations, it is typical to see values for the *noise figure*, which is simply the noise factor expressed in decibels Nanzer (2012):

$$F(dB) = 10log_{10}(F) \tag{3.6}$$

The *noise temperature T_n* of the receiver elements is the conversion of the noise factor to an equivalent input temperature, which, when it exists, produces a specific output noise power given by:

$$T_n = T_0(F - 1) \tag{3.7}$$

This noise temperature is calculated from the noise factor and the ambient temperature T_0, which is expressed in Kelvin Salazar (2018).

3.1.4 Noise temperature in series connection

Microwave receivers consist of a series connection of individual components in a cascade network, considering a heterodyne receiver, figure (3.3), where each element
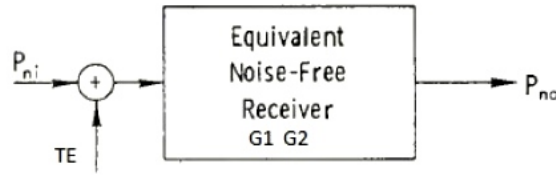
FIGURE 3.5. Equivalent representation of a heterodyne receiver. The noise behavior of the cascade can be represented as a single subsystem with equivalent input noise temperature T_E, whose input power is $P_{in} = kT_i\Delta\nu$, and where $G = G1 \cdot G2$ is the gain of the subsystem where the gains of each component are considered (in this example case, two gains). P_{no} represents the output power of the equivalent system. Source: Ulaby et al. (1981).

contributes to the noise of the overall system.

The noise behavior of the cascade is considered as a whole; that is, the cascade network can be represented as a single subsystem with an equivalent input noise temperature T_E, figure (3.5), and whose input power is $P_{in} = kT_i\Delta\nu$.

The output noise power of the single subsystem in this representation is:

$$P_{no} = Gk(T_i + T_E)\Delta\nu \tag{3.8}$$

where $G = G1 \cdot G2$ is the subsystem's gain where each component's gains are considered (in this example case, two gains).

The equivalent input noise temperature of the cascade network can be found in terms of the equivalent input noise temperatures of the individual subsystems. In particular,

$$T_E = T_{E1} + \frac{T_{E2}}{G_1} \tag{3.9}$$

This can be directly extended to a general number of subsystems N, leaving equation (3.9),

$$T_r = T_1 + \frac{T_2}{G_1} + \frac{T_3}{G_1 G_2} + \frac{T_n}{G_1...G_{n-1}} \tag{3.10}$$

This equation (3.10) is known as the *Friis equation*, and represents the receiver noise temperature T_r. As observed, a configuration should be available such that the amplifier with the lowest noise temperature at the receiver start is used first; for the following stages, the noise temperatures may be higher Nanzer (2012); Pozar (2011); Wilson et al. (2009).

3.1.5 Sensitivity

A receiver must be sensitive, that is, capable of detecting weak signals in the presence of noise. As with any other measurement device, there are limits to this sensitivity, as the receiver input and the receiver itself are affected by noise Wilson et al. (2009).

In practice gain variations are unavoidable, especially with the very high gains that are necessary in receivers Kraus et al. (1966). Gain temperature variations can be primarily traced to the variation in bias resistance in the amplifiers, which results in variations in the source current, short-term variations can be due to power supply instabilities Nanzer (2012). This is because the detector that is part of the receiver cannot distinguish between increases in power in the signal and increases in power due to a higher gain on the part of the amplifiers.

Through an idealized block system of a heterodyne receiver, figure (3.3), a signal passes from the antenna to an amplifier characterized by its power gain factor G. If the gain is high enough, this amplifier will set the noise performance of the entire system, which we denote as $Tsys$.

This signal passes through a filter that determines the $\Delta \nu$ frequency bandwidth. Then the signal is converted into a digital data stream sampled at a τ integration time. Moreover, output fluctuations due to gain variations are independent of the fluctuations resulting from system noise.

Radiometric sensitivity, or minimum detectable temperature ΔT_{min}, is expressed:

$$\Delta T_{min} = K_s T_{sys} \sqrt{\frac{1}{\Delta \nu \cdot \tau} + \left(\frac{\Delta G}{G}\right)^2} \tag{3.11}$$

where $\Delta \nu$ is the receiver bandwidth, τ the integration time, $Tsys$ the system temperature, G average power gain, ΔG value of the detected receiver power-gain variations, and K_s corresponds to a constant related to the architecture of the receiver.

Variations of the receiver noise temperature and the bandwidth of the receiver decrease the sensitivity in the same way as to gain instability Kraus et al. (1966). The equation (3.11) is called as *radiometer equation*.

3.1.6 Gain fluctuations and $1/f$ noise

Establishing instrument stability by mitigating amplitude noise and spurious tones is very important in radiometer design, so much attention is paid to mitigating $1/f$ contribution gain fluctuation Jarosik et al. (2003); Kooi (2008).

As seen above, electronic element-based detection systems suffer from fluctuations in the system's overall gain, which result in the propagation of these fluctuations to the measured counts or the digitized voltage signal. In addition, the gain variations in the preset section arise primarily from the RF amplifier and secondly from the mixer and IF amplifier.

Since V_{out} is linearly related to the product GT_{sys}, an increase in G by ΔG will be misinterpreted by the output as an increase in T_{sys} by $\Delta T_{sys} = T_{sys}(\Delta G/G)$.

This has implications for detection systems since in ideal systems, the output spectrum of an instrument has a flat power density given by white noise, such as that produced by a passive thermal source, such as a resistor.

However, the temperature of the systems increases monotonically as the frequency decreases from the point where the frequency of the white noise spectrum intersects the spectrum of non-white components. This point is called the *knee frequency*, figure (3.6).
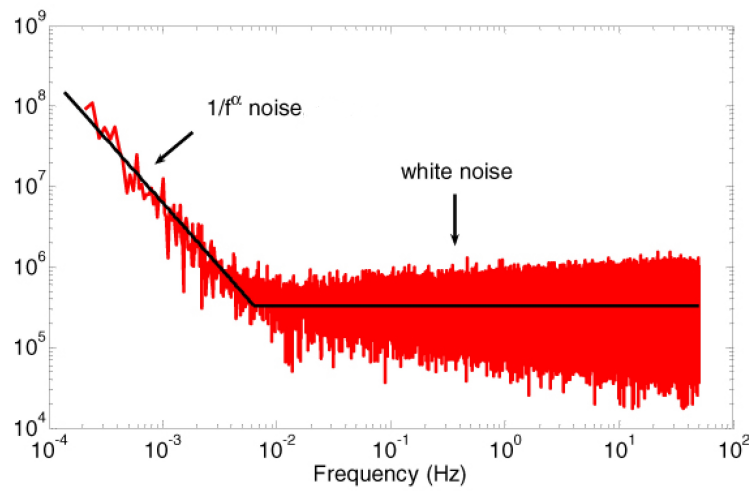
FIGURE 3.6. Widespread representation of PSD (Power Spectral Density). Source: Reeves (2019).

The signal must be modulated and demodulated to reduce the contribution of $1/f$ noise. Statistically, the uncertainty due to the variations of gain of the system can be defined as,

$$\Delta T_G = T_{sys}\left(\frac{\Delta G}{G}\right) \tag{3.12}$$

where G is the average power gain of the system and ΔG is the effective value of the detected power gain variation.

The gain fluctuations present a limit to the maximum sensitivity of the instrument, contribute to raising the noise of the instrument, and are often the limiting factor to achieving high radiometric resolutions as it is integrated for more extended periods of time.

Therefore, a trade-off is always sought between minimizing the radiometric temperature resolution and the scanning speed, where the integration time is increased to reduce the radiometric temperature resolution. However, if the integration time is less

than the residence time, the radiometer is not achieving the best possible sensitivity.

One possibility to reduce the gain fluctuations at the instrument output is to alter the system architecture to reduce the effect of the fluctuations using the Dicke architecture, which uses the modulation technique described in section 3.2.2.

Thereby, the ΔT radiometric resolution, equation (3.11), implies that given a change in the architecture of the receiver, we can achieve that the temperature variations of the system, product of the gain variations, are canceled as long as the temperature is the equal noise level of the reference signal with the antenna temperature Reeves (2019).

3.1.7   Receiver calibration

Calibrating the receiver refers specifically to obtaining the receiver noise temperature accurately and finding a relationship between power and temperature to calibrate the data obtained, i.e., one relates the noise temperature increment at the receiver input to a given measured receiver output increment.

The calculation of the receiver noise temperature is done using a procedure known as the *Y-factor method*. The receiver is calibrated by connecting two reference noise temperature known power sources to the input Ulaby et al. (1981). In this measurement method, the process consists of detecting and relating the power delivered by the receiver when it faces a cold load and a hot load that has known temperatures. Hence, the power for the hot load P_{Hot} and the power for the cold load at P_{Cold} are given by:

$$P_{Hot} = k\Delta\nu(T_{Hot+T_r}) \tag{3.13}$$

$$P_{Cold} = k\Delta\nu(T_{Cold+T_r}) \tag{3.14}$$

where, k is the Boltzmann constant, $\Delta\nu$ is the bandwidth in which the measurement is being made, T_r is the receiver's noise temperature, T_{Hot} is the physical temperature of the hot load, T_{Cold} is the temperature of cold load physics.

Assuming that the physical temperature of each load is considered as an antenna temperature, the receiver noise temperature will be realized by:

$$Y = \frac{P_{Hot}}{P_{Cold}} = \frac{k\Delta\nu(T_{Hot} + T_r)}{k\Delta\nu(T_{Cold} + T_r)} = \frac{T_{Hot} + T_r}{T_{Cold} + T_r} \tag{3.15}$$

$$Y(T_{Cold} + T_r) = T_{Hot} + T_r \tag{3.16}$$

$$YT_r - T_r = T_{Hot} + YT_{Cold} \tag{3.17}$$

$$(Y-1)T_r = T_{Hot} + YT_{Cold} \tag{3.18}$$
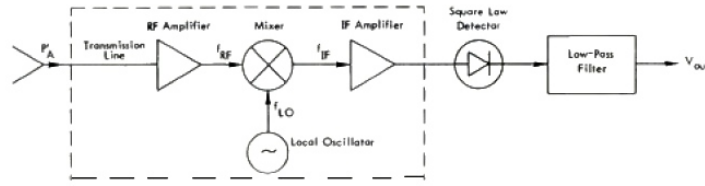
FIGURE 3.7. Block diagram of a total power receiver. Source: Ulaby et al. (1981).

The receiver temperature is given by:

$$T_r = \frac{T_{Hot} - Y T_{Cold}}{Y - 1} \tag{3.19}$$

This temperature is used to obtain the temperature of the system T_{sys} and then to obtain the sensitivity of the receiver Salazar (2018).

The noise temperatures T_{Hot} and T_{Cold} are usually produced by matched resistive loads (absorbers in the millimeter/sub-millimeter wavelength ranges) at the ambient temperature ($T_{Hot} = 293$ K or 20 °C) and at the temperature of liquid nitrogen ($T_{Cold} = 78$ K or -195 °C) or sometimes liquid helium Wilson et al. (2009), or oxygen at 66 K.

3.2 Radiometers

A radiometer is a sensor that measures the electromagnetic power that an object radiates, and in the microwave region, the thermally radiated energy is linearly proportional to its physical temperature. Therefore, a radiometer measures the object's temperature when measuring the radiated power. Radiometers must have very high gain to respond to the extremely low power levels of the signals of interest, and they must also have high sensitivity. Nanzer (2012).

Microwave radiometers are as varied in design as the applications for which they were developed, and considerations at a given frequency include performance factors such as sensitivity, precision, and spatial resolution. Different kinds of architectures can be used depending on the frequency and the object of measurement.

3.2.1 Total power radiometer

Any receiver which measures the total noise power from the antenna and the receiver itself is called a total power receiver, without providing an intrinsic method of differentiating.

A block diagram of an available, total power receiver is shown in figure (3.7), consisting of an antenna, a receiver with frequency response $H(\nu)$ Nanzer (2012), in this case, a quadratic law detector, and an integrator or low-pass filter.

The system noise temperature is taken to be T_{sys}, and ΔT is the signal noise temperature or change in antenna temperature to be measured.

The spectral power at the antenna terminals of the total power radiometer is:

$$P_A = kT_A \tag{3.20}$$

where the antenna temperature T_A is proportional to the temperature of the source. The circuitry introduces a noise power T_r and has gain G and bandwidth $\Delta \nu$. For a passband, the power incident on the detector diode is:

$$P_D = GkT_{sys}\Delta \nu = Gk\left(T_r + T_A\right)\Delta \nu \tag{3.21}$$

Hence, the mean voltage on the output of the detector is:

$$V_d = KGkT_{sys}\Delta \nu \tag{3.22}$$

where K is the power sensitivity of the detector. The output voltage is:

$$V_{out} = G_{sys}kT_A\Delta \nu \tag{3.23}$$

with $G_{sys} = g_{LPF}KG$. The total power voltage response is directly proportional to the source's temperature.

The integration of a random signal of bandwidth $\Delta \nu$ during a time τ leads to a reduction of its variance by the factor $\Delta \nu \cdot \tau$. Assuming that all the system parameters are constant, equation (3.23) is equivalent to,

$$\frac{\Delta T}{T_{sys}} = \frac{1}{\sqrt{\Delta \nu \cdot \tau}} \tag{3.24}$$

Can be rewritten in the form,

$$\Delta T = \frac{T_{sys}}{\sqrt{\Delta \nu \cdot \tau}} \tag{3.25}$$

The above equation defines an ideal total power radiometer's radiometric sensitivity (or resolution) with no gain fluctuations Ulaby et al. (1981).

3.2.2 Dicke radiometer

The total power radiometer is not suitable for many applications because it is difficult to stabilize and calibrate. However, by means of the Dicke radiometer method Dicke (1946) it is possible to stabilize a radiometer.

The method repeatedly switches the radiometer input between the antenna terminals and a reference load at a known temperature, figure (3.8). A reference load can be
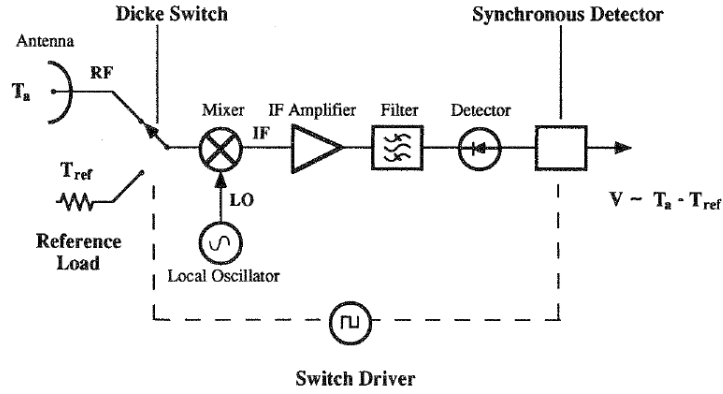
FIGURE 3.8. Schematic of a Dicke radiometer. Note the characteristic switch of this architecture, which exchanges between the two different inputs, of the signal and the reference load. Source: Janssen (1994).

an external load viewed by a second antenna or a load internal to the circuit, with the load maintained at a known temperature in either case Janssen (1994). The switching frequency must be fast enough to constant gain during the switching period.

The receiver is followed by a synchronous detector, which rectifies the switched signal so that the output is proportional to the difference between antenna and load temperatures. Measurements show that gain fluctuations decrease rapidly as their frequency increases Yaroshenko (1964). If the switching time is much shorter than the characteristic period of the gain fluctuations, then the gain fluctuations cause only the measured temperature difference to vary.

Accordingly, the output is:

$$V_{out} = kG\left(T_A - T_R\right)\Delta\nu \tag{3.26}$$

where T_R is the reference temperature. The temperature uncertainty due to gain variations is:

$$\Delta T_G = \left(T_A - T_R\right)\frac{\Delta G}{G} \tag{3.27}$$

If the reference temperature is set such that $T_R = T_A$, the radiometer is balanced, and the measured temperature uncertainty due to gain variations is zero.

In Dicke receivers, the signal is connected to the receiver half of the time only, degrading the sensitivity by a factor of $\sqrt{2}$, In addition, the sensitivity is degraded by another factor of $\sqrt{2}$ due to subtraction of two noise signals Kraus et al. (1966). Hence, the sensitivity of the Dicke receiver is

$$\Delta T = 2\frac{T_{sys}}{\sqrt{\Delta\nu\cdot\tau}} \tag{3.28}$$
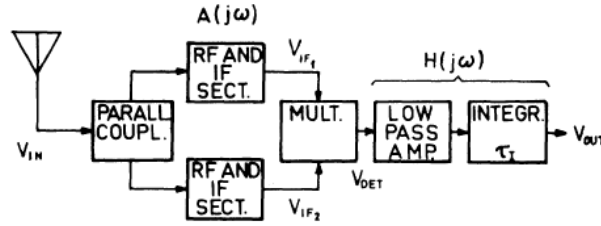
FIGURE 3.9. Correlation receiver. In this design it is shown that two identical receivers are connected, and the output voltage is proportional to the power of the signal. Source: Tiuri (1964).

which is worse that of the total power radiometer by a factor of two (2). Because the net integration time at the source is halved and two equally uncertain quantities are differentiated to form the result Nanzer (2012).

3.2.3 Correlation radiometer

Two identical receivers can be connected as shown in figure (3.9), resulting in a correlation receiver Goldstein (1955). IF output voltages from the two separate receivers, as in an interferometer, are multiplied instead of added and detected.

As in the total power receiver detector, the uncorrelated noise voltage components of both receivers beat each other in the multiplier, resulting in a low frequency fluctuating noise voltage output, containing only a correlation signal or a signal proportional to the noise power coming from the antenna, and is the same for both receivers. The output voltage, which is proportional to the power of the signal, can be given by,

$$V_{out} = GkT_A\Delta\nu \tag{3.29}$$

The sensitivity of the correlation receiver is:

$$\Delta T_{min} = \sqrt{2}\frac{T_{sys}}{\sqrt{\Delta\nu \cdot \tau}}\sqrt{1 + \left(\frac{1/2T_A}{T_{sys}}\right)^2} \tag{3.30}$$

where, in this case, $T_{sys} = \frac{1}{2}T_A + T_r$.

If the signal noise is a small fraction of the antenna noise and receiver noise is small compared to antenna noise, then the sensitivity is the same as that of the total power receiver. Hence, the correlation receiver is useful only when T_A is small Tiuri (1964).

3.2.4 Pseudo-Correlation radiometer

In coherent radiometric systems, one of the major concerns is the intrinsic instability due to gain and noise temperature fluctuations of the amplifiers themselves, typically well represented by a $1/f$ -type noise spectrum. Recently, a scheme called "pseudo-correlation" radiometer has been introduced to improve over the classical Dicke scheme by a factor $\sqrt{2}$, allowing for improving the sensitivity of the instrument regarding amplifier instabilities at very low levels and also in the presence of small
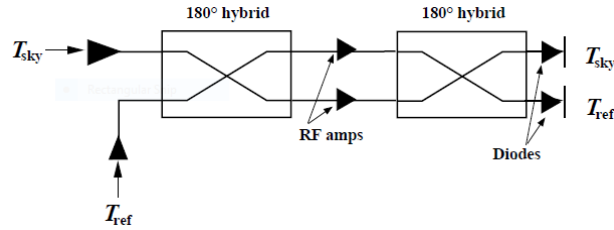
FIGURE 3.10. A pseudo-correlation radiometer in its simplest form. This scheme allows a differential measurement without requiring an active switch before the first RF gain stage Mennella et al. (2003b).

non-idealities in the components of the radiometric chain, and eliminates the necessity for beam steering out of the target of interest. This design has a two-port front-end that allows a continuous comparison between the sky signal Tsky and a stable reference signal T_{ref}, improving the sensitivity. In addition, fast (few kHz) phase switching provides immunity from back-end fluctuations **?**.

In figure (3.10) it is appreciated a schematic of a pseudo-correlation radiometer in its simplest form. In each radiometer of pseudo-correlation, the sky signal and the signal from a stable reference load pass through a 180° hybrid. One of the two signals then runs through a switch that applies a phase shift oscillating between 0 and 180°. The signals are then recombined by a second 180° hybrid, producing an output that is a sequence of signals alternating at twice the phase switch frequency. The RF signals are further amplified in the backend, filtered by a low-pass filter, and then detected. After detection, the sky and reference load signals are integrated, digitized, and differenced Mennella et al. (2003a).

3.3   Digital spectrometer

The design of the spectrometers focuses on obtaining the spectral information (spectral lines) contained in the radiation captured Sapunar Opazo (2015). Spectrometers are designed to measure the PSD (Power Spectral Density), and the main parameters that characterize the spectrometer are overall bandwidth and spectral resolution.

They are mainly used to make vertical and stratified atmospheric characterizations of different gaseous components. There are different spectrometers to analyze the signal of interest, which for this particular case, will be the profile of atmospheric water vapor at 22 GHz, using a digital FFT spectrometer with the Fourier transform (Fourier analysis is a family of mathematical techniques based on the decomposition of signals into sinusoids) to find the PSD; for which an algorithm is used that is capable of extracting the signal from the spectrum in time, that is, the power spectrum of a signal is the Fourier transform of the autocorrelation function of that signal Thompson et al. (2017).

The data before reaching a digital FFT (Fast Fourier Transform) spectrometer first goes through an analog-to-digital converter or ADC that samples the electrical field of the incoming signal by periodically taking amplitude measurements of the analog

signal so that it can then be processed. . the sampled signal corresponds to a discrete signal in time, in the same way it assigns a single output level to the samples and binary codes to the levels obtained, that is, the ADC samples, quantifies and encodes the incoming signal. These samples are then processed directly by a FPGA (Field Programmable Gate Array), a large collection of logic gates that calculates the FFT (Fast Fourier Transform) in real time **?**. They are designed to be reconfigurable, their structure is based on the hierarchy of logical blocks and reprogrammable interconnections both for their internal structure and for their peripheral interface and support subsystems Widmer et al. (2007); Trimberger (2018).

3.4 Use of radiometers in astronomy

Precipitable Water Vapor (PWV) in the atmosphere seriously affects ground-based astronomical observations over a wide waveband, this effect occurs because water vapor attenuates light from astronomical sources Naylor et al. (2002); Marshall et al. (2008,?); Kausch et al. (2015). In addition, the emission of water vapor also increases the background, which reduces the observation sensitivity Silva et al. (2010).

Because water vapor undergoes rapid variations over time, both in different directions and at different locations, and because the line of sight to astronomical targets is constantly changing over time, water vapor along the line of sight significantly influences astronomical observations. Therefore, locally, along the line of sight, it is necessary to monitor water vapor in real time to correct astronomical observations Xu et al. (2020).

Water vapor is mainly distributed in the troposphere and lower stratosphere and has important effects on astronomical observations, which is why astronomers have proposed several methods to measure the content of vertical PWV columns in millimeters Li et al. (2003) . In this context, it is necessary to investigate the role that some key meteorological parameters play in the quality of astronomical observations to understand the impact of climate change on future observations Cantalloube et al. (2020).

It is for this reason that designing instruments that allow analyzing the atmospheric parameters that interrupt astronomical observation is of the utmost importance. In this context, radiometers are commonly used instruments in radio astronomy, and can also be used in atmospheric physics to support observations. Similarly, radiometers have been used to measure the radio emission from numerous objects in our galaxy, as well as from objects in other galaxies Ulaby et al. (1981).

Due to the effective spatial resolution of microwave radiometers, they have been included on satellites for astronomical analysis and on satellites for applications involving observations of atmospheric parameters. These parameters include atmospheric water vapor content, liquid water content, temperature profiles Staelin et al. (1973); Wilheit (1980), and rainfall rates Wilheit et al. (1977). Similarly, they have been used in

satellites, as was the case of the Microwave Anisotropy Probe, launched in 2001, which contained 20 radiometers Jarosik et al. (2003), which were of support in the discovery of the CMB (Cosmic Microwave Background) .

All radio telescopes require a radiometer to operate at their full capacity, in addition to including atmospheric opacity calibrations in their measurements. For more than 30 years, astronomical observatories have been collecting daily meteorological data that can be used together to study the effect of climate change and refine the link between synoptic and optical turbulence scales, particularly in Chile, where interactions between the ocean , the coastal zone and the Andes involve complex mechanisms Cantalloube et al. (2020).

At the conclusion of the chapter

Considering all this and considering all the theories related to the receivers, our instrument, a pseudo-correlation water vapor radiometer tuned to 22 GHz that we are designing and currently characterizing its parts, can contribute to the characterization of the vapor of atmospheric water as support in the astronomical observations in the country, in a particular case, for observatories under 4000 meters above sea level. The CePIA laboratory has the personnel and the infrastructure to carry out this prototype, which is expected to be operating in a few months, in a first phase in the city of Concepción to establish measurement parameters and data acquisition and then carry it out to the place that is expected to be a contribution in Cerro Ventarrones. This place is close to Paranal, which can be validated with other radiometers or instruments whose objective is the same.

Chapter 4

22 GHz Radiometer desing and results

This chapter shows the calculations, analysis, and simulations of the signal passing through the instrument, components, and the complete analog system. In addition, the results of the main parameters of the radiometer design, which are part of the specific objectives presented in this work, are revealed.

4.1   Conceptual stage

Remote sensing is the science or technology for acquiring information, such as identifying, classifying, and determining objects on the earth's surface and the environment from air or space by means of electromagnetic waves Karmakar (2019).

Water vapor is not a well-mixed atmospheric component, making it impossible to model it with a high degree of precision, and even though it is found in small quantities in the atmosphere, it controls its thermodynamic equilibrium, so its measurement in real-time is an emerging topic of great interest for research and the most promising available technique for making vapor measurement is the use of passive microwave radiometry Karmakar (2019).

The use of microwave radiometers offers certain advantages, calculations of the intensities of the spectral lines are simpler and safer because it is not necessary to know the vibratory and electronic wave functions, in addition, millimeter wave radiation, unlike ultraviolet and visible radiation, is not affected by atmospheric aerosols, thus in itself, the high spectral resolution that can be obtained allows the measurement of spectral line shapes from which information on the altitude distribution can be obtained Parrish et al. (1988).

The 22.234 GHz line is primarily suitable for ground-based surveys, which can provide valuable information on total water vapor content, diurnal variation of water content, and even vertical distribution Resch (1983).
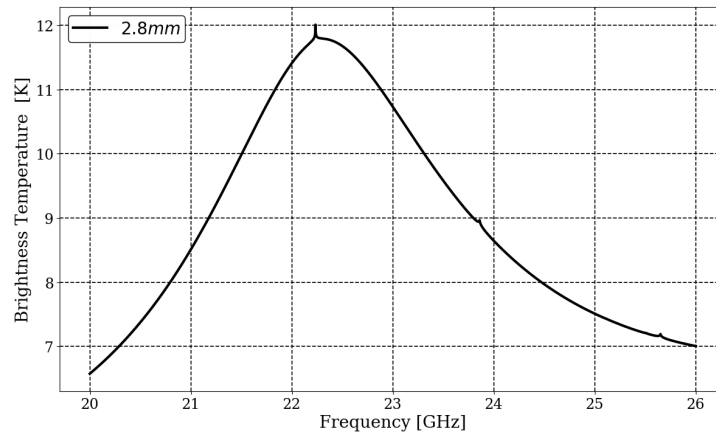
FIGURE 4.1. Representative water vapor emission line profile at 22.235 GHz for 2.8 mm PWV. Note the asymmetry of the profile and the peak. Source: CePIA.
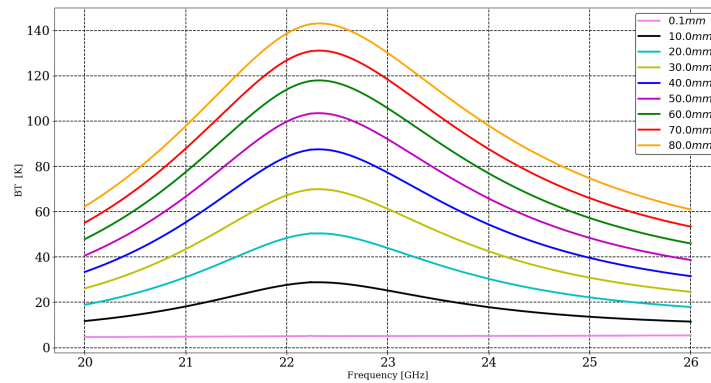
FIGURE 4.2. The model show the profile of the water vapor line centered at 22.235 GHz made through the AM program for Cerro Ventarrones (Region II). The different colors that make up the curves of the graph indicate the amount of PWV between 0.1 mm and 80 mm, more widely spaced. We see in this modeling that the profile of the line shows no apparent saturation. Source: CePIA.

The measure of the intensity of the water vapor line of 22.235 GHz, presents an asymmetric line profile as seen in figures (4.1) and (4.2). These figures correspond to an atmospheric simulation carried out with the AM program. The profile of the water vapor line is observed as the amount of PWV (precipitable water vapor) increases, each colored line represents a different amount of PWV ranging from 0.1 mm to 80 mm (the legend located on the top right shows how much PWV each line represents). The line profile remains independent of the amount of PWV present.

The retrieval of water vapor profiles as a function of altitude (or pressure) from the measured spectrum is based on the sensitivity of the emission at each altitude to increased pressure. The signal-to-noise ratio governs the contribution of the a priori profile to recovery and must be kept constant. This, in turn, requires longer integration times for higher opacities Haefele et al. (2009), and thus establish stability. The measurement time depends on the instrument, the conditions of the troposphere and the

desired range of the profile to retrieval Straub et al. (2011). Hence, the time between two retrievals changes drastically with the season.

4.1.1   Requirements

To contribute to the state of the art in water vapor radiometry, the construction of a radiometer is proposed, with a real-time system, improvements in the sensitivity, and the scope of data retrievals for corrections in scientific applications.

The design of this instrument contemplates a mixture of functions that will allow the expected objectives to be addressed. Among them:

- Autocalibration: Allows to calibrate of the instrument with internal components of the architecture, this function is performed by a digitally controlled noise diode. The instrument can receive the temperature of a known load, which will be activated by means of a CS (commutator switch), and is displayed as a noise that works like a T_L calibrated load, monitored in real time.

- Heterodination: Allows the signal received at the antenna to be converted into a fixed intermediate frequency signal, which can be more conveniently processed than the original radio frequency.

- Low noise amplification: The input signal is weak and electronic noise can dominate the measurement, and LNA (Low Noise Amplifiers) are used, located on the front-end, which allow increasing the signal power with low noise of the signal.

- Pseudo-correlation: This design continually compares the sky signal to a stable reference load. It allows for improving the sensitivity of the instrument. The result of the pseudocorrelation is that each output of the spectrometer is directly proportional to the brightness temperature of the load or the input, and depending on the phase, which changes sign, the demodulation of the output provides a stable measurement in the time. Therefore, the reference charge is critical to the system's operation and is a crucial part of the pseudocorrelation.

- Band rejection: Allows to eliminate one of the sidebands from the center frequency. This refers to detecting only one of the sidebands. This function is made possible by the bandpass filter on the frontend. In practice, it is a system consisting of single-band RF to IF translation, since the RF amplifier generally has a wider bandwidth than that of the IF amplifier and therefore the width of the band going to the digital part is effectively determined by the IF amplifier's bandpass characteristics. It is an SSB (single sideband) system.

- Digital spectrometry: Through this process, it is possible to obtain spectral bands within 22 GHz frequency range. This will allow vertical characterization in the water

vapor column, using the spectral recovery method, and the FFT.

Based on the proposal and the preliminary aspects presented, the instrumental requirements for the concept stage within the development of the 22 GHz water vapor radiometer prototype are defined, summarized in table (4.1).

TABLE 4.1. Important thirteen (13) requirements for the development of the prototype of CePIA's 22 GHz radiometer.

N°	Requirement	Value
1	Center frequency	22.235 GHz
2	Frequency range	(20 – 26 GHz)
3	IF bandwidth	0 - 6 GHz
4	Portability	Yes
5	Backend type	Digital spectrometer
6	Measurement altitude range	0 – 80 km
7	Bandwidth/Channel	62.5 kHz
8	Number of channels	65536
9	Measurement objetive	Water vapor profile
10	PWV measurement range	Maximum 30 mm
11	Water vapor retrieval	Atmospheric layer inversion via OEM
12	Data extraction interface	Data storage and extraction via ethernet connection
13	General characteristics	Plug and play

The description of the instrumental requirements of the CePIA 22 GHz radiometer in table (4.1) are described below, but for a much more detailed discussion on the validations and verifications of the requirements that are more technical and needed more in-depth analysis than allowed their choice, it is found in B.

Center Frequency

Ground-based radiometers observe the pressure-expanded emission lines of rotational transitions by water vapor in the atmosphere at specific frequencies in the microwave part of the spectrum. It is chosen to take the frequency of 22.235 GHz, because this emission line can be observed at sea level, at altitudes lower than 4000 masl, and in regions with a high concentration of water vapor in an almost continuous way, so it is suitable to observe from the city of Concepción and also from Cerro Ventarrones (2603 masl), which can generate data sets long-term global conditions, which are crucial for climate research.

Frequency range

The frequency range in the electromagnetic spectrum to be used depends on the central frequency of interest; figure (4.5), 20 to 26 GHz is chosen to have different three Nyquist zones covering 2 GHz in the ADC sampling.

IF Bandwidth

The IF bandwidth is the result of the heterodyne design of the receiver through the use of mixers. The received signal, called a radio frequency or RF signal, is translated into a different frequency, intermediate frequency IF signal, before being detected by a data logging system. The original signal is fed into a mixer, which is a nonlinear circuit element in which the RF is combined with a constant-frequency signal generated by a LO local oscillator, producing a signal whose frequency is the difference between the RF and LO frequencies $\nu_{IF} = \nu_{LO} - \nu_{RF}$ (section 3.1.1). Moreover, in our case, the received RF signal is in a range between 20 – 26 GHz; when going through the process of mixing or heterodyning of frequencies, this signal becomes an intermediate frequency IF tuned between 0 - 6 GHz, that is, 6 GHz as IF bandwidth, allowing a better adjustment to the profile of the water vapor line.

Portability

The need for radiometers to be used in measurement campaigns, that is, for a person to be able to transport them, access remote places, handle them easily and be able to cover a range of altitudes, as well as serve as a complement to other measurement techniques, is has increased in recent years, in this way it is possible to obtain a global database with special emphasis on the study of climate, according to trends and seasonal variations.

Among the most outstanding is MIAWARA-C; this radiometer has participated in campaigns in Bern (Switzerland), Zugspitze (Germany), and the Arctic Research Center of the Finnish Meteorological Institute in the US Mohave 2009 campaign Stiller et al. (2012), among others. It is worth mentioning that the whole instrument: the frontend, backend and the computer, is placed in the same case with a rain hood that closes automatically to prevent damage to the instrument when there is precipitation or strong winds and can be controlled remote form.

For this reason, and due to the reduced architecture designed, the 22 GHz CePIA radiometer can keep pace with the needs in water vapor research. It is expected that this instrument can be used for measurement campaigns and in the open field. For industrial use, it is positive to establish the portability requirement.

Backend type

The backend corresponds to the last part of the chain of electronic components of a receiver, in charge of digitizing and processing the IF signal. First, radio signals must be spectrally analyzed to obtain spectral line information.

An FFT digital spectrometer consists on an ADC (Analog-Digital Converter), that samples the electric field of the incoming signal periodically, taking the amplitude measurements of the analog signal, and then this sampled signal corresponds to a discrete signal in time. In the same way, it assigns a single output level to the samples

and binary codes to the obtained levels; that is, the ADC samples quantizes and encodes the incoming signal; then, the samples are processed directly by an FPGA (Field Programmable Gate Array), a large collection of logic gates that calculates the FFT in real time, and thus be able to measure the PSD.

Unlike other spectrometers used in other radiometers on the market, digital FFT spectrometers offer some advantages, including temperature stability that allows longer time intervals without calibration, costs are significantly lower, and since the FFT does not requires a laser, the limited lifetime of a laser is not a concern; that is why for this prototype radiometer it is considered to take into account a digital spectrometer for the digital backend.

Measurement altitude range

Two essential parameters that need to be established in advance in a spectrometer are the bandwidth and the spectral resolution; they indicate the lower and upper in height, respectively, to set the altitude where we want to observe the water vapor emission line at 22 GHz.

The upper limit measurement altitude is governed by the altitude at which the spectral line is predominantly Doppler rather than the amplified pressure, which occurs at approximately 80 km for water vapor, where the peak at 22.235 GHz is appreciable. (see figures 5.11 and 5.12) from which there is the most significant possible amount of information on water vapor in the stratosphere and mesosphere; On the other hand, the lower limit altitude for the recoveries is governed by instrumental considerations and not by the physics of the measurement, which is given by the altitude at which the bulging pressure in half the width of the line is equal to the width of the line spectral measurement band Nedoluha et al. (2011), so, it is also possible to carry out measurements at low altitudes.

These qualities allow the project to cover sea-level observations since the 22 GHz line allows it up to 80 km high.

Bandwidth/channel

The design of spectrometers focuses on obtaining the spectral information (spectral lines) contained in the radiation captured by the antenna, the spectral resolution that corresponds to the width of the spectral channels of the spectrometer should be small, and the smaller the width of the channels, the higher the spectral resolution of a spectrometer will be for a given IF bandwidth.

Because it is desired to observe up to a height of 80 km in the atmosphere, for this, it is necessary to observe in greater detail, or rather, with a good resolution, the peak of the profile of the line that contains the necessary information on the concentration of water at that point. For this reason, it is decided to obtain ten spectral samples of the peak in question. For this, the width of the channel is increased in the order of

kHz in order to be able to observe the upper mesosphere or stratosphere; that is, at this height, the basis of success is to increase the spectral bandwidth of the measurement. However, for the observation of the lower atmosphere, a larger spectral bandwidth is required in the order of MHz since it is not necessary to focus so much on the peak, which in fact, is not so predominant at the level of the troposphere, besides of the high variability present there.

For the CePIA 22 GHz radiometer, since the sampling frequency given by the digital processing board manufacturer is 4096 GHz and the number of elements is 65536, so $\frac{F_s}{N} = \frac{4096GHz}{65536} = 62.5$kHz. This is acceptable because it is in the kHz range, and it is possible to make observations in the upper atmosphere, up to 80 km, and make adjustments for the troposphere and middle atmosphere (section 4.2.2).

Number of channels

To implement the digital spectrometry function in the 22 GHz radiometer, it is necessary to work with the FFT (Fast Fourier Transform). The FFT is an efficient algorithm developed to calculate the DFT (Discrete Fourier Transform), widely used in signal and image processing. The DFT corresponds to the linear transformation of a vector in time to a vector in the frequency domain. It requires that the input function by a discrete sequence of finite duration, only evaluates enough frequency components to reconstruct the finite segment that it has analyzed.

The time needed to measure the power spectrum of an astronomical signal can be reduced by a factor of *n* if the spectrometer is built using *n* filters and integrators. This requires *n* independent channels simultaneously measuring different parts of the Sapunar Opazo (2015) spectrum. The digital card for the CePIA 22 GHz radiometer supports a transform length of up to 65536 elements to have a better spectral resolution that allows the analysis of the middle and lower atmosphere. Considering that the maximum bandwidth offered by the spectrometer is 4 GHz, in this case, the number of channels in multiples of 2 that enter the spectrometer with a resolution already evaluated in the previous section that turned out to be 62.5 kHz is sought; this is done since the algorithms in the digitizers work well to activate multiples of base 2, in this case, $65536 = 2^{16}$, this will be the default value.

Measurement objective

The emission spectra can be measured with the water vapor radiometer at 22 GHz due to the pressure expansion of this emission line at the tropospheric, stratospheric, and mesospheric levels. An optimal estimation algorithm can be applied using the inverse theory, which consists of the inversion of generally non-linear functions. The quantities to be recovered are continuous functions, and the measurements are discrete quantities. This allows obtaining the distribution of the water vapor profile with previous considerations of stratification of the atmosphere.

PWV measuring range

According to the characteristics of the instrument and the emission line of interest in this case at 22 GHz, which is asymmetric, and according to the water vapor measurement maps on the Earth's surface and in the simulations for the water vapor is established as a maximum limit in the range up to 30 mm, since in the measurements in Cerro Paranal of the 12 years of data they showed that the maximum registered of PWV is 30 mm (private conversation in CePIA, article not yet published).

Water vapor retrieval

An efficient way is needed to convert the spectral measurements of the water vapor profile at 22 GHz to a vertical profile of water vapor, which indicates its quantity and variability in a density column, for which strategies can be used. That, for now does not require long processing times. Using an Optimal Estimation Method can meet this requirement since it analyzes the integration of this code to the online computer system of the instrument.

Data extraction interface

According to the digital functions, a graphical interface is generated that works to display the control and monitoring variables. In addition, the result of the pseudo-correlation can be known. Also, you can modify the variables to optimize the balance and magnitude control. The results obtained are delivered by a text file and can be used and replicated by a user, all this by storing and extracting data through an ethernet connection.

4.1.2   Analysis of sensitivity

A receiver must be sensitive, that is, capable of detecting weak signals in the presence of noise. As with any other measurement device, there are limits to this sensitivity, as the receiver input and the receiver itself produce noise. This shows that variations in output power caused by variations in gain go directly into the determination of the limit sensitivity and depend on different factors. In the literature there are different amounts of this parameter that will depend on the type of radiometer and the height range to be measured.

The sensitivity is defined by the radiometer equation, which is an important figure of merit in the radiometer, according to equation (3.11). In the case of the 22 GHz CePIA radiometer, a system temperature of 120.4 K (T_{sys}) is estimated, over a single channel of width of 62.5 kHz ($\Delta \nu$) and an estimated integration time of 0.8 s (τ), the sensitivity will be about 0.54 K.

An effective verification method to check the sensitivity is through a calibration (see section 3.1.7). By measuring the receiver noise temperature, which is related to the amount of noise the system introduces into the received signal, it can be estimated using the *Hot/Cold* test, or also known as *Y -factor* , obtaining as a result a graph of
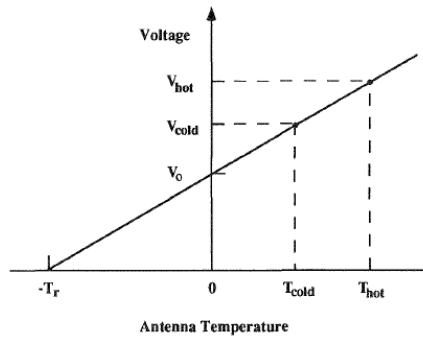
FIGURE 4.3. Calibration of antenna temperature using a hot and cold load. The calibration coefficient is given by the measured slope, and the voltage intercept for zero antenna temperature determines the receiver temperature T_r. Source: Janssen (1994)

the trend line corresponding to a straight line whose information is represented as the minimum detectable noise temperature; figure (4.3).

This method using liquid nitrogen is used to obtain an absolute calibration (section 3.1.7); this kind of absolute calibration is for stable systems, absolute calibration is not required as often, but for variable or unstable systems, absolute calibration (*Y-factor*) should be done more frequently.

On the other hand, the design of the radiometer consists of the use of an internal calibration, using a noise diode, or calibration of internal sources (T_L), which is a relative calibration that is much easier to maintain over time, so the stability of the system is relevant. The noise associated with this load T_L is known and from time to time, by means of a switch, it is possible to switch the radiometer from measurement mode to calibration.

4.2 Architecture of the radiometer

In the design of the CePIA 22 GHz tuned radiometer, an instrument with the characteristics described in section (4.1.1) is proposed, which allows a better tuning with the vapor line profile of water and an improvement in the noise temperature, conserving the phase.

The schematic diagram or architecture of the 22 GHz water vapor radiometer is presented in figure (4.4), which includes three (3) stages: analog frontend, analog backend, and digital backend. The analog and digital stages will be explained in the following sections.

4.2.1 Analog part: frontend and backend

The first stage of the radiometer (analog frontend) is composed of an antenna or horn, which receives the intensity of the electromagnetic radiation of the emitting body,
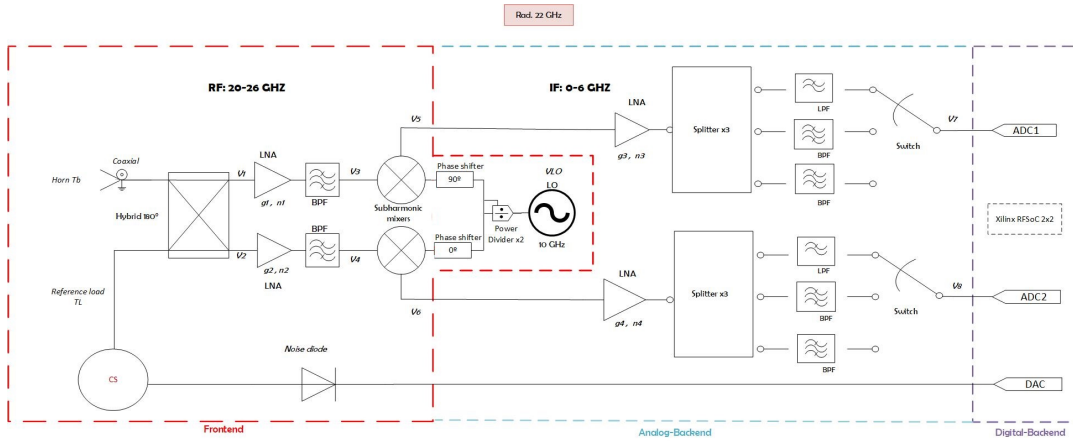
FIGURE 4.4. Schematic design of the 22 GHz radiometer proposed in this thesis. In the dotted lines are the most important stages. Red denotes the analog or RF frontend stage, in which the signals from the environment T_b and the noise diode that acts as internal calibration T_L are introduced, and they are mixed with a signal originated by a local oscillator that provides a signal from IF intermediate frequency output later indicated as the analog backend stage framed in blue, this analog signal in both branches enters the digital stage or digital backend which is the purple box, which represents the ADCs and the DAC of the digital card.

that is, the brightness temperature T_b and and it is assumed that $T_b = T_a$ (antenna temperature).

In addition, the instrument receives the temperature of a known internal load whose temperature is called T_L and passes through a switch CS, monitored in real time and allowing the system to self-calibrate.

These two temperatures are combined and compensated by a 180° hybrid whose outputs are indicated as V_1 and V_2. Two branches continue, figure (4.5), whose signals are amplified (g_1 and g_2, respectively) by an LNA (Low Noise Amplifier) to increase the power of the incoming signal much higher above the noise power generated thermally in the following components, thus improving the sensitivity without considerably increasing the noise even though each amplifier has a noise figure (n_1 and n_2, respectively); followed by a BPF (Bandpass Filter) that passes only the frequencies located within the determined RF bandwidth (20 - 26 GHz) and attenuates those that are outside this width, whose outputs are denoted by V_3 and V_4, the fact that these filters are prior to the mixer stage allows band rejection, and when the signal leaves the mixers it only has one band.

These signals are fed into two mixers (which are non-linear circuit elements) where they are combined with a constant frequency signal generated by a 10 GHz local oscillator.

The signal that comes out of the LO is divided into a power divider, in such a way that it is distributed for both mixers, figure (4.5), for this particular design opts for subharmonic mixers, whose outputs express the difference between the RF signal and LO in a harmonic multiple of the LO signal (the second harmonic of the signal), in simple
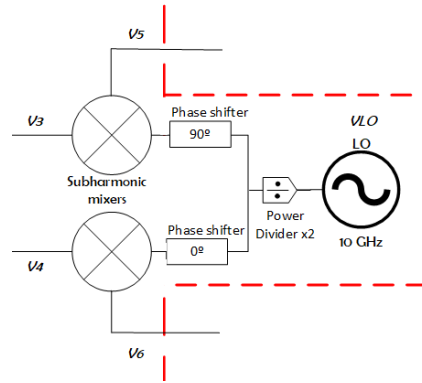
FIGURE 4.5. Diagram of the signal passing through the LO and mixers.

terms, the frequency that is entering from the LO is multiplied by two (2).

This power divider preserves the LO frequency but the power for each branch decreases by $-3dB$. Then in each node, there is a switch that applies a phase shift or PS (phase shifter) at 90° controlled by FPGA, which modulates the signal in phase, and allows the outputs of the mixers (because they are subharmonic), there is a 180° difference between them. This effect is then demodulated from the digital data, suppressing $1/f$ fluctuations that improve the sensitivity of the radiometer. For the respective outputs (V_5 and V_6) the unwanted products are then excluded from the mix and there is a signal IF, $\nu_{IF} = \nu_{RF} - 2\nu_{LO}$.

In the second part of the receiver, called the analog backend, there are the amplifiers in the IF stage, with their associated gains and noises (g_3, n_3, and g_4, n_4 respectively), and finally, in this analog section, each node finds a switch which allows the signal to enter one of the BPFs in the IF stage (0 - 2 GHz, 2 - 4 GHz and 4 - 6 GHz), to later be analyzed in the digital stage. The analog system outputs are named V_7 and V_8 for each node.

4.2.2 Digital part

The scientific objective of this prototype water vapor radiometer tuned to 22 GHz is the characterization of the atmosphere at a vertical level by means of spectrometry and analysis of the emission line of water vapor at 22 GHz. It is for this reason that it requires a robust digital backend, of high quality and capacity, that meets the instrumental requirements with ease.

This radiometer is a single sideband heterodyne receiver that converts the incoming 22.235 GHz signal to an intermediate 6 GHz frequency in one mixing step. Among its requirements is that the signal must be analyzed using a digital spectrometer since the state of the art in backend devices for real-time spectral analysis corresponds to FFT (Fast Fourier Transform) spectrometers. In addition to considering a bandwidth range of 0 to 6 GHz and a spectral resolution of 62.5 kHz. That is, the radiometer system must measure the emission of water vapor at frequencies between 20 and 26 GHz at

very high resolution.

The digital backend is the last stage of the schematic design shown in figure (4.6), responsible for digitizing and processing the signal (IF) to obtain the desired information, and can be designed in such a way that it acts in diagnostic mode, performing functions such as supply voltage and temperature control by placing the components on a peltier plate. Also, in operation mode, $1/f$ suppression, data integration, digital spectrometry, phase and magnitude balance, 180º digital hybrid, noise diode control, analog frontend current monitoring, temperature monitoring and control and communication.

It is necessary to comply with the requirements of vertical profile retrieval (as specified in chapter 5), for which there is an approach where is to use the full spectral resolution of the instrument (62.5 kHz) at the center of the line and the full available bandwidth of the spectra (6 GHz) for different altitude purposes, with noise-free and simulated full-power spectra, and artificially added noise with a certain standard deviation (σ). Retrievals in this way show promising results with high sensitivity in both the troposphere and mid-atmosphere, and increased sensitivity. However, as soon as noise is added, the mid-atmosphere sensitivity decreases rapidly Bleisch and Kämpfer (2012). At these altitudes, measurements are limited by signal/noise, resulting in both decreased sensitivity and increased vertical resolution Nedoluha et al. (2011). So, in this case, it is convenient to make temporary adjustments and consider some parameters such as the station, the city, a priori height profiles, and others at the time of taking the measurements Haefele et al. (2009).

It is due to these reasons that the choice of the digital processing board must be in accordance with the proposed objectives, in which different modules can be implemented that allow the data to be processed in a coherent way and that it be of good performance. Since there are no digitizers from 0 to 6 GHz that comply with this spectral resolution for which atmospheric recoveries can be made up to 80 km, it is necessary that the digital processing board can be configured in such a way that approximately 65000 channels are considered, and thus cover the necessary altitude of the study.

Thus, it has been designed that the first stage of the backend process is the digitization of the intermediate frequency signal IF, for which two high-speed ADCs are used, one for each output. The signal must be sampled in such a way that the data taken can accurately reconstruct the analog signal. An ADC is a device that converts an analog signal to a digital signal, binary numbers that represent amplitudes (usually voltage).

Digitizing a signal requires three steps: sampling, quantization, and encoding. In sampling, measurements of the amplitude of the analog signal are periodically taken and the sampled signal corresponds to a discrete signal in time; for quantization, a single output level is assigned to samples within a voltage range (voltage or level quantization); and encoding consists of assigning binary codes to the levels obtained in the

quantization.

To achieve this, specific criteria, such as the Nyquist-Shannon sampling theorem, must be met when sampling the signal. This theorem shows that the exact reconstruction of a continuous signal from its samples is mathematically possible if the signal is frequency limited and the sampling rate is greater than twice its bandwidth Smith et al. (1997), that is

$$F_{sampling} \geq 2B_{signal} \tag{4.1}$$

Suppose this criterion is not met when sampling a band-limited analog signal. In that case, it cannot be correctly reconstructed from the discrete signal because high-frequency signals will appear in the fundamental band as lower-frequency signals, producing a different signal to the original; this effect is known as aliasing Sapunar Opazo (2015). In the same way, it is important to consider that the filters used in the analog IF stage have a pronounced drop so that it finds couplings in the conversion rates.

In this design the signals go through a demodulation stage of the samples delivered by the ADC (the phase shift control). The demodulated samples are integrated, received, accumulated and stored in parallel, to then pass to the spectrometers where the spectra or PSD (power spectral density) are formed that can analyze the signals through the FFT maximizing the resources of the hardware with a high spectral resolution of 62.5 kHz, but which in turn can be modified depending on the atmospheric layer to be studied, and a large number of spectral channels (65536) to maintain a high dynamic range. The spectrum is divided into three (3) bands of 2 GHz each, these bands are displayed with 4.096 GSPS digitizers, and the different bands are sampled with the same type of digitizer but in different Nyquist zones, following equation (4.1).

It is essential that the balance in phase and magnitude of the signals be considered among its models, where the differences in phase and magnitude generated in the analog stage are equated between both branches delivered to the digital system, allowing the correct calculation of the posterior pseudo-correlation and requiring the use of complex adjustment factors that must be calculated in the calibration mode. Finally, go through a digital hybrid for the calculation of pseudo-correlation. All in such a way that an adequate baseline is considered that allows lower measurement limits in the troposphere. The result and monitoring data are taken to a module to be sent to the PC, and the 3 spectra produced by each section are expected to generate the complete total spectrum.

Based on these considerations, the chosen card corresponds to the Xilinx RFSoC 2x2, which contains two ARM processors in its System on a Chip (SoC), 2 ADCs with a resolution of 12 bits, and a sampling frequency of up to 4096 GHz. , 8 GB of DDR4 memory (4 GB available in the processing system (PS) and 4 GB in the programmable logic (PL)), two Pmod ports, one SYZYGY STD port and various I/O connections, such as 4 USB ports and an 11-gigabit Ethernet port. There are 850,560 flip-flops, 1,080 BRAM, and 4,272 DSP blocks on the FPGA side.
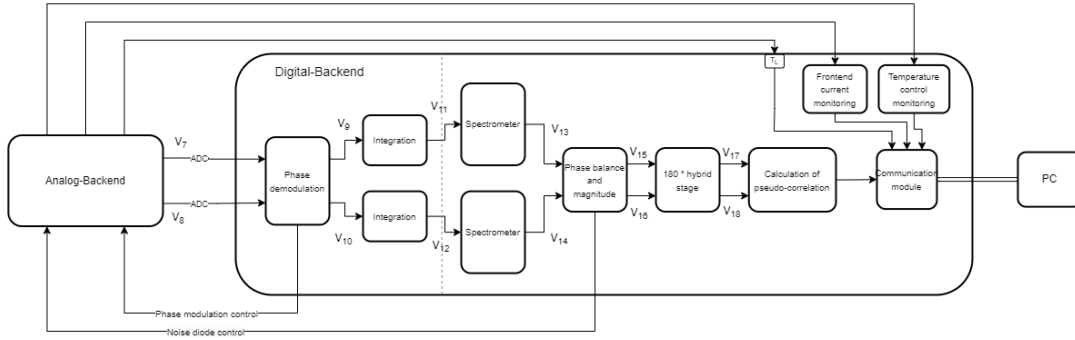
FIGURE 4.6. Schematic diagram of the digital backend for the CePIA 22 GHz radiometer. The sequence of the modules to be implemented is shown, and the monitoring of the signal in each one. Source: CePIA.

4.3 Analytical description of the signal

The input signal is attributed to everything coming from the sky in the line of sight, with the main signal of interest being the atmosphere. The signal from the atmosphere enters the receiver through the horn, and the radiation pattern is assumed to cover the source completely; hence $T_A = T_b$.

For the 22 GHz radiometer at CePIA (see figure 4.4), the input signals a are the atmospheric signal received by the horn T_b and the reference load signal T_L. Considering that the components are ideal, the input signal voltages are considered to be expressed:

$$V_{Tb} = V_{Tb} cos \left(\omega_{LO} + \omega_{IF/USB} \right) t + V_{Tb} cos \left(\omega_{LO} - \omega_{IF/LSB} \right) t \tag{4.2}$$

$$V_{TL} = V_{TL} cos \left(\omega_{LO} + \omega_{IF/USB} \right) t + V_{TL} cos \left(\omega_{LO} - \omega_{IF/LSB} \right) t \tag{4.3}$$

These RF voltages are transmitted and enter a 180° hybrid and branch out into two branches. A 180° hybrid is a four port network with a phase shift of 180°, when two voltages are input to two ports, one output port will contain the sum of the two inputs, while the other port will contain the difference between them, figure (4.7).
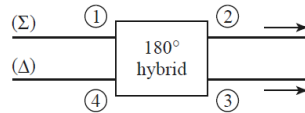
FIGURE 4.7. Symbol for a 180° hybrid junction. Source: Pozar (2011)

The outputs are expressed by a single symmetric matrix, figure (4.8), which implies the specific phase shift between the input and output ports. Hence, the outputs of the hybrid are V_1 and V_2.

$$V_1 = \frac{-j}{\sqrt{2}} \left(V_{Tb} + V_{TL} \right) \tag{4.4}$$

$$V_2 = \frac{-j}{\sqrt{2}} \left(V_{Tb} - V_{TL} \right) \tag{4.5}$$

$$[S] = \frac{-j}{\sqrt{2}} \begin{bmatrix} 0 & 1 & 1 & 0 \\ 1 & 0 & 0 & -1 \\ 1 & 0 & 0 & 1 \\ 0 & -1 & 1 & 0 \end{bmatrix}$$

FIGURE 4.8. 180° Hybrid Matrix S. Source: Pozar (2011); Maas (1986).

After the hybrid, in each branch, it is considered to include a low noise amplifier (LNA) and a band pass filter (BPF) considered a block. The amplifiers have gain g_1 and g_2, and a loss is associated with them that increases the noise temperature of the system, n_1, for each respective branch. This design allows for a single sideband (SSB) configuration where one sideband (USB) is eliminated. The outputs are the voltages V_3 and V_4:

$$V_3 = g_1[V_1 + n_1] = g_1 \left[\frac{-j}{\sqrt{2}}(V_{Tb} + V_{TL}) + n_1 \right] \tag{4.6}$$

$$V_4 = g_2[V_2 + n_2] = g_2 \left[\frac{-j}{\sqrt{2}}(V_{Tb} - V_{TL}) + n_1 \right] \tag{4.7}$$

$$V_3 = \frac{g_1}{\sqrt{2}} \left[V_{Tb}\cos\left(\omega_{LO} + \omega_{IF}\right)t + V_{TL}\cos\left(\omega_{LO} + \omega_{IF}\right)t + n_1\cos\left(\omega_{LO} + \omega_{IF}\right)t \right] \tag{4.8}$$

$$V_4 = \frac{g_1}{\sqrt{2}} \left[V_{Tb}\cos\left(\omega_{LO} + \omega_{IF}\right)t - V_{TL}\cos\left(\omega_{LO} + \omega_{IF}\right)t + n_2\cos\left(\omega_{LO} + \omega_{IF}\right)t \right] \tag{4.9}$$

Behind this "block" are the mixers, one for each branch, which, together with the LO and the incoming RF signal, produce a lower bandwidth signal or lower frequency intermediate signal (IF).

The mixing process can change the signal phase by a constant value, so there is a phase shifter (PS) for each branch (represented by ϕ). These calculations will be 90°, so multiply by two (2) for the subharmonic mixer, which will modulate the phase and give the mixer's output a difference of 180°.

The expression for the LO voltage is:

$$V_{LO} = V_{LO}\cos\left(\omega_{LO}t + \phi\right) \tag{4.10}$$

The input signals V_3 and V_4 are multiplied by the V_{LO} signal.

$$V_5 = KV_3 \times V_{LO}^{\phi=180°} \tag{4.11}$$

$$V_6 = KV_4 \times V_{LO}^{\phi=0°} \tag{4.12}$$

It is assumed that K is the mixer constant that indicates the efficiency of the element. The outputs V_5 and V_6 are:

For $\phi = 180°$, V_5 is:

$$V_5^{180°} = \frac{KV_{LO}g_1}{\sqrt{2}} \left[V_{Tb}cos(\omega_{IF}t) + V_{TL}cos(\omega_{IF}t) + n_1cos(\omega_{IF}t)\right] \qquad (4.13)$$

For $\phi = 0°$, V_6 is:

$$V_6^{0°} = -\frac{KV_{LO}g_1}{\sqrt{2}} \left[V_{Tb}cos(\omega_{IF}t) - V_{TL}cos(\omega_{IF}t) + n_1cos(\omega_{IF}t)\right] \qquad (4.14)$$

For the analog backend, the IF stage amplifier and switch-selected filter are again considered as one block. Taking into account the gain of the amplifier (g_3 and g_4, respectively for each node) and the noise of both branches (n_3 and n_4, respectively for each branch), the outputs V_7 and V_8 are:

$$V_7 = g_3(V_5 + n_3) \qquad (4.15)$$

$$V_8 = g_4(V_6 + n_4) \qquad (4.16)$$

$$V_7 = \frac{KV_{LO}g_1g_3}{\sqrt{2}} \left[V_{Tb}cos\left(\omega_{IF}t\right) + V_{TL}cos\left(\omega_{IF}t\right) + \left(n_1 + n_3\right)cos\left(\omega_{IF}t\right)\right] \qquad (4.17)$$

$$V_8 = -\frac{KV_{LO}g_2g_4}{\sqrt{2}} \left[V_{Tb}cos\left(\omega_{IF}t\right) - V_{TL}cos\left(\omega_{IF}t\right) + \left(n_2 + n_4\right)cos\left(\omega_{IF}t\right)\right] \qquad (4.18)$$

where V_7 and V_8 are the respective inputs to the digital backend, figure (4.6) to the ADC.

After the ADCs in the digital backend stage, there is the phase demodulation module and then the integration modules, where the input data is accumulated in a bank, read one by one, and then averaged and sent.

$$V_{11} = \frac{1}{N}\sum\frac{KV_{LO}g_1g_3}{\sqrt{2}} \left[V_{Tb}cos\left(\omega_{IF}t\right) + V_{TL}cos\left(\omega_{IF}t\right) + \left(n_1 + n_3\right)cos\left(\omega_{IF}t\right)\right] \quad (4.19)$$

$$V_{12} = \frac{1}{N}\sum\frac{KV_{LO}g_2g_4}{\sqrt{2}} \left[V_{Tb}cos\left(\omega_{IF}t\right) - V_{TL}cos\left(\omega_{IF}t\right) + \left(n_2 + n_4\right)cos\left(\omega_{IF}t\right)\right] \quad (4.20)$$

The input signals in each spectrometer are V_{11} and V_{12}, there the signals change from the time domain to the frequency domain by means of the Fourier Transform.

$$\widetilde{f} = \int_{\infty}^{-\infty} f(t)e^{-j\omega t}dt \qquad (4.21)$$

This transform is applied to the voltage equations V_{11} and V_{12} whose outputs are:

$$V_{13} = \frac{\pi K V_{LO} g_1 g_3}{\sqrt{2}} \left[V_{Tb}\left(\delta_{IF}t\right) + V_{TL}\left(\delta_{IF}t\right) + \left(n_1 + n_3\right)\left(\delta_{IF}t\right) \right] \qquad (4.22)$$

$$V_{14} = \frac{\pi K V_{LO} g_2 g_4}{\sqrt{2}} \left[V_{Tb}\left(\delta_{IF}t\right) - V_{TL}\left(\delta_{IF}t\right) + \left(n_2 + n_4\right)\left(\delta_{IF}t\right) \right] \qquad (4.23)$$

To provide optimum sideband isolation, they are arithmetically outputs are recombined using calibrated weighting coefficients, that compensate for the phase and magnitude errors of the analog components. A signal can be used for calibrationthat is known to be in only one sideband can be used, even RFI, but it is convenient to provide a known calibration tone in the lab to ensure adequate S/N Morgan and Fisher (2010).

As described in Fisher and Morgan (2008), the gain amplitude ratio of the two channels is easily measured as the square root of the quotient of the time-averaged of the signal powers. Therefore, the gain or amplitude ratio χ, and the phase terms $(\varphi_{IF} \pm \varphi_{LO})$ for all frequencies in the IF passband are:

$$\chi = \sqrt{\frac{\left(V_{Tb}\overline{V_{Tb}}\right)}{\left(V_{TL}\overline{V_{TL}}\right)}} \qquad (4.24)$$

where V_{Tb} and V_{TL} are the voltage amplitudes. The phase term $(\varphi_{IF} - \varphi_{LO})$ can be determined from the cross product of V_{Tb} and V_{TL}:

$$\varphi = \varphi_{IF} - \varphi_{LO} = \tan^{-1}\left[\frac{Im\left(V_{Tb}\overline{V_{Tb}}\right)}{Re\left(V_{TL}\overline{V_{TL}}\right)} \right] \qquad (4.25)$$

where IF and LO are the phase unbalances in IF and LO. LO represents the phase unbalance at the ADC input due to RF and LO components, and IF the relative phase mismatch of the signal due to components analog after mixers.

The signals are out of phase with each other so that there is a compensation per channel or a balance in phase and magnitude, these constants or modification factors, equations (4.24) and (4.25), must be included in a branch; in such a way that can reach the hybrid stage with equal magnitude and 180° phase.

The outputs of the hybrid contain in one port the sum of the two inputs, while the other port has the difference between them,

$$V_{17} = \frac{-j}{\sqrt{2}}\left(V_{15} + V_{16}\right) \qquad (4.26)$$

$$V_{18} = \frac{-j}{\sqrt{2}}\left(V_{15} - V_{16}\right) \qquad (4.27)$$

In the output of the digital hybrid it is possible to obtain values for the pseudo-correlation for both $\phi = 0°$ and $\phi = 180$:

For $\varphi = 0°$

$$V_{17} = 2GkV_{Tb} + N \tag{4.28}$$

$$V_{18} = 2GkV_{TL} + N \tag{4.29}$$

For $\varphi = 180°$

$$V_{17} = -2GkV_{Tb} + N \tag{4.30}$$

$$V_{18} = -2GkV_{TL} + N \tag{4.31}$$

That is, each output of the spectrometer is directly proportional to the brightness temperature of the load or the input, and depending on the phase, which changes sign, the demodulation of the output provides a stable measurement over time.

For a better detail of the equations, see B

4.4   Data flow

The input signal at the horn goes through a into a 180º hybrid together with a T_L signal coming from a Noise Diode (ND) controlled by the digital backend. The hybrid's outputs are amplified and fed into band-pass filters, which remove a sideband from the center frequency. Then, the filtered signals are introduced to a mixer each, together with the signal coming from an LO, with the same objective of obtaining IF signals in a frequency range between 0 and 6 GHz. Subsequently, the signals are amplified, filtered, and introduced to two analog-digital converters (ADC) to be read by the digital backend.

Then, two voltage signals are delivered from the analog backend in a time-dependent waveform. There are three zones of 2 GHz width in the digital part; therefore, the complete spectrum covers the 0 - 6 GHz range. In the first instance, the wave or analog voltage signal is digitized by the ADCs. Quantization will preserve information, resulting in a better signal-to-noise ratio Wilson et al. (2009), figure (4.9).

Some considerations to take into account are that the target sampling frequency is 4 GHz and a quantization resolution of 12 bits. In addition, the Xilinx IP FFT to use supports a maximum of 65536 elements for the transform, so 65536 samples are taken per integration, resulting in a 62.5 kHz spectral resolution. This generates a digital integrator, multiplying the integration time by the power of 2 Le Vine and Skou (2006).
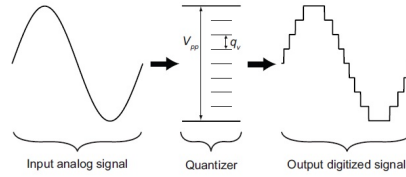
FIGURE 4.9. Quantization of an input analog signal Nanzer (2012).

Thus, the number of integrations that best meets these requirements is 16384, which translates into an acquisition time of approximately 0.8 seconds Palacios (2021).

The samples delivered by the ADC are demodulated; as inputs, the 500 MHz clock delivered by the ADC, the reset signal, and two 128-bit vectors (containing 8 samples of 12-bit). This demodulation module also controls the phase shifter and the correct delivery of valid samples to the integrator.

Demodulation consists of assigning a sign to the output samples depending on the state of the phase shifter. Here, it is convenient for sensitivity testing to have the ability to change the state of the phase shifter periodically after a certain number of integrations.

Samples are received, accumulated, and stored in 8 samples in parallel at a rate of 500 MHz. To work with all the samples, it is necessary to use two buffers, each made up of 8 BRAMs of $\frac{65536}{8} = 8192$ elements each.

Incoming samples pass through three input registers before being sign-extended and summed with the corresponding element stored in the bank. The result is stored in one last register before entering the buffer. Once the data has been integrated, the already processed buffer is read and integrated into the other buffer. The reading of the already integrated data is carried out thanks to two counters, these enter the spectrometers in a set of 65536, and some additional configurations, such as the data format, are chosen Palacios (2021).

Its design focuses on obtaining the spectral information contained in the radiation captured by the horn Sapunar Opazo (2015). The spectrometer modules are designed to measure the spectral density of a signal, which corresponds to the distribution of the power of said signal over the different frequencies by which it is formed, that is, its spectrum, known as the power spectral density (PSD). Moreover, this is done using methods to calculate the frequency response of a signal over time.

The PSD can be determined by using the Fourier transform (FT), v_t, to obtain v_v and then squaring v_v to obtain the PSD. FT can be performed using Fast Fourier Transform (FFT) algorithms Wilson et al. (2009).

Fourier analysis is a family of mathematical techniques based on decomposing signals into sinusoids, which can be used to calculate the spectrum of a signal over time. The Discrete Fourier Transform (DFT) is a member of the family that is used for digital (discrete) signals, which is the case of the application in a backend Sapunar Opazo (2015).

The DFT corresponds to the linear transformation of a vector x_n in time to a vector X_m, whose coefficients represent the charaxteristics of sinusoidal signals whose sums make up the signal in time; and, the FFT algorithms are categorized based on the number of small summations n.

In all this digital implementation, a high processing power is necessary, which is why an FPGA (Field Programmable Gate Array) is used, a device that contains a matrix of logic blocks whose interconnection and functionality can be configured through a description language. Specialized in most FPGAs, is possible to find high-level functions such as adders or multipliers embedded in the interconnection matrix, as well as memory blocks, allowing an excellent capacity for parallel processing, giving the possibility of processing large data widths real-time band Klein (2014).

The FFT will have two real and imaginary components that can be generated in the FPGA, and they are data that we can obtain. Then the balance function requires the use of complex adjustment factors that need to be calculated in the calibration mode, where the constants representing a digital hybrid are determined to reduce the total imbalances, equations (4.24) and (4.25).

This module has as inputs the clock, the reset signal, and a 160-bit data bus. The input data bus contains two complex values, whose real and imaginary parts. As outputs, there are also two complex values, but this time separated into their real and imaginary parts Palacios (2021).

For balance, the four components of the data bus are first separated. The components of the first channel are taken to an intermediate register to delay them by one cycle and then to the output register after a sign extension of 4 bits; the multiplication of each input by the corresponding correction factors is implemented, which are stored in two BRAMs of 65536 elements each Palacios (2021). Data can be extracted in the same way.

In the digital hybrid, complex addition and subtraction of the inputs are implemented, adding a bit to avoid overflow. The outputs are two real and two imaginary components. For the calculation of the pseudo-correlation, they are subtracted from the two complex values obtained after the digital hybrid. Thus, from two real and two imaginary components, one real and one imaginary are obtained. Since the digital hybrid and pseudo-correlation calculation modules are small, a testbench is created that simulates them together with the phase and magnitude balance module, where unitary correction factors are used for this simulation Palacios (2021). The result of the digital

pseudo-correlation is sent by USB to the computer for data storage and visualization of the resulting spectrum.

4.5 Characterization of the noise temperature

This section contains the calculations and simulations carried out with the AWR support software, specifying its properties and modes of use. AWR supports simulations that are consistent with the application of the Friis formula (equation 3.10), to represent the noise temperature of a system or receiver.

What is expected is to analyze the components of the diagram of the CePIA 22 GHz radiometer, and in this way discern those that represent the best result of the noise temperature of the analog system, data of great relevance to determine the sensitivity.

AWR is a software that has automation tools for high frequency electronic design and allows to know the theoretical performance of a receiver, for which the physical parameters of the components are introduced in the schematic design and their behavior is observed, being possible obtain some properties, such as the noise temperature of the system, which is very important for the further development of the instrument (for more details, see D).

4.5.1 Analysis of components

This section presents a theoretical investigation through a series of simulations developed from the prototype of a water vapor radiometer tuned to 22 GHz, which allows an understanding of the behavior of commercial electronic components before their acquisition and evaluating the a priori design of architecture in general. These simulations are performed with the AWR VSS software.

The design or architecture of the 22 GHz radiometer at CePIA, figure (4.4), had an evolution over time, which iteratively considered adding or removing some components and restoring the adequate bandwidth. Firstly, an exhaustive search is made of the commercial components that can integrate it, whose characteristics in frequency, noise figure, losses, and others, are the ones that best fit the scheme and allow a low noise temperature.

To have the final selection of components, simulations are made for each component and different combinations between them, discarding them for better performance.

It begins with individual simulations for each design element in the AWR software, for which the generic components shown in the software library and the indicated values of the most relevant characteristics of the components shown in the tabs are taken into account in the data; this to evaluate the noise temperatures individually.

At the same time, it is tested to determine which type of noise source can be the most optimal and which one represents an input of microwave signals in the receiver, considering various options in the software library. For the sky signal, T_b, is chosen to use the RN source block, figure (4.10, which models thermal noise into a noisy resistor; by default, the noise is white, although temperature and frequency-dependent resistors are supported, as well as including parameters by the user, among them the SMPFRQ, which is the sampling frequency of the generated signal, and also CTRFRQ, which is the central frequency of the complex surround signal.
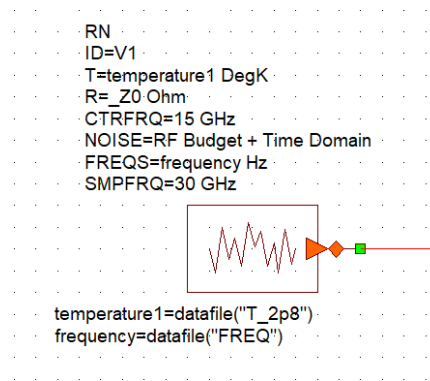
FIGURE 4.10. Input block, noise source RN. This block enters a signal to the system that can be programmable in such a way that it enters frequency and temperature data that resembles the measurement site.

Figure (4.11) shows an example of an amplifier simulation from some of the tests carried out, which includes an input source (in this case, a PORT SRC) that allows generating an input signal with certain specific frequency parameters, as well as a termination block (PORT =1) that can serve as a measurement source. Figure (4.12) shows another example of some tests carried out for characterization by the simulator in a mixer, with their respective sources, which exemplify the RF input signal and an LO input signal. Note that the most important parameters provided by the provider are included in each component.
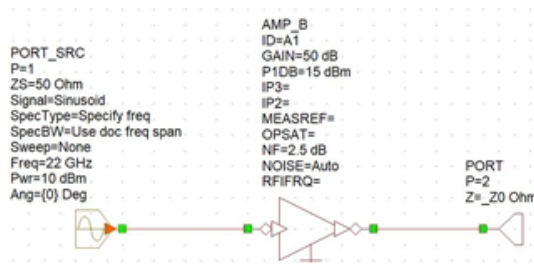
FIGURE 4.11. Evaluation in AWR of an amplifier. The data correspond to the datasheet of the SBL-1832733025-KFKF-S1 model from the Eravant company. The source and a final port are included for the simulation.

For the noise temperature in each simulation, the RF Budget option is used, and then C-TE is chosen, which calculates the equivalent input noise temperature; this in the simulation window allows adapting the type of simulation that is intended to be carried out (figure D.4).
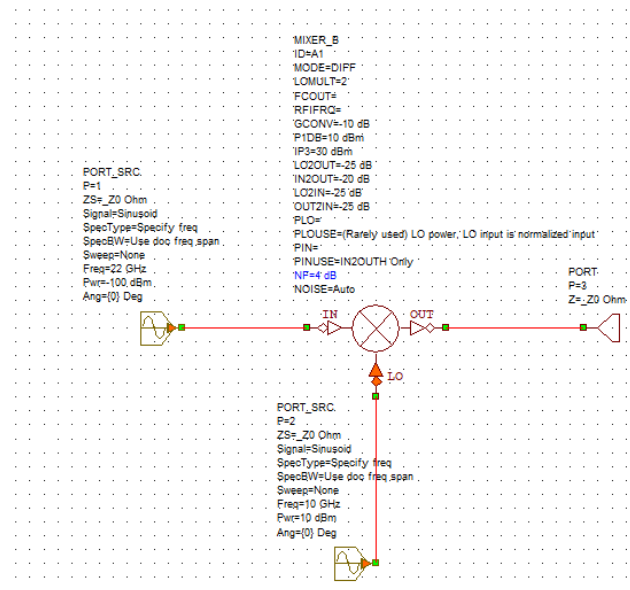
FIGURE 4.12. Evaluation in AWR of a mixer. The data correspond to the datasheet of the model TFDC-2030-10-DC6 from the Tuneful RF company. The source and a final port are included for the simulation. Another input source is attached that simulates the LO signal.

The results of the simulations in figures (4.11) and (4.12), where the noise temperature of the LNA and the mixer are reflected, are 225.70 K and 445.18 K, respectively. These results allow for choosing the components with the best results to be considered acquired.

An example is a figure (4.13); some initial tests are done with a source, the 180° hybrid, and the first LNA amplifiers. In the case of this figure, the same LNA is considered in both branches, but tests have previously been carried out with different LNAs in each branch to rule out the one that provides the highest noise temperature. In this case, the parameters of the LNA model TFMA-ULNM1826.5-30 from the company TUNEFUL RF are shown. Whose results for each branch of noise temperature is 240.3 K, and the gain is 28.99 dB.

It should be remembered that the parameters given in the supplier's datasheet are attached to each component to be evaluated, and the parameter-S files if they are provided. Also, it is essential to mention that the mixers are used in DIFF; that is, they subtract the input signal from the LO signal, following that $v_{IF} = nu_{RF} - nu_{LO}$, to perform heterodyning. In addition, the mixers are used as subharmonic; that is, the LO signal is multiplied by two (2).

After the first LNA of the RF stage, the other components that are part of the receiver continues to be placed; they can be incorporated directly into the AWR software and, therefore, into the receiver to be characterized. Thus, different analyzes can be performed using generic components of the library.

Finally, using comparison tables where the results of the simulations (at a specific
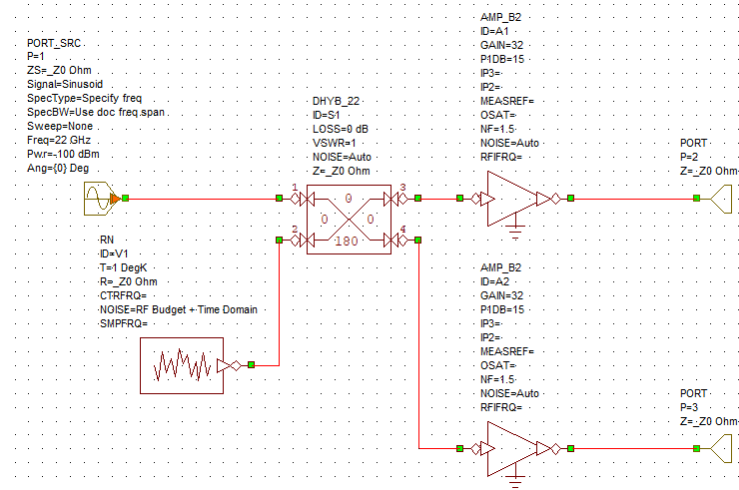
FIGURE 4.13. Schematic design of the first components of the radiometer receiver, to evaluate the noise temperature in the first part.

TABLE 4.2. Results of the noise temperature simulations on the analog frontend and backend for different mixers. The little difference between the values is appreciated for the generic component.

Mixer model	4 GHz
Tuneful RF	368.6 K
Narda-QUITED	369 K
Lambda	368.7 K
Eravant	369.2 K

frequency value) of noise temperature and gain in the configuration of each component are attached, it is possible to visualize the best commercial component options to acquire. Table (4.2) shows an example of a comparison of noise temperature results using different mixers; note that the differences are marginal.

These results make it possible to make the best choice of components to be purchased. Note the example of table (4.2), which reveals that the best option in the mixer model is the one offered by the company TUNEFUL RF.

4.5.2 System noise temperature

After determining the best component configurations to use in the radiometer, the following diagram (figure 4.14) is shown for the analog stage and figure (4.15) for the pseudo-correlation (involving the analog ensemble plus the hybrid of the stage digital).

In the diagram of the AWR system, the RN source is used as a source or input signal to the system. Table (4.3) of section (4.8) shows the components chosen to develop the following simulations. Remember that the frequency of the RF stage goes from 20 to 26 GHz. Therefore, the frequency used in the LO is 10 GHz, multiplied by two (2) in the mixers, to have the frequency range of the IF from 0 to 6 GHz.
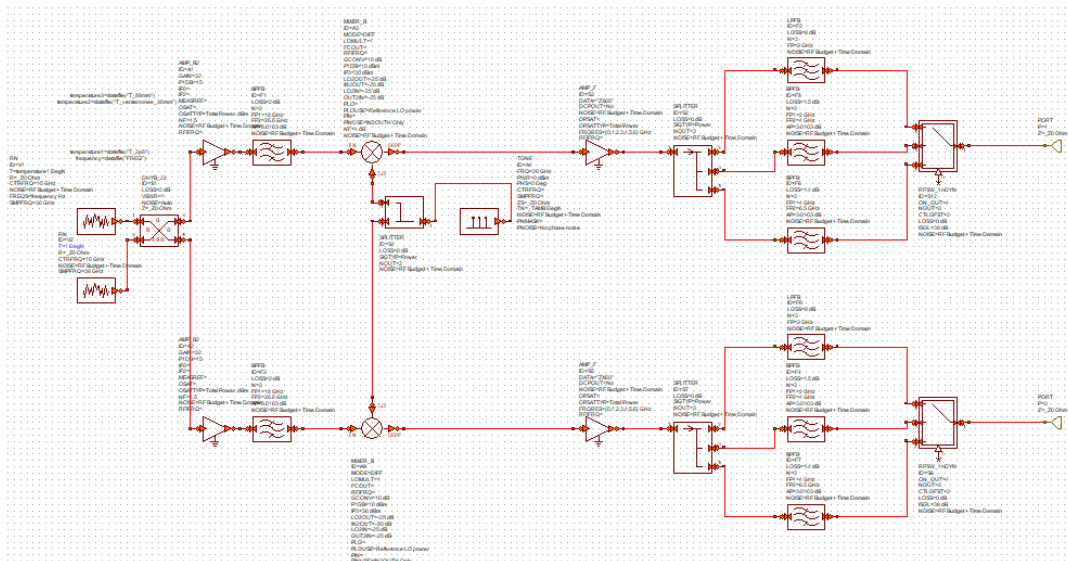
FIGURE 4.14. The analog frontend and backend diagram are shown with generic components.
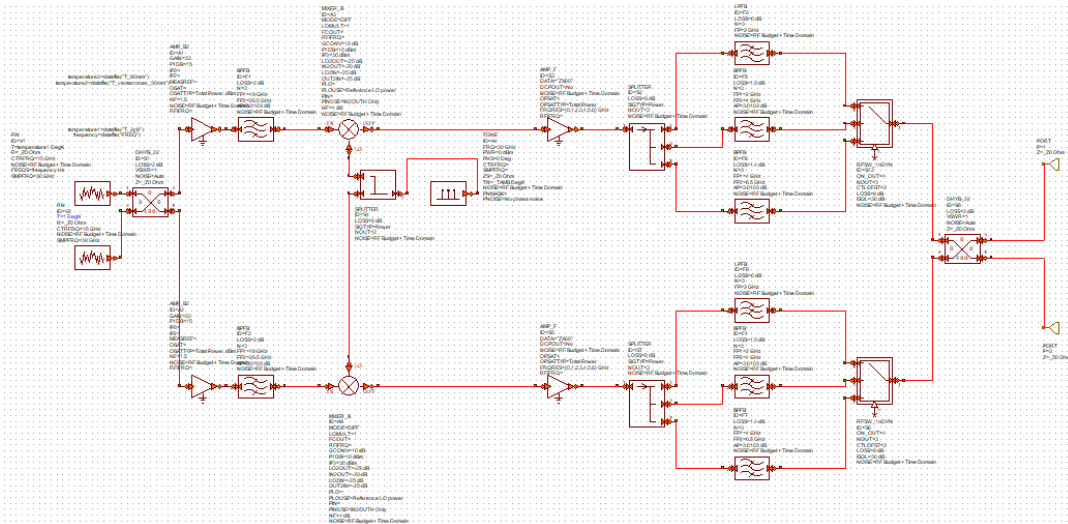
FIGURE 4.15. Diagram of pseudo-correlation, note the second hybrid.

As a generic component to represent the LO, a TONE is chosen from the AWR simulation library, which generates a sinusoidal tone in the complex envelope or as a real signal, where the power of the tone is specified and also supports phase noise modeling, thermal noise, and impedance mismatch.

It is observed in the same way in the IF stage; a divider divides the signal and takes it to the filters of this stage, which through a switch, will select the filter that will pass the signal to the digital stage.

Some adjustments are necessary to make the introduction of the component parameters as accurate as possible. Among them: the appropriate adjustments are made to correlate better the frequency cutoff of the filters (figure 4.16); the simulation carried out by AWR is superimposed with the parameters offered by the technical sheet and

the curve provided by the supplier.
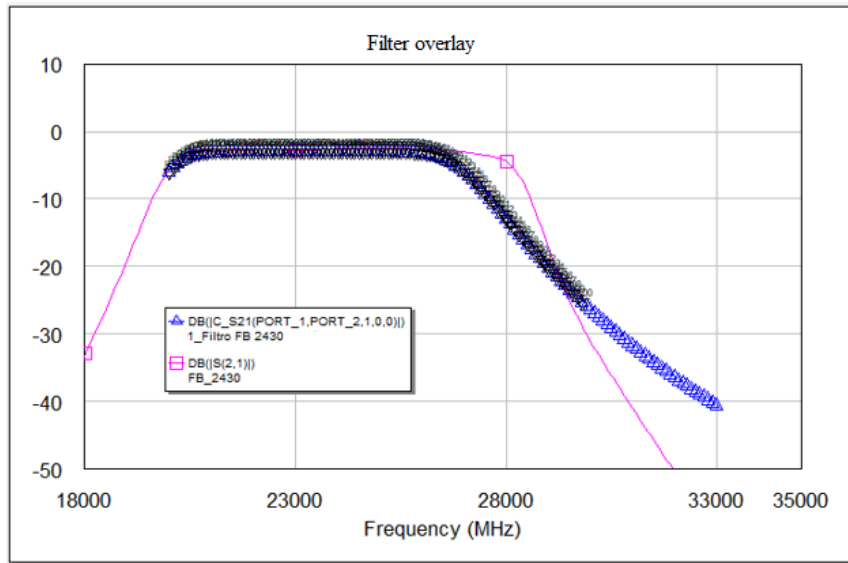
FIGURE 4.16. Component gain overlay in s2p file and sweep due to setting of pre-mixer filter characteristics are shown.

In the same way, some adjustments are made to the data that is entered into the amplifiers, and a file is loaded in which the most significant possible amount of data that the manufacturer offers to this component of the AWR library is attached, such as the S-parameters and the noise figure for each frequency, and thus the element is more similar to the actual component to be acquired, and in this way obtain more precise results in the calculation of the noise temperature and the gain of the system. Figure (4.17) shows the input file attached to the amplifier chosen for the IF stage, model ZX60-83LN-S+ from MiniCircuits, which contains the S-parameters.

FIGURE 4.17. Part of the text file included in the amplifier that contains the frequency, the S-parameters and the NF (noise figure).

Finally, a sweep simulation is performed to obtain the noise temperature (TN) using the AWR software (D). Specific tasks are executed to find this result. Figures (4.18) and (4.19) reflect the results, which are 241.8 K for the analog stage and 120.4 K for the pseudo-correlation (in which the 180° hybrid is included).

In the same way, using the Friis equation (3.10), the independent calculations of the noise temperature of the system were made to compare them with the AWR result

and demonstrate the consistency of the simulations. For the diagram without pseudo-correlation, the data obtained is 236.103 K, which shows coherence in the order of magnitude of both results and the similarity between them.

It is necessary to consider the numerical relationship between the noise temperature values with and without the pseudo-correlation. At the beginning of the analog scheme, there is a hybrid that acts as a power divider, which affects a factor of 2 in the noise and is what is reflected in the result of 241.8 K, which the last hybrid does not have in the output that allows pseudo-correlation, that both inputs are perfectly matched and allow an output with better performance in the noise of the receiver.
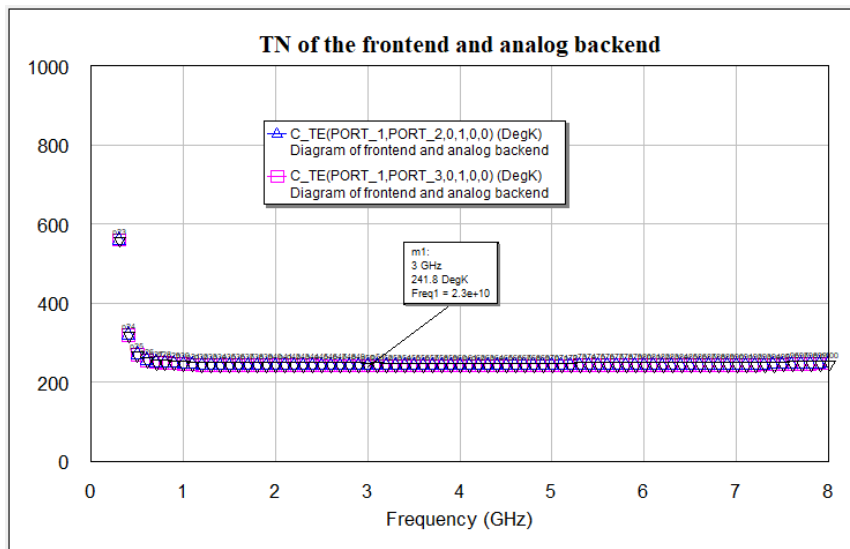
FIGURE 4.18. Result of the simulation of TN the scheme of the figure (4.16), shows the result of the noise temperature that is consistent with the one calculated independently by the Friis equation (3.10). The result is 241.8K.
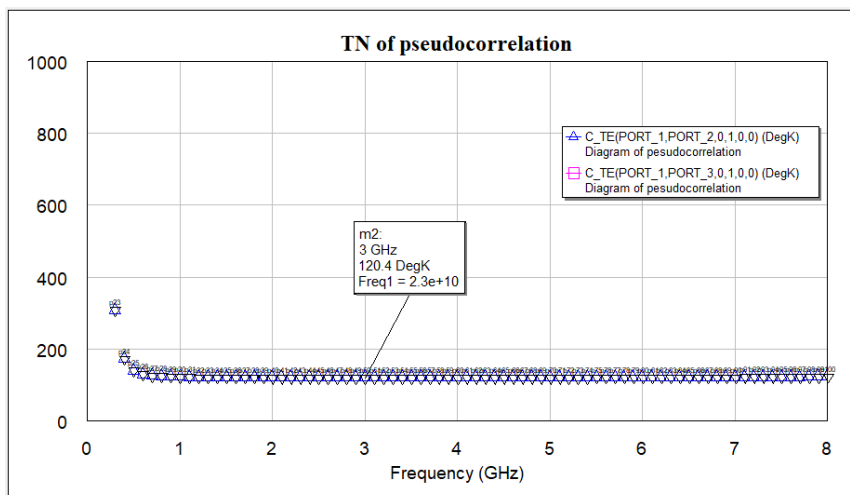
FIGURE 4.19. Plot of the pseudocorrelation result. The result is 120.4 K unlike the previous figure where it is evaluated without the pseudo-correlation. This is due to the position of the last hybrid that has uncorrelated inputs and therefore couples the outputs into one.

This pseudo-correlation noise temperature result is used to obtain the sensitivity of the CePIA 22 GHz radiometer.

4.6 Generation of an input RF signal

Using the AM software (D), it is possible to generate by simulation -by introducing certain variables- a set of output data that reproduces in the best possible way the frequency and brightness temperature of the site's atmosphere where it is expected to position the radiometer, Cerro Ventarrones. Furthermore, the AM can reproduce this data according to the PWV of interest. For the case exposed here, the average PWV of the study site is taken into account, that is, 2.8 mm.

This data, obtained in a text file, is entered into the AWR and attached to the source of entry to the system. The RN source is chosen as the signal generator that will allow the input of a signal with the characteristics of the T_b of the site in question so that it simulates as best as possible the signal that will be captured in the real atmosphere at that moment, the frequency in units of Hz and the power in units of W.

Figure (4.20) shows the input source to the system, with the specific necessary input values, such as SMPFRQ (samplig frequency) at 6 GHz and CTRFRQ (center frequency) at 23 GHz, because 23 GHz is the center measurement between 20 - 26 GHz and 6 GHz demonstrates the output bandwidth range of the analog backend; and, vectors indicating the text file input of the frequency and power that reproduces the input signal.
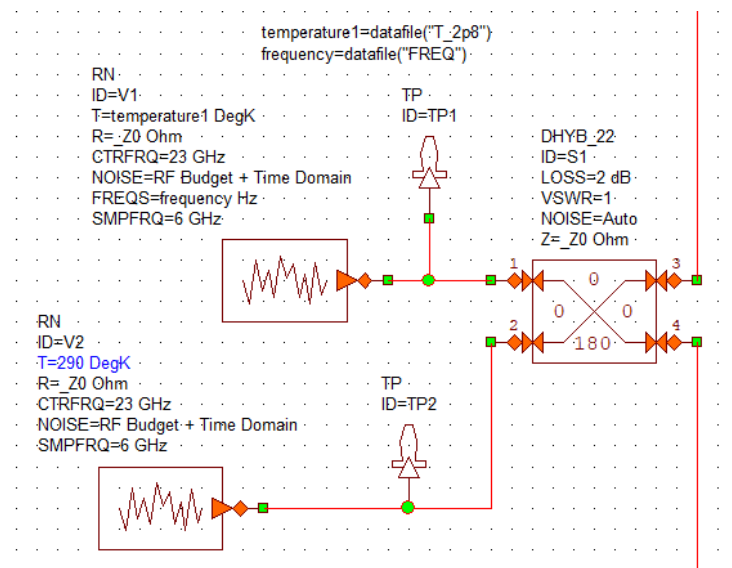
FIGURE 4.20. System input source. The input parameters and the vectors that indicate the frequency and power are reflected to generate the input signal that reproduces the T_b that the radiometer will measure at a PWV of 2.8 mm in Cerro Ventarrones.

In this case, with the input parameters of figure (4.20), the signal is input together with a generic noise signal to the 180° hybrid. Both signals are mixed and passed through the analog components. Figures (4.21) and (4.22) show the spectrum of this signal for each of the elements, reflecting the corresponding bandwidth.
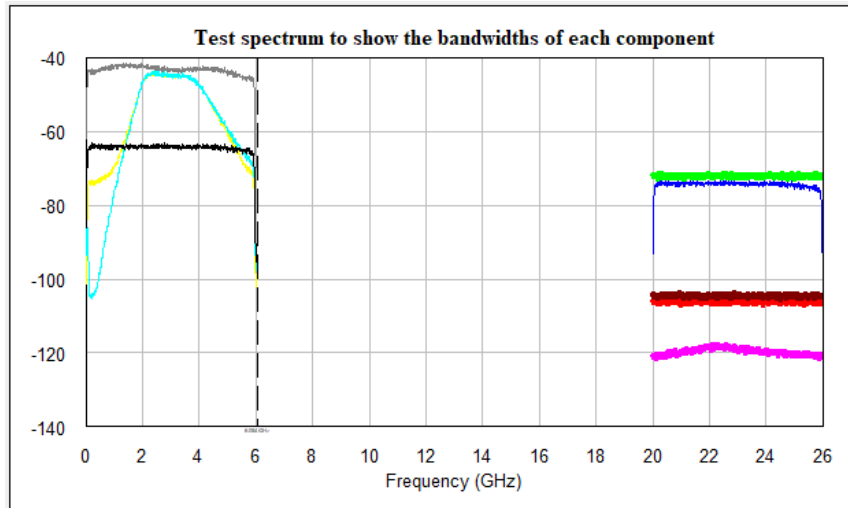
FIGURE 4.21. Spectrum of the signal as it passes through each component of the diagram. The Y axis indicates the power in dBm. Note the colors that differentiate each of the elements and their bandwidths. The pink line is the the input signal of the RN; the brown line shows the calibration signal T_L, the red line shows the signal that comes out for one of the branches after the first 180° hybrid, the green line shows the LNA RF, the blue line the BPF RF, the black and gray lines indicate the mixer and splitter output, respectively, the turquoise line indicates the output of one of the chosen IF filters (2 to 4 GHz), and the yellow line that is the output of the second 180° hybrid.

The figure (4.21) shows the pink line, which is the input signal of the RN with the AM data that simulates the PWV at 2.8mm and shows the peak in 22 GHz; the brown line shows the calibration signal associated with the known T_L, at a power of approximately -100 dBm; the red line shows the signal that comes out for one of the branches after the first 180° hybrid, where $V_1 + V_2$, are uncorrelated signals and their noises are added. The green line shows the LNA RF bandwidth and the blue line the BPF RF, between 18 and 26.6 GHz. The black and gray lines indicate the mixer and splitter output respectively, which are between 0 and 6 GHz. The turquoise line indicates the output of one of the chosen IF filters, in this case from 2 to 4 GHz; and, finally, the yellow line that is the output of the second 180° hybrid, since this graph shows the output between the ranges of the chosen filter, and therefore the pseudo-correlation of figure (4.16) and (4.19).

In this case, changing the input parameters in Fig. (4.21), such as SMPFRQ (sampling frequency) to 30 GHz and CTRFRQ (center frequency) to 15 GHz, to show a wide bandwidth covering the IF and the RF, but that represents the figure (4.19) in the same way, the figure (4.22); where in the same way the signal enters together with a generic noise signal to the 180° hybrid. Both signals are mixed and passed through the analog components and the corresponding bandwidth is reflected, where the colors that are reflected are exactly the same as figure (4.21), that is, that each color reflects the corresponding component in its bandwidth, only that it shows it in a larger sample.

4.7 Integrated power analysis and gain budget

Using the simulation in PWR-MTR in AWR, which calculates the average power in the time domain by specifying the frequency band, it is possible to obtain the total
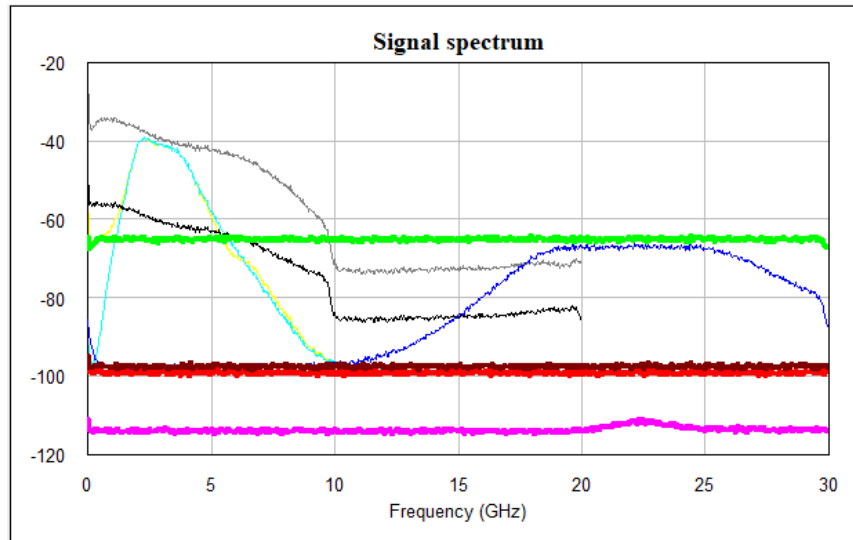
FIGURE 4.22. Spectrum of the signal as it passes through each component of the diagram. the Y axis indicates the power in dBm. Note the colors that differentiate each of the elements and their bandwidths, which indicates the veracity of the input signal. These colors are the same as for figure (4.21), except that in this graph, due to the sampling value, a wider frequency range is shown on the X axis and therefore the lines are shown in the entire range, but It is emphasized that it should be observed that each of them denotes its bandwidth in the frequency range that corresponds to it, as well as the peak of the pink line that is shown only at 22 GHz.

power or power spectral density (power/Hz). Offering for this case, where the BPF IF from 2 to 4 GHz and a PWV of 2.8 mm are taken into account, a power adjustment result of the 22 GHz radiometer is -24.057 dBm.

This value shows the output power of the analog stage. An important parameter to consider is the digital part, which indicates that combining an LNA with a gain of approximately 24 dB before the ADC reaches the value required by the digital card of 0 dBm is necessary.

Another critical parameter in the analog-digital interface is the gain budget, for which the scheme for the BPF FI from 2 to 4 GHz and the PWV value of 2.8 mm was used again. Carrying out a cumulative sweep simulation to evaluate the parameters S_{21}, the result of the gain budget is obtained, shown in figure (4.23), whose result is 55.73 dB.

4.8   Selection of commercial components

According to the desired characteristics in the concept and design of the CePIA 22 GHz tuned radiometer, and based on the requested requirements, a search is done for commercial analog components that will eventually form part of the instrument.

The list of the laboratory's different companies and suppliers is analyzed so that they adapt to a commercial search in the requested frequency ranges, which in the first instance, is the most critical requirement.
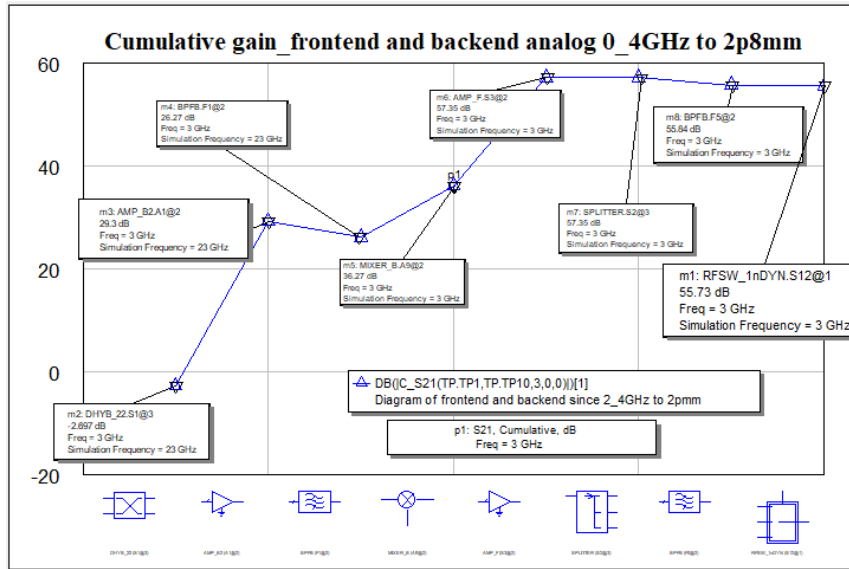
FIGURE 4.23. Result of the gain budget. Note that show the cumulative contribution of all components. The result is: 55.73 dB.

An exhaustive search for analog frontend and backend components is initiated, and four (4) to six (6) prospects of each element are chosen by looking at their technical data sheets provided by the company, following the selection criteria that meet the width of band, low noise, connection model to the same cables for all, high gains, low return losses, phase and amplitude in the cases that are relevant.

A catalog of approximately 70 components is established where their main characteristics, model, companies, quantity, delivery, and other relevant parameters are described. This catalog goes through a selection process at the convenience of choosing the elements that can successfully meet the requirements set forth above, considering several factors, among them the simulations of section (4.5).

After choosing the best combination of features, cost, delivery, size, and connection, a list of the final components to buy is generated. It is essential to make three (3) quotes for each component and take the necessary precautions at the time of purchase. The vast majority of the elements already definitive and will be acquired for the instrument are in table (4.3).

It is expected to continue analyzing the components once they have been obtained using a VNA (vector network analyzer), an instrument with which numerous tests can be carried out to check the correct operation and performance of the elements.

TABLE 4.3. List of components chosen for purchase that will be part of CePIA's 22 GHz radiometer.

Element	Company	Model	Description	Cost (USD)
Horn	Eravant	SAR-2013-42-S2	Pyramidal, 18.0-26.5GHz, Gain: 20dB, Return loss: 23dB, Connector WR-42	760
Coaxial adapter	Eravant	SWC-42KF-E1	$18 - 26.5$ GHz, Insertion loss 0.3 db, Return loss 20dB, Puerto de guía de onda WR-42, coaxial 2.92mm	320
Hybrid 180° (2)	Tuneful RF	TFHC-180K2028	20-28 GHz, insertion loss 2dB, amplitude unbalance +/-0.7dB, phase unbalance +/-10°, insertion loss 2dB, connetor 2.92 female	675
LNA RF (2)	Tuneful RF	TFMA-ULNM1826.530	18-26.5 GHz, Gain 32dB, NF 1dB, P1dB 15dBm, SMA Female	1590
BPF RF (2)	Marki	FB-2480	Frequency range 21.1-28.5 GHz, insertion loss 3dB, passband return loss 15dB, connector 2.92mm female	327
Mixer (2)	Tuneful RF	TFDC-2030-10-DC6	Frecuency range RF 20-30GHz, Frecuency range LO 10-15GHz, Frecuency range IF DC-6GHz, Conversion gain 10dB, Lo power 0dB, NF 4dB, Female	2490
Divider x2	Clear Microwave	D218/D218T	DC-18 GHz, insertion loss 1dB, amplitude balance +/-0.10dB, phase amplitude +/-1.5°, SMA Female	172
Phase shifter (2)	Tuneful RF	TFPS-360VC0812	8-12 GHz, insertion loss 8dB, phase shift 360°	1450
LNA IF (2)	MiniCircuits	ZX60-83LN-S+	0.5-8GHz, NF 1.4dB, Gain 22.1dB	164.45
LPF IF (2) (DC-2 GHz)	MiniCircuit	ZX60-83LN-S+	DC-2000 MHz, insertion loss 3.8dB, 2.92mm-F	164.45
BPF IF (2) (2-4 GHz)	Fairview Microwave	FMFL1013	2-4 GHz, insertion loss 2dB, impedance 50ohm, SMA Female	470
BPF IF (2) (4-6 GHz)	Qotana	DBBF1004200770A	Frequency range 4.2-7.7 GHz, insertion loss 0.7dB, SMA Female	175
Divider x3 (2)	Clear Microwave	D313 / D313T	DC-13 GHz, amplitude balance 0.12dB, phase balance 12°, SMA Female, insertion loss D313 0.9dB, insertion loss D313T 0.35dB	230

Chapter 5

Optimal Estimation Model

5.1 The forward model

The problem that will be examined here is as follows: given a measurement or series of measurements of thermal radiation emitted by an atmosphere, the intensity and spectral distribution of which depend on the state of the atmosphere in a known way, deduce the best estimate of the state of the atmosphere. There are two distinct aspects to this problem which are not always clearly separated; they may be described as the 'inverse' problem and the 'estimation' problem. The inverse problem is the matter of inverting a known equation which expresses radiation as a function of the atmospheric state, so as to express atmospheric state in terms of radiation. This is usually an 'ill-posed' problem; i.e., it has no mathematically unique solution. We therefore have an estimation problem, that is, to find the appropriate criteria which determine the best solution from all the possible ones which are consistent with the observations Rodgers (1976).

There exists a direct relation between the power radiated by an object and the radiometric brightness temperature T_b of the scene under consideration Karmakar (2019). According to equation (1.14), all total power spectra where measured voltages are converted to brightness temperature can be converted to a water vapor volume mix ratio (VMR) profile according to the OEM Optimum Estimation Method Rodgers (2000). But first starting with a linearized version of the radiative transfer equation for which the inverse problem is trivial, it is possible to address estimation issues.

The result for the radiance $L(\nu)$ emerging vertically at the top of the atmosphere at wavenumber ν is

$$L(\nu) = \int_{\infty}^{0} B[\nu, T(z)] \frac{d\tau(\nu, z)}{dz} dz \qquad (5.1)$$

where $B[\nu, T(z)]$ is the Planck radiance at temperature T at height z, and $\tau(\nu, z)$ is the atmospheric transmittance from height z to the measuring instrument above the atmosphere. For simplicity we assume that the absorption of the whole atmosphere is so great that the transmittance from the surface to the instrument is zero, and emission from the surface can be ignored.

Consider making a set of measurements of radiance, $L(v_i), i = 1...m$, at a set of m closely spaced wavenumbers v_i, so that de frequency dependence of the Planck function can be ignored, but that of the transmittance varies considerably:

$$L_i = L(v_i) = \int_\infty^0 B(\bar{v}, T(z)) K_i(z) dz \qquad (5.2)$$

where v is some representative wavenumber and $K_i(z) = d\tau(v_i, z)/dz$ is a function of only z and i. The equation is now linear in $B(\bar{v}, T(z))$, which we may take to be the unknown. If $B(\bar{v}, T(z))$ can be found, then $T(z)$ follows immediately, as the Planck function can be inverted algebraically. The radiance is thus a weighted mean of the Planck function profile, with $K_i(z)$ as the *weighting function*. It is a true mean, because the assumption of zero transmittance from the surface to space ensures that $\int_\infty^0 K_i(z) dz = 1$. Because of this, any quantity that takes the part of $K_i(z)$ in any inverse problem tends to be called the weighting function in the atmospheric literature, regardless of whether it is normalised.

Solving equiation (5.2) is clearly going to cause some difficulties, not least because it is underconstrained, or ill-posed, as there are only a finite number of measurements, and the unknown is a continuous function. The obvious approach is to express the unknown as a function of a finite number of parameters, such as a polynomial or a sum of sines and cosines. The general linear form, of which these are but two examples can be written

$$B(\bar{v}, T(z)) = \sum_m^{j=1} \omega_j W_j(z) \qquad (5.3)$$

where ω_j is a set of coefficients to be found, and $W_j(z)$ is a set of functions, such as z^{j-1} or $sin(2\pi j z/Z)$ and $cos(2\pi j z/Z)$ for a finite height range $(0, Z)$, in terms of which the profile is to be represent. Substituting (5.3) into (5.2) gives

$$L_i = L(v_i) = \sum_m^{j=1} \omega_j \int_\infty^0 W_j(z) K_i(z) dz = \sum_m^{j=1} C_{ij} \omega_j \qquad (5.4)$$

thus defining the square matrix C whose elements $C_{ij} = \int_\infty^0 W_j(z) K_i(z) dz$ can easily be calculated (the spectral shape of the measured broadened line). We now have a set of m equations for m unknowns, which can in principle be solved exactly. Unfortunately this type of solution is ill-conditioned in many practical situations, as will be illustrated. This means that any experimental error in the measurements can be greatly amplified. Solve equation (5.4) by inverting the matrix, so that the vector of coefficients $C^{-1}\mathbf{1}$, where $\mathbf{1}$ is the vector of radiances, and substitute the result back in equation (5.3):

$$B(\bar{v}, T(z)) = \sum_{i,j} W_j C^{ji}_{-1} L_i = \sum_i G_i(z) L_i \qquad (5.5)$$

where C^{ji}_{-1} is the *jith* component of the inverse matrix C^1. This equation also defines the set of functions $G_i(z)L_i$ is the contribution to the solution profile due to the measured radiance L_i. This solution gives back exactly the measured radiances when inserted in the measurement equation (5.2), and can therefore be termed exact. If there is an error ϵ_i in the measurement of L_i, then there will obviously be a corresponding error $G_i(z)\epsilon_i$ in the profile. Thus the size of the functions $G_i(z)$ gives an indication of the ill-conditioning of the solution method Rodgers (2000).

The spectral shape of the measured broadened line can be related to the vertical distribution of water vapor in the atmosphere Straub et al. (2010), and the calculation of the water vapor mixing ratio profiles is based on the variation of the shape of the line with the altitude Nedoluha et al. (1995). Therefore, the recovery of water vapor profiles as a function of altitude (or pressure) depends on the sensitivity of the observed spectrum to pressure broadening Nedoluha et al. (1997).

There are components of the atmospheric profile which make no contribution to the quantities measured, so that in principle the size of these components could be infinite. The purpose Optimal Estimation Method is to have of a priori constraints is to set bounds on them Rodgers (1976). This method needs sufficient a priori information using radiosonde observation, this in turn depends on historical background of the location and time of the year Karmakar (2019).

The extended pressure spectrum (y) is a function of the profile of the species to be recovered (x), the parameter b takes into account the remaining information on the atmospheric state, which could influence the measured spectrum, and is the measurement noise, and F represents the mapping or radiative transfer operator, also called the direct model operator, it follows,

$$y = F(x, b) + \varepsilon \tag{5.6}$$

It has then, a linearized radiative transfer equation is obtained employing the Taylor series expansion around an initial guess atmospheric state, x_a, (also referred to as the a priori state vector), which is the best beforehand estimator of the true solution. Neglecting the higher order terms in the Taylor series expansion, the following linear relation between measured radiances and atmospheric parameters to be retrieved is obtained Rozanov et al. (2011):

$$y = F(x_a) + \frac{\partial F(x)}{\partial x}|_{x=x_a} \times (x - x_a) + \varepsilon \tag{5.7}$$

Neglecting all errors, the linearized inverse problem is written as

$$y = F(x) + \epsilon = Kx + \epsilon \tag{5.8}$$

or

$$y = F(x_a) + A(x - x_a) \tag{5.9}$$

where **A** is the Jacobian matrix, also known as the weighting function matrix, which is a measure of the sensitivity of recovery to disturbances at a given altitude.

x_a is the state vector, which assumes the a priori parameters of a site, and can vary with respect to the annual season.

A qualitative description of the number of independent pieces of information in a measurement as the number of singular values of K which $\widetilde{K}$ are greater than about unity, how many of the degrees of freedom of a measurement are related to signal, and how many are related to noise. Consider the general case of measuring a vector y with m degrees of freedom. The most probable state in the Gaussian linear case is the one which minimises,

$$\chi^2 = (x - x_a)^T S^a_{-1}(x - x_a) + \epsilon^T S^\epsilon_{-1}\epsilon \tag{5.10}$$

where $\epsilon = y - Kx$, and the convariance matrix S_a qualitatively indicates the accuracy of the recovered atmospheric parameters, such as the concentration in each layer and the correlation of errors between different layers.

The best estimate $\widehat{x}$ of the atmospheric state, assuming that the errors obey linear Gaussian statistics, which is a valid assumption in our case since the atmosphere is optically thin at 22GHz, is given by Rodgers (1976, 2000); Straub et al. (2011):

$$\widehat{x} = x_a + \left(K_x^T S_y^{-1} K_x + S_a^{-1}\right)^{-1} K_x^T S_y^{-1}(y - K_x x_a) \tag{5.11}$$

$$\widehat{x} = x_a + D_y(y - K_x x_a) \tag{5.12}$$

$$\widehat{x} = x_a + A(x - x_a) \tag{5.13}$$

where y is the measured spectrum, x true atmospheric profile, x_a a priori profile, $\widehat{x}$ retrieved profile, S_y error covariance matrix of y (measurement noise), S_a error covariance matrix of x_a, K_x weighting function matrix, describes sensitivity of y variations in x, D_y retrieval gain matrix, represents sensitivity of $\widehat{x}$ to y and, **A** averaging kernel matrix, $D_y K_x$ characterizes the response of the retrieved VMR profile ($\widehat{x}$) to a perturbation in the "true" profile $\widehat{x}_x$ and explains the sensitivity and limited vertical resolution of a recovery Rodgers (2000).

The retrieved profile thus consists of an a priori estimate to which we add a fraction of the H_2O profile corresponding to $(y - F(x_a))$. **A** approaches zero at low pressures (high altitudes) where the absolute amount of H_2O becomes very small and where the line width becomes smaller than the spectral resolution of the instrument, also, **A** decreases at high pressures (low altitudes), where the line width becomes larger than the bandwidth of the instrument due to the pressure broadening Haefele et al. (2009).

Retaking equation (5.10), the minimum is at

$$\widehat{x} - x = G(y - Kx_a) = G\left[K(x - x_a) + \epsilon\right] \tag{5.14}$$

where the equivalent of the contribution function of equation (5.5) is now a matrix G, given by

$$G = (K^T S^{\epsilon}_{-1} K + S^a_{-1})^{-1} K^T S^{\epsilon}_{-1} = S_a K^T (K S_a K^T + S_{\epsilon})^{-1} \tag{5.15}$$

This matrix is a *contribution function matrix*. At the minimum the expected value of χ^2 ls equal to the number of degrees of freedom, or the number of measurements, m; and, to calculate the recovered state vector x_{ret} or $\widehat{x}$, and its covariance matrix S_{ret} or $\widehat{S}$ are,

$$\widehat{x} = x_a + G((y - y_0) - K(x_a - x_0)) \tag{5.16}$$

$$\widehat{S} = (K^T (S^{\epsilon}_{-1} K) + S^a_{-1})^{-1} \tag{5.17}$$

On the other hand, F(x) is not linear in the troposphere, an iterative search for the solution is performed using the Levenberg-Marquardt approach Levenberg (1944); Marquardt (1963). The $(i + 1) - th$ iterative step, this approach results in the following solution:

$$x_{i+1} = x_i + (K_i^T S_e^{-1} K_i + S_x^{-1} + \gamma D_x^{-1})^{-1} \left[K_i^T S_e^{-1} (y - F(x_{i,b})) - S_x^{-1} (x_i - x_a) \right] \tag{5.18}$$

where x_i is the state vector at iteration i, x_a the a priori state vector, y the measured spectrum, $F(x_i, b)$ the spectrum calculated with the forward model, S_e the error covariance matrix, S_x the a priori covariance matrix, D_x the diagonal matrix of S_x, $K_i = \frac{\partial F(x_i,b)}{\partial x_i}$ the weighting function matrix evaluated at x_i and γ is a trade-off parameter. The iteration is initiated by setting x_a as the state vector and continued until the cost-function (γ^2), derived from Bayes' probability theorem is minimized Bleisch et al. (2011):

$$\chi^2 = [y - F(x_i, b)]^T S_e^{-1} [y - F(x_i, b)] + [x_i - x_a]^T S_x^{-1} [x_i - x_a] \tag{5.19}$$

At each step, γ is decreased if $\chi^2(x_{i+1}) < \chi^2(x_i)$. Otherwise, x_{i+1} is rejected, and the iteration is retried with an increased γ. To save computing time, the number of iterations is limited to 10 Bleisch et al. (2011).

Furthermore, the main components of the random error of a retrieval method are the observation error, caused by measurement noise and uncertainty, and the smoothing error, caused by the vertical smoothing of the retrieval method. The observation error and smoothing error covariances can be estimated as follows Rodgers (2000):

$$S_{obs} = D_y S_e D_y^T \tag{5.20}$$

$$S_{smo} = (A - I)S_x(A - I)^T \qquad (5.21)$$

where **I** is the identity matrix. For more detailed information on the forward model, review E).

5.2   Application of a vertical water vapor characterization model

To retrieve PWV values using spectral measurements of the rotational water line at 22 GHz, brightness temperature data at this frequency from the NASA Merra2 satellite (Modern-Age Retrospective Analysis for Research and Applications, version 2) are considered. That generates atmospheric values in near real-time and distributes them to a broad community of users. With it, it is possible to create AM configuration files and simulate spectra for the 22 GHz radiometer, with the following characteristics: lowest frequency: 20 GHz, highest frequency: 26 GHz, bandwidth channel: 62 kHz, adding noise Gaussian to recreate a more realistic situation.

These MERRA2 data were taken in the decade between 2010 and 2020; 10 recoveries were made for each month of the year every year, an average was made for each month and then an average for each year, and finally, an average for the entire decade, and they are the data that we find in the figure (F.6), see E.

These AM configuration files imply several command-line parameters to set the frequency grid range and resolution, the zenith angle of observation, the surface temperature, and a scale factor applied to the tropospheric water vapor profile. This scale factor is used to model variations in the total precipitable water vapor over the observatory site to approximate the natural variation of the H2O mixing ratio profile by scaling a profile of fixed form and is implemented using a Nscale statement. For example, the statement "Nscale h2o 0.9" would scale the entire H2O profile defined in the model by a factor 0.9. In contrast, the statement "Nscale troposphere h2o 0.9", would scale the H2O column density only on those layers tagged with the layer tag troposphere Paine (2012).

A simple configuration file to model this situation defines the frequency range and resolution, the background temperature, and at least a layer containing a single absorbing species, H_2O. These are the output variable(s) with the units that are needed by specifying in the header of the file (see Chapter 1 and A); an example of the complete text of the file, can be seen in figure (5.1). A more complete example of a file that has parameters including MERRA2 data is shown in figure (5.2).

Through the OEM, the AM and the development of some python scripts, it is possible to perform recoveries for water vapor. Here are some examples and the step by step carried out to demonstrate a first attempt at possible codes that will be established

```
f 0 GHz  2500 GHz  50 MHz    # frequency grid for computation
T0 77 K                      # background temperature

Nscale troposphere h2o %11

layer                        # introduces a layer
P 1013.25 mbar               # layer pressure
T 20 C                       # layer temperature
h 1 m                        # layer thickness
column h2o vmr 0.012         # adds a column of h2o to this layer
```

FIGURE 5.1. A laboratory propagation path. Source: Paine (2012).

```
f %1 %2   %3 %4   %5 %6
output f GHz   tau   Tb K
za %7 %8
tol 1e-4

Nscale troposphere h2o %11

T0 2.7 K

layer mesosphere
Pbase 0.1 mbar
Tbase 222.3 K
lineshape Voigt-Kielkopf
column dry_air vmr
column h2o vmr 6.46e-06
column o3 vmr 1.77e-06

layer mesosphere
Pbase 0.3 mbar
Tbase 243.3 K
lineshape Voigt-Kielkopf
column dry_air vmr
column h2o vmr 6.60e-06
column o3 vmr 1.65e-06
```

FIGURE 5.2. An example about command-line parameters in AM file, see the different parameters. Source: Paine (2012).

when the 22 GHz radiometer is in operation.

It is possible to perform recoveries for water vapor through the OEM, the AM, and the development of some Python scripts. Here are some examples and the step-by-step carried out to demonstrate a first attempt at possible codes that will be established when the 22 GHz radiometer is in operation.

The basic idea behind the OEM is that a retrieval based on simply minimizing the sum of squared residuals relative to a forward model is generally unstable. Still, the retrieval can be stabilized by adding contribution from the squared residuals relative to a statistical prior, such as a climatological average and its associated covariance to the overall function to be minimized. The critical point is that if the forward model is linear, the OEM solution can be found with matrix algebra. The linearized model consists of the forward computation at the reference point and its Jacobian matrix containing the spectral derivatives concerning all the model parameters to be retrieved, iterates as many times as necessary, re-linearizing about a retrieved solution and retrieving again.
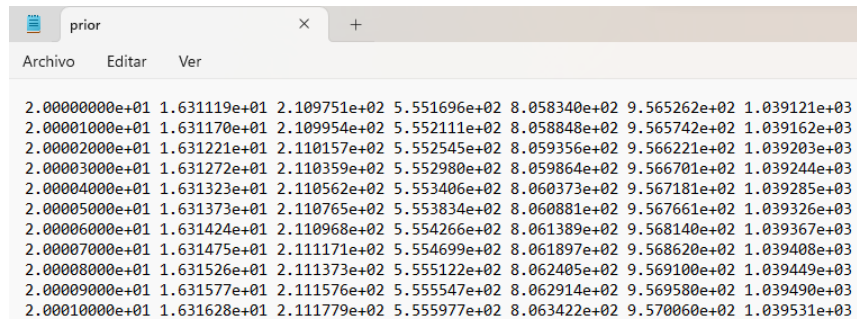
That is why using the OEM best estimation method and having the AM software

available, it is possible to carry out an exercise to calculate the recoveries of water vapor profiles at a vertical level in a simple 5-layer model first. It is assumed that the temperature profile is fixed, that the only meteorological variables to be retrieved are the H2O mixing ratios in the five model layers, and that the previous (a priori) statistical state and the point about which the model is linearized model are the same.

The above state is given by the AM configuration file "prior.amc" (see F figure F.2). Where the water mix ratios correspond to approximately 50% RH (relative humidity) in each layer. To keep things simple, it is assumed that these mixing ratios are not correlated at all, so the above inverse covariance matrix for the mixing ratios is a diagonal matrix whose diagonal elements are the reciprocals of the variances (standard deviations in the square) of the corresponding mixing proportions.

Also, assume that the standard deviations are 25% of RH (i.e., the likely range of RH is 25% to 75% with a mean of 50%, so that the standard deviation is half the mean value). Thus, in "prior.amc" you will see that, for example, the mixing ratio of water in the top layer is 9.0^{-5}, and that the corresponding diagonal element in the inverse covariance matrix is $1/(4.5^{-5})^2 = 4.9^{-8}$, etc. The AM prior.amc file computes the forward model in the reference state (y_0 in retrieval.py) and its Jacobian matrix (K in retrieval.py).

When running the prior.amc file in a terminal, the output is prior.out file in which we have the columns for the frequency, the T_{rj}, and the Jacobians of the layers, figure (5.3).

```
📄  prior                              ×    +

Archivo    Editar    Ver

2.00000000e+01 1.631119e+01 2.109751e+02 5.551696e+02 8.058340e+02 9.565262e+02 1.039121e+03
2.00001000e+01 1.631170e+01 2.109954e+02 5.552111e+02 8.058848e+02 9.565742e+02 1.039162e+03
2.00002000e+01 1.631221e+01 2.110157e+02 5.552545e+02 8.059356e+02 9.566221e+02 1.039203e+03
2.00003000e+01 1.631272e+01 2.110359e+02 5.552980e+02 8.059864e+02 9.566701e+02 1.039244e+03
2.00004000e+01 1.631323e+01 2.110562e+02 5.553406e+02 8.060373e+02 9.567181e+02 1.039285e+03
2.00005000e+01 1.631373e+01 2.110765e+02 5.553834e+02 8.060881e+02 9.567661e+02 1.039326e+03
2.00006000e+01 1.631424e+01 2.110968e+02 5.554266e+02 8.061389e+02 9.568140e+02 1.039367e+03
2.00007000e+01 1.631475e+01 2.111171e+02 5.554699e+02 8.061897e+02 9.568620e+02 1.039408e+03
2.00008000e+01 1.631526e+01 2.111373e+02 5.555122e+02 8.062405e+02 9.569100e+02 1.039449e+03
2.00009000e+01 1.631577e+01 2.111576e+02 5.555547e+02 8.062914e+02 9.569580e+02 1.039490e+03
2.00010000e+01 1.631628e+01 2.111779e+02 5.555977e+02 8.063422e+02 9.570060e+02 1.039531e+03
```

FIGURE 5.3. Output of the necessary parameters from prior.amc including the Jacobians of the 5 layers. Source: Harvard University-Scott Paine.

Then a simulated measurement is needed. The "simulated.amc" file (see F, figure F.3) has a setup similar to a drier state with all water mix ratios around 20% lower (and as shown indicated above, the same temperatures), plus adds Gaussian noise. I assumed a receiver noise temperature of 300 K and an SNR per channel of 250. The input frequency range between 20 and 26 GHz is considered, with a spectral resolution of 0.5 MHz, and the output is obtained Rayleigh-Jeans temperature as a function of frequency. All this using the script "make-simulated-spectrum.py" (see F, figure F.1), so it is possible to get, in the first instance, the spectrum of the simulated measurement, which also contains an associated noise temperature, whose result is,
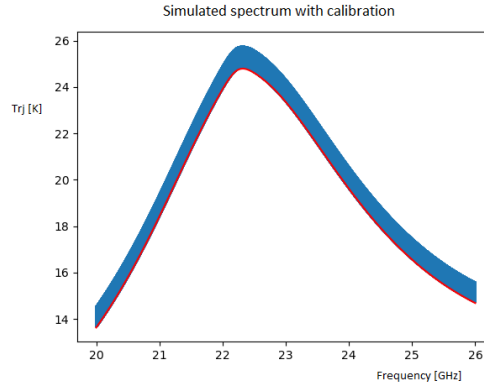
FIGURE 5.4. Rayleigh-Jeans temperature plot (T_{rj}) [K] vs. frequency [GHz] of a simulated spectrum for a particular atmospheric state, which has noise temperature to show its calibration.

Finally, "retrieval.py", a Python script (see F, figure F.4), runs the OEM retrieval, generating the file "retrieval.out". If when comparing the retrieved mixing ratios with the ones in "simulated.amc", t is possible to see they're reasonably close. Another interesting output is the number of degrees of freedom for signal, which is about 4, meaning that about 4 independent values were retrievable. This output (file "retrieval.out"), where the H_2O data, the degrees of freedom, covariance matrix and kernel are shown, can be seen in figure (5.5).

Taking the AM file "simulated.amc", another AM file called "retrieved.amc" is made, and the data of the recovery of the water vapor (H_2O in vmrs) figure (5.5); they are introduced or better said, they are replaced in the "column h2o hydrostatic", and in this way, we can evaluate the spectrum recovered concerning the a priori (prior) and the simulated (simulated). This "retrieved.amc" file can be found at F, figure F.5.

With the water vapor data from these AM files, it is possible to compare all their spectra. First, a table is made with the values of H_2O in vmrs, taking into account that the Rayleigh-Jeans temperature is used, the values of the prior, simulated, and recovered water vapor, together with the statistical error of recovery, table (5.1); to later graph them, figure (5.6).

TABLE 5.1. Water vapor values for each of the spectra evaluated.

Layer	Pressure (mbar)	Prior	Simulated	Retrieval model	Statistical uncertainties
1	200	9.0×10^{-5}	7.0×10^{-5}	6.079×10^{-5}	6.578×10^{-6}
2	400	1.7×10^{-4}	1.0×10^{-4}	1.413×10^{-4}	6.723×10^{-5}
3	600	1.1×10^{-3}	8.0×10^{-4}	7.349×10^{-4}	2.766×10^{-4}
4	800	3.1×10^{-3}	2.0×10^{-3}	1.859×10^{-3}	4.482×10^{-4}
5	1000	6.3×10^{-3}	5.0×10^{-3}	5.165×10^{-3}	2.324×10^{-4}

5.3 Case: Cerro Ventarrones

The case presented in the previous section are spectra evaluated in collaboration with Scott Paine, the author of the AM software, therefore his contribution is mainly

```
Retrieved H2O vmrs:
[[6.079e-05]
 [1.413e-04]
 [7.349e-04]
 [1.859e-03]
 [5.165e-03]]

Statistical uncertainties:
[[6.578e-06]
 [6.723e-05]
 [2.766e-04]
 [4.482e-04]
 [2.324e-04]]

Full covariance matrix for retrieved vmrs:
[[ 4.328e-11 -2.724e-10  3.614e-10 -1.937e-11 -1.219e-10]
 [-2.724e-10  4.520e-09 -1.571e-08  2.016e-08 -8.657e-09]
 [ 3.614e-10 -1.571e-08  7.652e-08 -1.189e-07  5.794e-08]
 [-1.937e-11  2.016e-08 -1.189e-07  2.009e-07 -1.027e-07]
 [-1.219e-10 -8.657e-09  5.794e-08 -1.027e-07  5.400e-08]]

Degrees of freedom for signal:
4.004

Full averaging kernel matrix:
[[ 9.788e-01  3.814e-02 -1.193e-03  8.137e-06  1.219e-05]
 [ 1.335e-01  3.672e-01  5.185e-02 -8.465e-03  8.657e-04]
 [-1.771e-01  2.200e+00  7.475e-01  4.994e-02 -5.794e-03]
 [ 9.493e-03 -2.822e+00  3.924e-01  9.156e-01  1.027e-02]
 [ 5.971e-02  1.212e+00 -1.912e-01  4.315e-02  9.946e-01]]
```

FIGURE 5.5. File "retrieval.out", with the parameters indicating a recovery of atmospheric water vapor for a 5-layer model.

in Cambridge-USA. But our interest is to be able to evaluate the PWV in Cerro Ventarrones, for which we have data from a decade of the site in question, these data were taken by MERRA2 and are averaged for different pressures.

Taking into account the previous steps (section 5.2) but with the exclusive a priori for Cerro Ventarrones (see F, figure F.6), it was possible to establish simulated spectra with Gaussian noise and real site recoveries for three models, one with 5 layers, another with 15 layers and another for 30 layers. In each of them, the recoveries above (high) and below (low) the a priori are evaluated, that is, wet and dry spectra, and their percentage errors are estimated.

In order to have the superposition of the a priori, simulated and recovered spectra in this particular case for Cerro Ventarrones, representative tables of the water vapor values in each case are made, firstly for the 5-layer model, both for the high and for the low, tables (5.2) and (5.3) and then if the graphs of the spectra, figures (5.7) and (5.8).

The simulated spectrum is obtained by multiplying the water vapor values of the
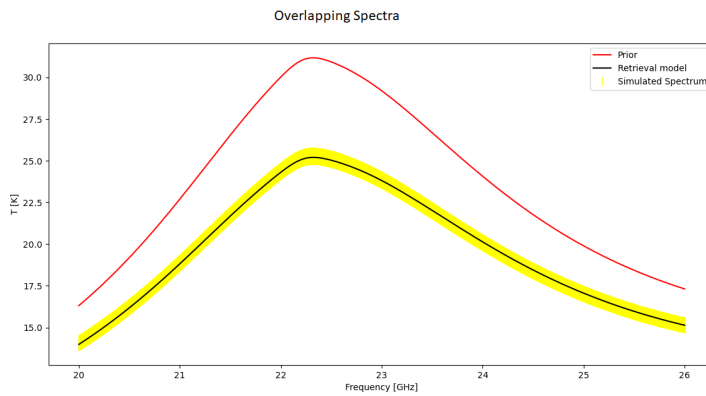
FIGURE 5.6. Representation of the three (3) spectra of water vapor studied for an ideal atmosphere with 5 layers. Note that for this case, the prior contains much more water than the retrieved model. It is also notable to observe the simulated spectrum and its associated noise. Corresponds table (5.1)
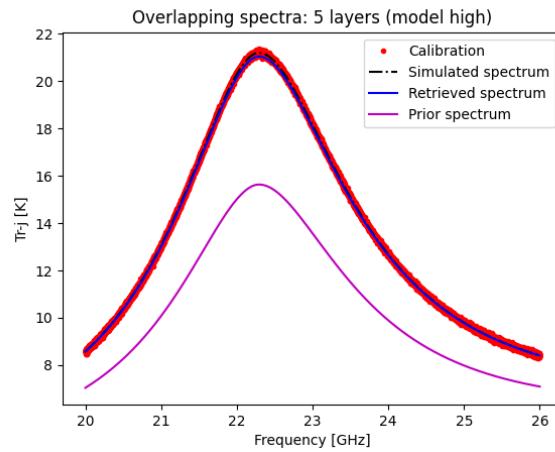
FIGURE 5.7. Representation of the three (3) spectra of water vapor studied for a model with 5 layers high (with a priori dry). The simulated spectrum with its associated noise, and the retrieved. Corresponds to the table 5.2.
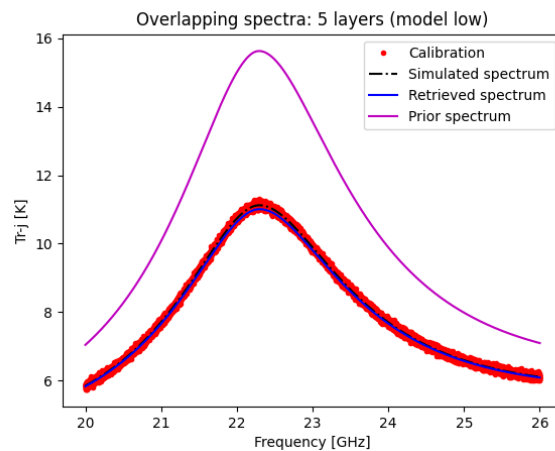
FIGURE 5.8. Representation of the three (3) spectra of water vapor studied for a model with 5 layers. Note that for this case, the prior contains much more water than the retrieved model. It is also notable to observe the simulated spectrum and its associated noise, and the retrieved. Corresponds to the table 5.3.

TABLE 5.2. Water vapor values for each of the spectra evaluated (priori, simulated and retrieved) for the 5-layer high model.

Layer	Pressure (mbar)	Prior	Simulated	Retrieved	Statistical uncertainties
1	100	5.1×10^{-6}	3.1×10^{-6}	9.5×10^{-6}	1.1×10^{-6}
2	200	6.0×10^{-5}	3.6×10^{-5}	4.2×10^{-5}	1.0×10^{-5}
3	400	4.9×10^{-4}	2.9×10^{-4}	8.6×10^{-4}	1.7×10^{-5}
4	600	1.6×10^{-3}	9.6×10^{-4}	2.0×10^{-3}	3.1×10^{-5}
5	700	2.7×10^{-3}	1.6×10^{-3}	4.7×10^{-3}	3.7×10^{-5}

TABLE 5.3. Water vapor values for each of the spectra evaluated (priori, simulated and retrieved) for the 5-layer low model.

Layer	Pressure (mbar)	Prior	Simulated	Retrieved	Statistical uncertainties
1	100	5.1×10^{-6}	3.1×10^{-6}	2.6×10^{-6}	1.0×10^{-6}
2	200	6.0×10^{-5}	3.6×10^{-5}	2.7×10^{-5}	9.9×10^{-6}
3	400	4.9×10^{-4}	2.9×10^{-4}	3.4×10^{-4}	1.7×10^{-5}
4	600	1.6×10^{-3}	9.6×10^{-4}	7.7×10^{-4}	2.6×10^{-5}
5	700	2.7×10^{-3}	1.6×10^{-3}	1.9×10^{-3}	3.6×10^{-5}

prior with the scale factor Nscale, which in the case of the 5-layer model is 0.6. Remember what this scale factor is used to model variations in the total precipitable water vapor over the observatory site in a manner which approximates the natural variation of the H_2O mixing ratio profile – water vapor and its fluctuations are largely confined below the "cold trap" at the tropopause Paine (2012)

The PWV results retrieved for the site in each case are: **high model: 6.64mm** with an error of 0.30% and **low model: 2.64mm** with an error of 0.75%; with respect to the real value.

As well as for the 5-layer model in high and low, it was also possible to make the necessary files and simulations to obtain the necessary values of tables (5.4) and (5.5), where the priori water vapor data is represented. , of the simulated and recovered spectrum for the 15-layer model in high and low, their graphs can be seen in figures (5.9) and (5.10).

The Nscale value for 15 layers depends on the high model which is 1.5 and the low is 0.5, only to the tropospheric layers.

The PWV results retrieved for the site in each case for 15 layers are: **high model: 5.06mm** with an error of 0.64% and **low model: 1.69mm** with an error of 0.1%; with respect to the real value.

Finally, for the model of 30 layers in high and low, the appropriate values of the priori water vapor, the simulated spectrum and the recovered were obtained, which are reflected in tables (5.6) and (5.7), and their graphs. they are observed in figures (5.11) and (5.12).
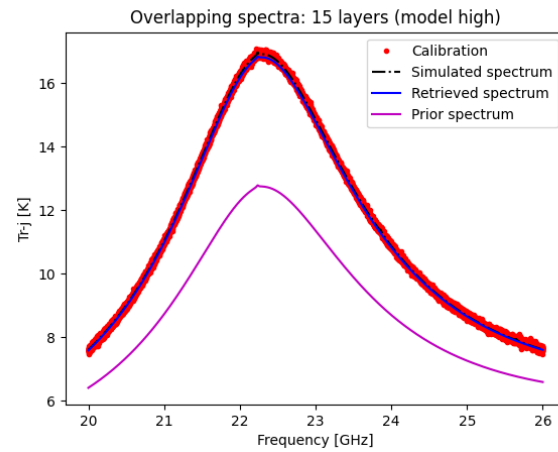
FIGURE 5.9. Representation of the three (3) spectra of water vapor studied for a model with 15 layers high (with a priori dry). The simulated spectrum and its associated noise, and the retrieved. Corresponds to the table 5.4.
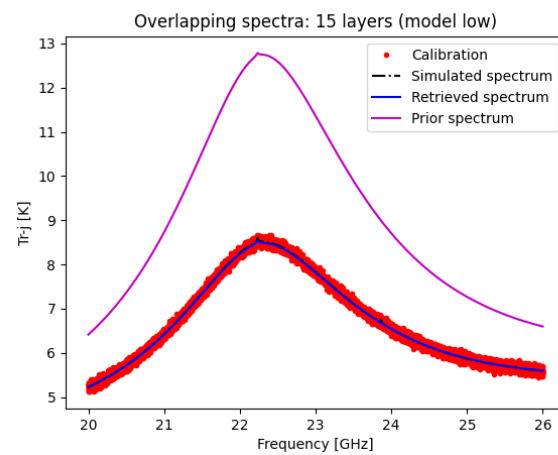
FIGURE 5.10. Representation of the three (3) spectra of water vapor studied for a model with 15 layers. Note that for this case, the prior contains much more water than the retrieved model. It is also notable to observe the simulated spectrum and its associated noise, and the retrieved. Corresponds to the table 5.5.

TABLE 5.4. Water vapor values for each of the spectra evaluated (priori, simulated and retrieved) for the 15-layer high model.

Layer	Pressure (mbar)	Prior	Simulated	Retrieved	Statistical uncertainties
1	10	4.9×10^{-6}	4.9×10^{-6}	4.6×10^{-6}	9.6×10^{-7}
2	50	4.4×10^{-6}	4.4×10^{-6}	4.7×10^{-6}	1.2×10^{-6}
3	100	5.1×10^{-6}	7.7×10^{-6}	5.7×10^{-6}	2.4×10^{-6}
4	150	1.5×10^{-5}	2.3×10^{-5}	1.8×10^{-5}	7.0×10^{-6}
5	200	6.0×10^{-5}	9.0×10^{-5}	8.5×10^{-5}	2.5×10^{-5}
6	250	1.5×10^{-4}	2.2×10^{-4}	2.4×10^{-4}	5.8×10^{-5}
7	300	2.4×10^{-4}	3.7×10^{-4}	3.9×10^{-4}	1.0×10^{-4}
8	350	3.5×10^{-4}	5.2×10^{-4}	5.4×10^{-4}	1.5×10^{-4}
9	400	4.9×10^{-4}	7.5×10^{-4}	7.3×10^{-4}	2.2×10^{-4}
10	450	7.1×10^{-4}	1.1×10^{-3}	1.0×10^{-3}	3.1×10^{-4}
11	500	9.9×10^{-4}	1.5×10^{-3}	1.4×10^{-3}	4.3×10^{-4}
12	550	1.3×10^{-3}	1.9×10^{-3}	1.8×10^{-3}	5.4×10^{-4}
13	600	1.6×10^{-3}	2.4×10^{-3}	2.2×10^{-3}	6.5×10^{-4}
14	650	2.1×10^{-3}	3.1×10^{-3}	2.9×10^{-3}	8.5×10^{-4}
15	700	2.7×10^{-3}	4.1×10^{-3}	4.6×10^{-3}	5.1×10^{-4}
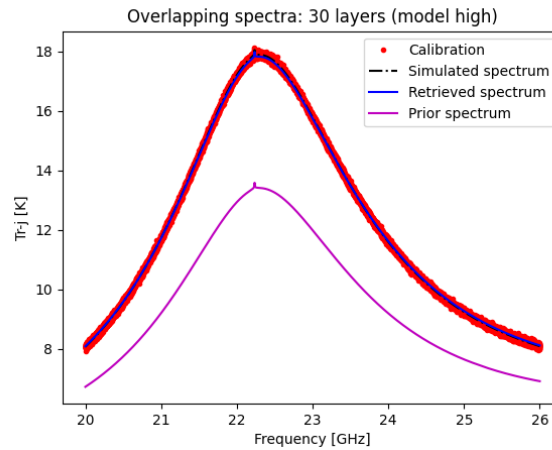
FIGURE 5.11. Representation of the three (3) spectra of water vapor studied for a model with 30 layers high (with a priori dry). The simulated spectrum and its associated noise, and the retrieved. Corresponds to the table 5.6.

The Nscale value for 30 layers depends on the high model which is 1.5 and the low is 0.6, only to the tropospheric layers.

It is noteworthy that in the models in which more numbers of layers are used, it is possible to better visualize the 22 GHz line of water vapor, including its peak.

The PWV results retrieved for the site in each case for 30 layers are: **high model: 5.55mm** with an error of 0.36% and **low model: 2.23mm** with an error of 0.45%; with respect to the real value.

TABLE 5.5. Water vapor values for each of the spectra evaluated (priori, simulated and retrieved) for the 15-layer low model.

Layer	Pressure (mbar)	Prior	Simulated	Retrieved	Statistical uncertainties
1	10	4.9×10^{-6}	4.9×10^{-6}	5.2×10^{-6}	9.1×10^{-7}
2	50	4.4×10^{-6}	4.4×10^{-6}	3.4×10^{-6}	1.1×10^{-6}
3	100	5.1×10^{-6}	2.6×10^{-6}	3.8×10^{-6}	2.4×10^{-6}
4	150	1.5×10^{-5}	7.6×10^{-6}	1.1×10^{-5}	7.0×10^{-6}
5	200	6.0×10^{-5}	3.0×10^{-5}	2.9×10^{-5}	2.5×10^{-5}
6	250	1.5×10^{-4}	7.3×10^{-5}	6.3×10^{-5}	5.8×10^{-5}
7	300	2.4×10^{-4}	1.2×10^{-4}	1.2×10^{-4}	1.0×10^{-4}
8	350	3.5×10^{-4}	1.7×10^{-4}	1.9×10^{-4}	1.5×10^{-4}
9	400	4.9×10^{-4}	2.5×10^{-4}	2.7×10^{-4}	2.2×10^{-4}
10	450	7.1×10^{-4}	3.6×10^{-4}	3.9×10^{-4}	3.1×10^{-4}
11	500	9.9×10^{-4}	4.9×10^{-4}	4.9×10^{-4}	4.3×10^{-4}
12	550	1.3×10^{-3}	6.4×10^{-4}	5.6×10^{-4}	5.4×10^{-4}
13	600	1.6×10^{-3}	7.9×10^{-4}	6.0×10^{-4}	6.5×10^{-4}
14	650	2.1×10^{-3}	1.0×10^{-3}	8.1×10^{-4}	8.5×10^{-4}
15	700	2.7×10^{-3}	1.4×10^{-3}	1.8×10^{-3}	5.1×10^{-4}

5.3.1   Vertical profiles in Cerro Ventarrones

It is also possible to incorporate realistic vertical profiles of water vapor from the site's maximum pressure altitude of 715 mbar to the mesosphere below 0.1 mbar. The model is based on NASA MERRA2 data, where the H2O mix ratio was made over the data acquisition period, including all hours of the day, for each MERRA pressure level.

The following figures show these quartile profiles of pressure vs. water vapor for the a priori data and the recovered of the site for the troposphere from the MERRA2 data and the recovery exercise carried out previously, for the three models, for 5 layers, 15 layers, and 30 layers, considering, in the same way, the moments in which the recovered profile had higher relative humidity above the a priori (high) and when it did not (low).

For the model involving 5 layers are presented in figures (5.13) and (5.14). If the profiles evaluated simulated from the previous section are added to these graphs, it is possible to find an average value for water vapor between the a priori and the recovered. In figures (5.15) and (5.16) it is possible to notice it for the 5-layer model in both, high and low positions, with the simulated too.

In these graphs, it is possible to visualize the relationship that exists between the data, and in some cases, they overlap; that is, our recoveries are close to the real values and the a priori values previously taken with the MERRA2 of the place (Cerro Ventarrones).

This same exercise of realistic vertical profiles of water vapor from the site's maximum pressure altitude at 715 mbar to the mesosphere below 0.1 mbar based on NASA MERRA2 data with a ratio of H_2O mixture during the data acquisition period, including all hours of the day, for each MERRA2 pressure level, it is also possible to do it for the 15 and 30 layer models, showing the pressure quartiles vs. water vapor for the a priori and recovered data
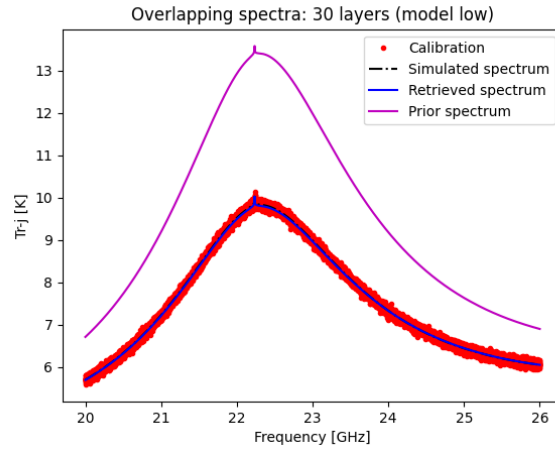
FIGURE 5.12. Representation of the three (3) spectra of water vapor studied for a model with 30 layers. Note that for this case, the prior contains much more water than the retrieved model. It is also notable to observe the simulated spectrum and its associated noise, and the retrieved. Corresponds to the table 5.7.
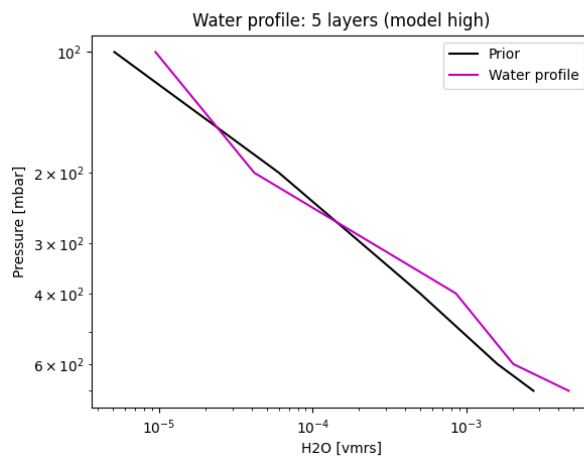
FIGURE 5.13. Water vapor quantile profiles over a decade over Cerro Ventarrones, based on NASA MERRA2 reanalysis data, for the tropospheric layers in a model where only 5 layers are considered and the recovered profile has higher humidity than the a priori (high). It is possible to notice the very similar relationship between both data for water vapor.
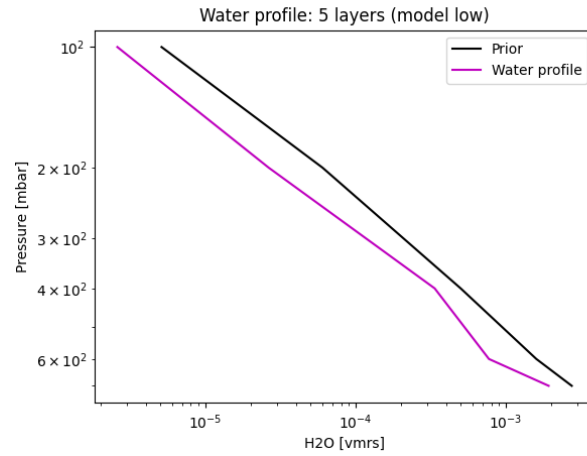
FIGURE 5.14. Water vapor quantile profiles over a decade over Cerro Ventarrones, based on NASA MERRA2 reanalysis data, for tropospheric layers in a model where only 5 layers are considered and the recovered profile has lower moisture than the a priori (low). It is possible to notice that the recovered profile is below the a priori, denoting the higher relative humidity in the a priori.
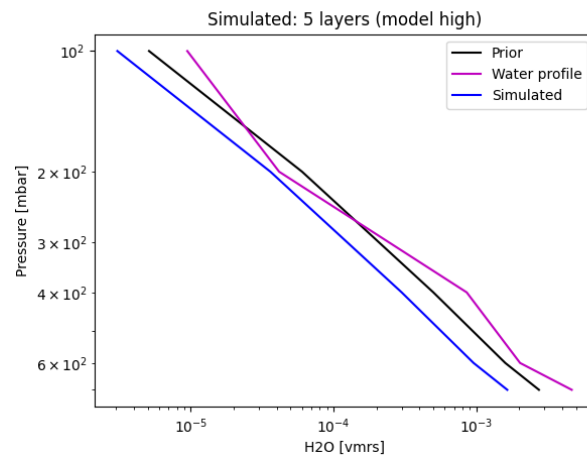
FIGURE 5.15. Water vapor quantile profiles over a decade over Cerro Ventarrones, based on NASA MERRA2 reanalysis data, for the tropospheric layers in a model where only 5 layers are considered and the recovered profile has higher humidity than the a priori (high). Here is the simulated model showing a slightly drier profile than the previous ones.

TABLE 5.6. Water vapor values for each of the spectra evaluated (priori, simulated and retrieved) for the 30-layer high model.

Layer	Pressure (mbar)	Prior	Simulated	Retrieved	Statistical uncertainties
1	0.3	6.8×10^{-6}	6.8×10^{-6}	6.9×10^{-6}	3.2×10^{-6}
2	0.4	6.8×10^{-6}	6.8×10^{-6}	6.9×10^{-6}	3.4×10^{-6}
3	0.5	6.8×10^{-6}	6.8×10^{-6}	6.9×10^{-6}	3.4×10^{-6}
4	0.7	6.7×10^{-6}	6.7×10^{-6}	6.8×10^{-6}	3.3×10^{-6}
5	1	6.6×10^{-6}	6.6×10^{-6}	6.5×10^{-6}	3.2×10^{-6}
6	2	6.3×10^{-6}	6.3×10^{-6}	5.9×10^{-6}	2.7×10^{-6}
7	3	6.0×10^{-6}	6.0×10^{-6}	6.0×10^{-6}	2.8×10^{-6}
8	4	5.8×10^{-6}	5.8×10^{-6}	5.8×10^{-6}	2.8×10^{-6}
9	5	5.6×10^{-6}	5.6×10^{-6}	5.6×10^{-6}	2.7×10^{-6}
10	7	5.2×10^{-6}	5.2×10^{-6}	5.2×10^{-6}	2.5×10^{-6}
11	10	4.9×10^{-6}	4.9×10^{-6}	5.0×10^{-6}	2.4×10^{-6}
12	20	4.6×10^{-6}	4.6×10^{-6}	5.3×10^{-6}	1.9×10^{-6}
13	30	4.6×10^{-6}	4.6×10^{-6}	5.3×10^{-6}	2.1×10^{-6}
14	40	4.5×10^{-6}	4.5×10^{-6}	5.1×10^{-6}	2.2×10^{-6}
15	50	4.4×10^{-6}	4.4×10^{-6}	4.9×10^{-6}	2.2×10^{-6}
16	70	9.4×10^{-6}	9.4×10^{-6}	5.0×10^{-6}	2.1×10^{-6}
17	100	5.1×10^{-6}	7.7×10^{-6}	5.7×10^{-6}	2.5×10^{-6}
18	150	1.5×10^{-5}	2.3×10^{-5}	1.8×10^{-6}	7.0×10^{-6}
19	200	6.0×10^{-5}	9.0×10^{-5}	7.1×10^{-5}	2.5×10^{-5}
20	250	1.5×10^{-4}	2.2×10^{-4}	1.8×10^{-4}	5.9×10^{-5}
21	300	2.4×10^{-4}	3.7×10^{-4}	3.6×10^{-4}	1.0×10^{-4}
22	350	3.5×10^{-4}	5.2×10^{-4}	6.1×10^{-4}	1.5×10^{-4}
23	400	4.9×10^{-4}	7.5×10^{-4}	9.6×10^{-4}	2.2×10^{-4}
24	450	7.1×10^{-4}	1.1×10^{-3}	1.4×10^{-3}	3.1×10^{-4}
25	500	9.9×10^{-4}	1.5×10^{-3}	1.6×10^{-3}	4.3×10^{-4}
26	550	1.3×10^{-3}	1.9×10^{-3}	1.4×10^{-3}	5.4×10^{-4}
27	600	1.6×10^{-3}	2.4×10^{-3}	1.1×10^{-3}	6.5×10^{-4}
28	650	2.1×10^{-3}	3.1×10^{-3}	1.8×10^{-3}	8.5×10^{-4}
29	700	2.7×10^{-3}	4.4×10^{-3}	6.4×10^{-3}	7.1×10^{-4}
30	715	2.9×10^{-3}	4.5×10^{-3}	5.6×10^{-3}	1.4×10^{-3}

of the site for the troposphere, considering, in the same way, the moments in which the recovered profile had higher relative humidity above the a priori (high) and when not (low). They can be seen in figures (5.17) and (5.18) for the vertical profiles of the 15-layer model and figures (5.21) and (5.22) for the 30-layer model. In the same way, the simulated profile is incorporated to observe the three incorporated profiles taking into account the scale factor Nscale of the simulated, in figures (5.19) and (5.20) for the 15-layer model and figures (5.23) and (5.24) for the 30-layer model.

The median profiles are used for the model, with layer boundaries matching the MERRA2 pressure levels. When constructing an AM model configuration file from this type of profile data, the base layer temperatures are taken directly from the temperature profile at the limiting pressure of the layer, but the water vapor mixing ratios must be approximate their weighted averages by column density over the entire layer. Thus, in the model file the base layer temperatures are the mean MERRA2 temperatures at the corresponding pressure levels, while the H_2O mixing ratios are the average of their values at the upper and lower limit pressures of the layer.

TABLE 5.7. Water vapor values for each of the spectra evaluated (priori, simulated and retrieved) for the 30-layer low model.

Layer	Pressure (mbar)	Prior	Simulated	Retrieved	Statistical uncertainties
1	0.3	6.8×10^{-6}	6.8×10^{-6}	5.9×10^{-6}	3.1×10^{-6}
2	0.4	6.8×10^{-6}	6.8×10^{-6}	6.6×10^{-6}	3.4×10^{-6}
3	0.5	6.8×10^{-6}	6.8×10^{-6}	6.6×10^{-6}	3.4×10^{-6}
4	0.7	6.7×10^{-6}	6.7×10^{-6}	6.6×10^{-6}	3.3×10^{-6}
5	1	6.6×10^{-6}	6.6×10^{-6}	6.5×10^{-6}	3.2×10^{-6}
6	2	6.3×10^{-6}	6.3×10^{-6}	6.3×10^{-6}	2.6×10^{-6}
7	3	6.0×10^{-6}	6.0×10^{-6}	6.1×10^{-6}	2.8×10^{-6}
8	4	5.8×10^{-6}	5.8×10^{-6}	5.9×10^{-6}	2.8×10^{-6}
9	5	5.6×10^{-6}	5.6×10^{-6}	5.8×10^{-6}	2.7×10^{-6}
10	7	5.2×10^{-6}	5.2×10^{-6}	5.6×10^{-6}	2.5×10^{-6}
11	10	4.9×10^{-6}	4.9×10^{-6}	5.4×10^{-6}	2.7×10^{-6}
12	20	4.6×10^{-6}	4.6×10^{-6}	4.9×10^{-6}	1.8×10^{-6}
13	30	4.6×10^{-6}	4.6×10^{-6}	4.4×10^{-6}	2.1×10^{-6}
14	40	4.5×10^{-6}	4.5×10^{-6}	4.3×10^{-6}	2.2×10^{-6}
15	50	4.4×10^{-6}	4.4×10^{-6}	4.2×10^{-6}	2.2×10^{-6}
16	70	9.4×10^{-6}	9.4×10^{-6}	4.1×10^{-6}	2.1×10^{-6}
17	100	5.1×10^{-6}	3.1×10^{-6}	4.6×10^{-6}	2.5×10^{-6}
18	150	1.5×10^{-5}	9.1×10^{-6}	1.0×10^{-5}	6.9×10^{-6}
19	200	6.0×10^{-5}	3.6×10^{-5}	1.8×10^{-5}	2.5×10^{-5}
20	250	1.5×10^{-4}	8.8×10^{-5}	3.2×10^{-5}	5.8×10^{-5}
21	300	2.4×10^{-4}	1.5×10^{-4}	1.3×10^{-4}	1.0×10^{-4}
22	350	3.5×10^{-4}	2.1×10^{-4}	2.9×10^{-4}	1.5×10^{-4}
23	400	4.9×10^{-4}	2.9×10^{-4}	5.0×10^{-4}	2.2×10^{-4}
24	450	7.1×10^{-4}	9.3×10^{-4}	6.8×10^{-4}	3.1×10^{-4}
25	500	9.9×10^{-4}	5.9×10^{-4}	6.8×10^{-4}	4.3×10^{-4}
26	550	1.3×10^{-3}	7.7×10^{-4}	4.1×10^{-4}	5.4×10^{-4}
27	600	1.6×10^{-3}	9.6×10^{-4}	5.8×10^{-5}	6.5×10^{-4}
28	650	2.1×10^{-3}	1.2×10^{-3}	2.3×10^{-4}	8.5×10^{-4}
29	700	2.7×10^{-3}	1.6×10^{-3}	2.8×10^{-3}	7.1×10^{-4}
30	715	2.9×10^{-3}	1.8×10^{-3}	3.9×10^{-3}	1.4×10^{-3}

This model uses default pressure-enlarged line shapes from ground level to the mid-stratosphere. Remember also the importance of the Doppler broadening that becomes significant in relation to the pressure broadening near the stratopause. So in this case we focus directly with the tropospheric layers in particular.

The model configuration file takes several command line parameters to set the range and resolution of the frequency grid, the zenith angle of observation (0 deg), the surface temperature, and the scale factor applied to the tropospheric water vapor profile. To model variations in total precipitable water vapor over the site in a manner that approximates the natural variation of the water vapor mixing ratio profile and its fluctuations.

In these graphs from figure (5.17) to figure (5.24) it is possible to visualize, as with the 5-layer model, the relationship that exists between the data, and that in some cases they
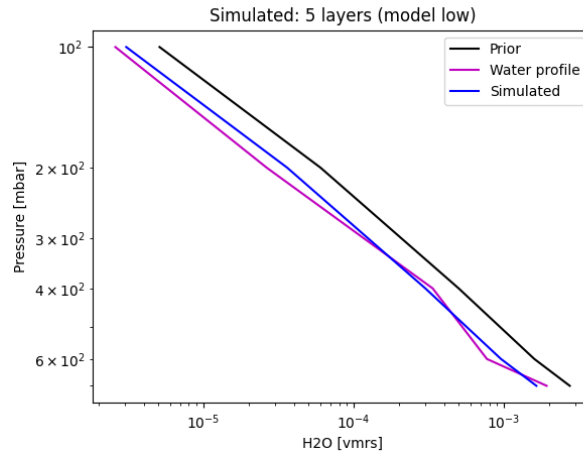
FIGURE 5.16. Water vapor quantile profiles over a decade over Cerro Ventarrones, based on NASA MERRA2 reanalysis data, for tropospheric layers in a model where only 5 layers are considered and the recovered profile has lower moisture than the a priori (low). In this case, the simulated profile is interspersed between the two previous profiles.
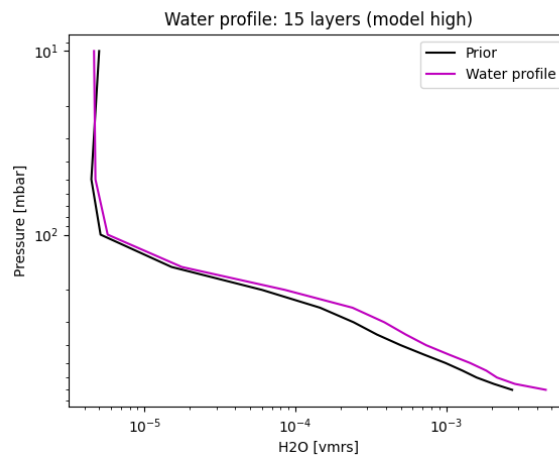
FIGURE 5.17. Water vapor quantile profiles over a decade over Cerro Ventarrones, based on NASA MERRA2 reanalysis data, for the tropospheric layers in a model where only 15 layers are considered and the recovered profile has higher humidity than the a priori (high). It is possible to notice the very similar relationship between both data for water vapor.
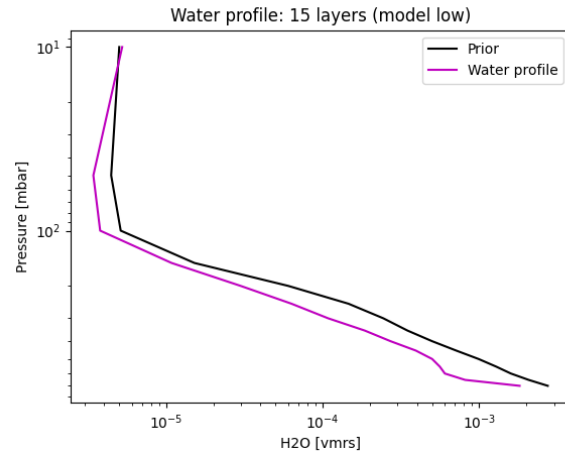
FIGURE 5.18. Water vapor quantile profiles over a decade over Cerro Ventarrones, based on NASA MERRA2 reanalysis data, for tropospheric layers in a model where only 15 layers are considered and the recovered profile has lower moisture than the a priori (low). It is possible to notice that the recovered profile is below the a priori, denoting the higher relative humidity in the a priori.
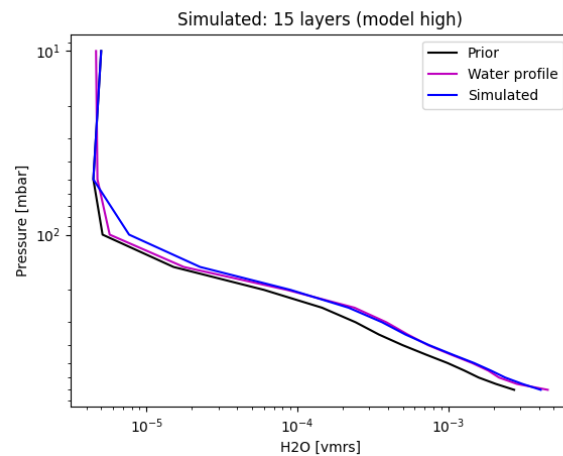
FIGURE 5.19. Water vapor quantile profiles over a decade over Cerro Ventarrones, from NASA MERRA-2 reanalysis data, for the tropospheric layers in a model where only 15 layers are considered and the recovered profile has higher humidity than the a priori (high). Here is the simulated model overlapping in the lower layers with the recovered profile, and in the higher layers we remember that they are considered the same as the priori.
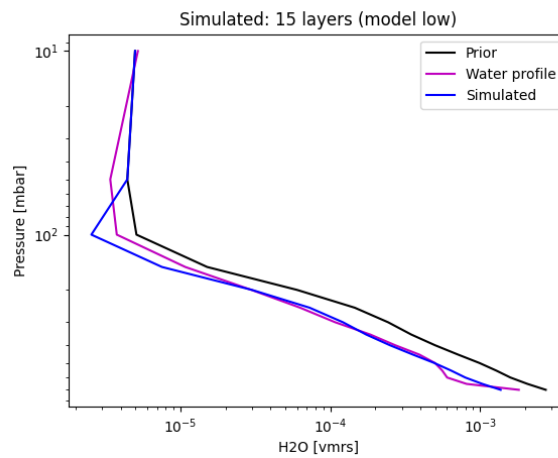
FIGURE 5.20. Water vapor quantile profiles over a decade over Cerro Ventarrones, from NASA MERRA2 reanalysis data, for the tropospheric layers in a model where only 15 layers model low. Here is the simulated model overlapping in the lower layers with the recovered profile, and in the higher layers we remember that they are considered the same as the priori, although a half-height offset is also observed.
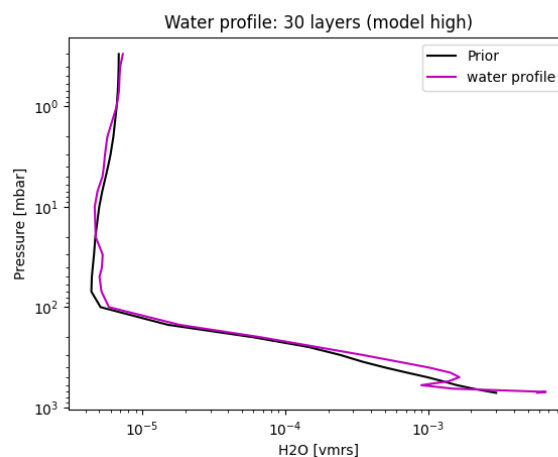
FIGURE 5.21. Decade water vapor quantile profiles over Cerro Ventarrones, based on NASA MERRA2 reanalysis data, for tropospheric layers in a model where all 30 layers are considered and the recovered profile has lower moisture than the a priori (low). Here is the priori model paired with the recovered, but it can see a gap in one of the lower layers.
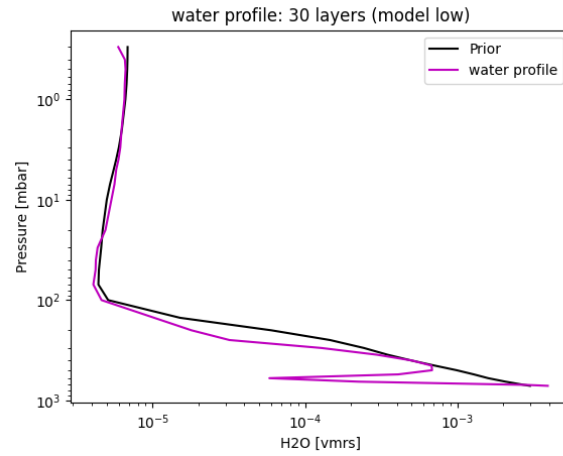
FIGURE 5.22. Decade water vapor quantile profiles over Cerro Ventarrones, based on NASA MERRA-2 reanalysis data, for tropospheric layers in a model where all 30 layers are considered and the recovered profile has lower moisture than the a priori (low). Here is the priori model paired with the recovered, but it can see a gap in one of the lower layers.
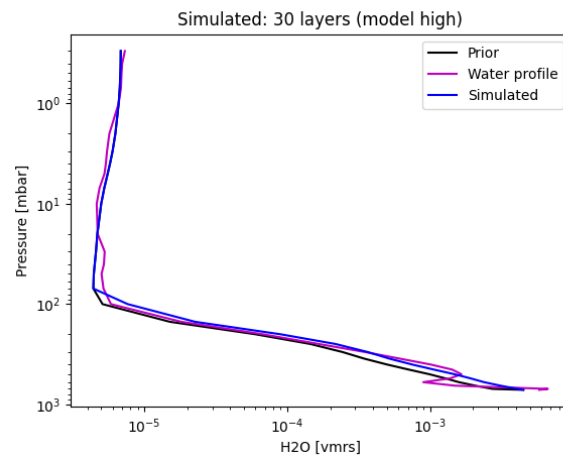
FIGURE 5.23. As in figure (5.21), the water vapor quantile profiles over a decade over Cerro Ventarrones are shown, based on NASA MERRA2 reanalysis data, for the tropospheric layers in a model where they are considered the 30 layers and the recovered profile have higher humidity than the a priori (low), and also the simulated profile. Here is the priori model paired with the recovered just like the simulated.
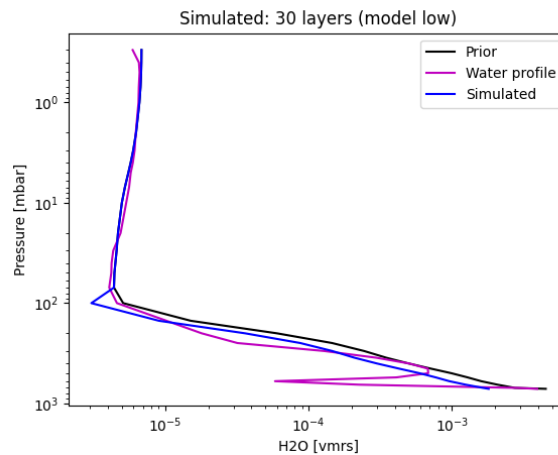
FIGURE 5.24. The water vapor quantile profiles over a decade over Cerro Ventarrones are shown, based on NASA MERRA2 reanalysis data, for the tropospheric layers in a model in which they are considered the 30 layers and the recovered profile has less moisture than the a priori (low), and also the simulated profile. Here is the priori model paired with the recovered, just like the simulated, the lag is shown in the lower layers.

overlap; that is, our recoveries are close to the real values, either the a priori values previously taken with the MERRA2 of the place (Cerro Ventarrones) and the simulated ones; which allows establishing a base that the running of the OEM simulations is on the right track.

Relationship between high and low models

To obtain a graph of profiles and thus be able to observe the differences between each of them, it is possible to make a vertical profile for each of the models proposed concerning the amount of relative humidity of the recovered a priori, that is, between the recovered profiles that have higher values of H_2O compared to the a priori (high) and those with less (low), for each model: 5 layers, 15 layers, and 30 layers. For them, a pressure (height) relationship is made concerning the difference between the simulated profile minus the recovered, and thus can calculate the differences between models between layers.

In graphs (5.25) and (5.26), it is possible to observe the differences that exist between the models of 5, 15, and 30 layers in the troposphere, it is notable that for the 30-layer model, it is more visible due to the lags presented in the Figures (5.21) and (5.22), there may be a problem in the average of the water vapor mixture at these heights. However, this detail is not yet well defined.
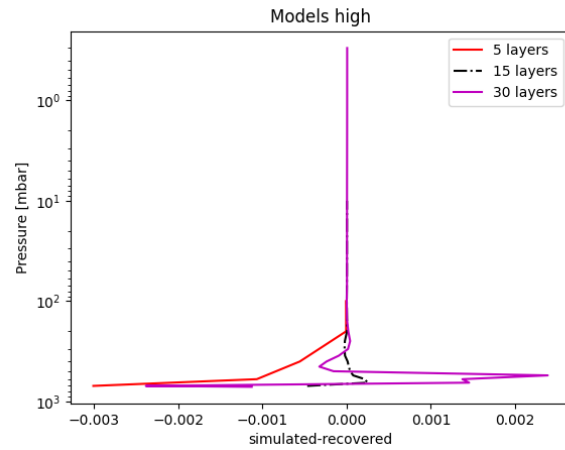
FIGURE 5.25. Relationship between the profiles of water vapor at 5, 15, 30 layers with respect to the height for those profiles whose relative humidity is greater than the priori, high models. The differences present in the values of H_2O for the troposphere depending on the layer model are observed.
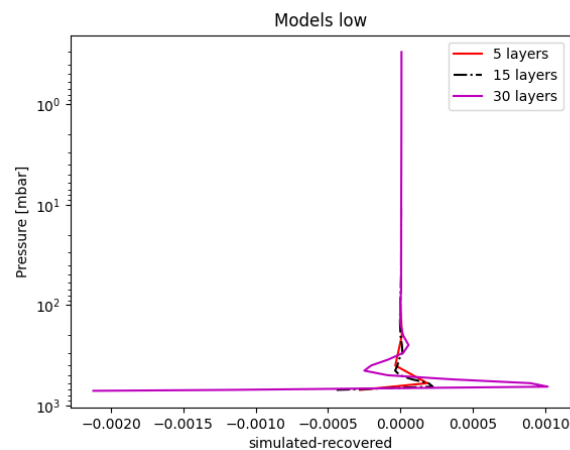
FIGURE 5.26. Relationship between the profiles of water vapor at 5, 15, 30 layers with respect to the height for those profiles whose relative humidity is lower than the priori, low models. The differences present in the values of H_2O for the troposphere depending on the layer model are observed.

Chapter 6

Conclusions, Current work and Future work

The specific objectives described in section (2.3) have been developed throughout this thesis. This work during a pandemic allowed for extensive analysis prior to implementation, leading to a detailed conceptual and design stage. We can conclude:

- The instrumental requirements for the 22 GHz radiometer prototype were defined, obtaining thirteen (13) critical prior guidelines that were taken into account for the instrument's design. Table (4.1) of section (4.1.1) shows the quantitative values and the qualitative expressions that validate these requirements. For a better understanding and details of verification methods, please read B.

- A preliminary analysis of the sensitivity of the radiometer was carried out, an important parameter that indicates the technological progress of the laboratory in light of state of the art found. As a result, $\Delta T_{min} = 0.54$ K.

- The radiometer's architecture consists of an analog part and a digital part that allows it to be at the forefront of spectroscopy and analysis of recovered data. This architecture evolved to figure (4.6), which allows the selective passing of the signal in a specific bandwidth that the digital part can control.

- The signal passage throughout the system was studied and designed, that is, for each analog component and for the digital block that makes up the radiometer, obtaining the pseudo-correlation equation that defines this architecture—equations from (4.28) to (4.31).

- The characterization of the components and the diagram was carried out using simulations through the AWR software, establishing the value of the noise temperature of the radiometer at $T_{sys} = 120.4$ K; relevant data to confirm the sensitivity of the instrument.

- A signal was generated that can reproduce the T_b of the atmosphere of the measurement site. This was accomplished through the AM and AWR programs. Its path through each component was evaluated in a spectrum showing the corresponding bandwidths of each

element.

- Two essential values were reached at the analog and digital parts interface: the integrated power at -24.057 dBm and the gain balance at 55.73 dB. These data allow the continuity of the passage of the signal to the digital card.

- A selection of the commercial components that were part of the radiometer was made. This was done through the electronic component sales platforms, allowing their technical specifications to be adjusted to the desired parameters. An analysis and simulation of each of them were carried out until reaching the list of the table (4.3) that is currently being acquired. and part of the costs of the analog components that have been acquired can also be observed.

-The concept of the OEM Best Estimation Method was introduced as the way to follow to carry out vertical recoveries of gaseous species from the atmosphere, in this case water vapor, as well as a step-by-step visualization of the spectra that can be recovered, simulated or a priori, which are of great importance when starting the observations with the instrument. For this, it was concluded that the OEM is the appropriate way to start with the recoveries using the AM software, and in some results that we obtained using real data from the site (Cerro Ventarrones) we were able to verify that the recovered vertical profiles are consistent with the a priori ones. and the errors regarding the recoveries and the actual values of the site are less than 1%; for the 5-layer model the high has an error of 0.30% and the low 0.75%, for the 15-layer model the high has an error of 0.64% and the low 0.1%, and finally, for the 30-layer model, the high has an error of 0.36% and the low 0.45%. This shows a breakthrough for a first approach in this area.

- The concept of vertical characterizations of atmospheric parameters was widely introduced, since it is possible to visualize in E the recovery theory, which will allow in the future to understand the dynamics of water vapor in the atmosphere in a range from 0 to 80 km, including troposphere, stratosphere and mesosphere, based on Rodgers (2000), as well as a small introduction of the next software to follow after AM for recoveries such as ARTS/Q-pack. Thus this instrument can serve as a support for astronomical observations.

On the other hand, the 22 GHz radiometer prototype project of the CePIA laboratory of the Department of Astronomy of the University of Concepción is currently developing various tasks in parallel, including:

1. The test assembly proposal is being made, that is, a description of the verification tests.

2. The vast majority of commercial components and the digital card have already been purchased.

3. The characterization of the commercial components is being carried out, the components of the IF stage have already been completed and the characterization process of the RF components is being defined.

4. Modeling is being carried out for the enclosure of the prototype in such a way that it can be transportable.

In subsequent phases of this thesis, it is intended to continue with the instrumental work that involves technical development, systems integration, laboratory tests and final assembly. To do this, the following steps must be followed:

1. Last acquisition of commercial components.

2. Carry out the respective characterization of the commercial components that are still missing.

3. Perform any laboratory tests that involve connecting the analog components.

4. Perform mechanical and digital development, which involves assembly testing, packaging, integration testing, and powering the radiometer.

5. Design appropriate calibration strategies.

6. Advance in a vertical atmospheric characterization of the water vapor that includes the kernels (sensitivity of the windows at different pressures) and that can be validated with other instruments in established sites.

7. The final prototype will be able to collect data at the University of Concepción and also in measurement campaigns in Cerro Ventarrones, Antofagasta Region.

8. Used for multiple purposes of analysis and atmospheric characterization, as support in astronomical observations, the wood production process, research in precision agriculture, among others.

Appendix A

AM software operation

AM (Atmospheric Model) software, The AM is compiled by the Smithsonian Astrophysical Observatory (SAO) Li et al. (2020). Is a tool for radiative transfer computations involving propagation through the atmosphere and other media at microwave through submillimeter wavelengths. The atmosphere can be modeled as hydrostatic plane-parallel or spherical layers. More generally, the program can be used for any problem that can be modeled as a narrow beam. The simplest AM propagation path model is illustrated in figure (A.1). Radiation, initially having a Planck spectrum at a background temperature T_0, propagates through the series of layers, which layers will represent horizontal strata in the atmosphere, making sequential and recursive calculations within the layers to be able to simulate the atmospheric behavior and the conditions of each one. However, a layer simply represents a segment of a propagation path, for example, a single layer could represent a horizontal path at constant pressure and temperature between two points in the atmosphere Paine (2012).

The radiative transfer model in AM makes several simplifying approximations, refraction is despised, and local thermodynamic equilibrium is assumed, meaning that molecular collisions suffice to maintain equality of the molecular excitation temperature and the gas kinetic temperature of the medium, even in the presence of coupling to a radiation field at a different effective temperature. Multiple scattering is neglected, and radiation is assumed to be unpolarized. The radiative transfer computation through the complete layer stack is carried out iteratively, allowing to obtain results with a specific frequency range, opacity, brightness temperature, and other variables, generating graphs that enable the model of atmospheric parameters of a particular place Cortés Guerrero et al. (2015).

In that sense, the AM software allows obtaining a large amount of data about the atmosphere considering the conditions of some observation place, since each site has particular conditions that make it unique. For this reason, the CePIA atmospheric sciences team has designed a model (model-annual-site.amc) within the AM that describes in great detail the conditions of Cerro Ventarrones (place where the data will be collected), in such a way that best represent the behavior of the atmosphere at the site.

This model uses certain input variables to work, these are: the minimum and maximum frequency in GHz, zenith angle in degrees, scale factor. From these input values, the model is capable of reconstructing the atmospheric behavior and delivering the specified output variables.
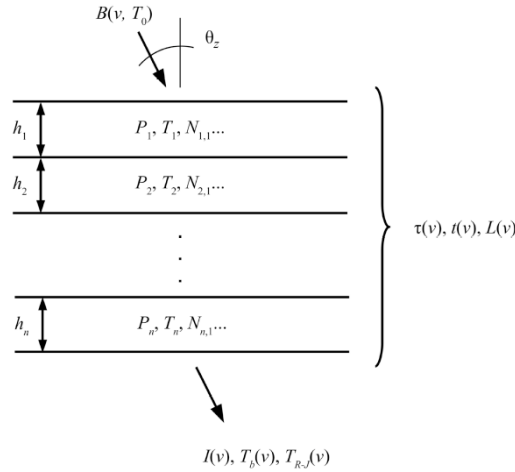
FIGURE A.1. The AM layer model. In this example, layer pressure and temperatures have been defined at the layer midpoints Paine (2012).

The propagation diagram of AM is illustrated in figure (A.1). At the beginning, the radiation has a Planck spectrum with a background temperature of T_0, which propagates through a series of layers. The parametrizations of the pressures P and temperatures T in different layers applied in AM are defined at the layer midpoints, and are presumed constant at each layer. Each layer contains various species, the type and column density of which are defined respectively. The basic spectral quantities calculated by AM are also expressed in figure (A.1), show spectral properties of the radiation in any layer that includes Rayleigh-Jeans brightness temperature and Planck brightness temperature.

Knowing that the input variables are supplied by the user, it is possible to manipulate the program within the ranges that are convenient, this program is used in such a way that we can reconstruct the operation of some instruments, in this sense, for example, the input frequencies can correspond to the minimum and maximum values of the filter that the instrument has (in this case 20 - 26 GHz), while with the zenith angle it is possible to simulate different air masses, and the scale factor applied to the tropospheric water vapor profile; this scale factor is used to model variations in the total precipitable water vapor over the observatory site in a manner which approximates the natural variation of the H_2O mixing ratio profile.

It is also necessary to indicate to the model the output variables that are needed and the units; the possible output variables are shown in table A.1. For this work, the brightness temperature in K, frequencies in GHz, radiance in $watt \cdot cm^{-2} \cdot GHz^{-1} \cdot sr^{-1}$, among others, are necessary.

The primary application areas for am are in radio astronomy and ground-based atmospheric radiometry, involving terrestrial propagation paths between ground and sky Paine (2012).

TABLE A.1. AM program output variables.

Output spectrum	Array-name	Unit
frequency	f	Hz, kHz, MHz, GHz, THz, cm^{-1}
opacity	tau	neper, dB
transmittance	tx	none
radiance	I	$watt \cdot cm^{-2} \cdot GHz^{-1} \cdot sr^{-1}$
radiance difference	I_{diff}	$watt \cdot cm^{-2} \cdot GHz^{-1} \cdot sr^{-1}$
Planck brightness temperature	T_b	K
Rayleigh-Jeans brightness temperature	T_{rj}	K
Rayleigh-Jeans system temperature	T_{sys}	K
Y-factor	Y	none
excess path or delay	L	km, m, cm, mm, um, s, ps, fs
absorption coefficient	k	internal

Appendix B

Requirements details

Description of the criteria and methods of validation of the technical instrumental requirements for the CePIA 22 GHz radiometer.

B.1 Frequency range

i. <u>Verification Criteria</u>: The expected frequency range is located, taking into account the central frequency to be measured. In this case, an idealization of expanding the range between 18 and 26 GHz can be made, which will depend on the information considered in the datasheets of each component that is located in the radio frequency (RF) stage.

ii. <u>Verification method</u>: It is possible to characterize using a VNA all the components of the receiver in their RF phase, extrapolate their S-parameters to the instrument, and verify that all of them are located in this amplified range. An example is in the antenna; verification can be done utilizing the S_{11} parameter pointing to the sky (without reflections) and seeing its frequency response. In the same way, it is possible to inject a tone into the input that allows the white noise to be visualized and to see how the power reacts to various bands in the output, hoping to observe some attenuation or gain fluctuation that may occur between the chosen frequency range.

B.2 Backend type

i. <u>Verification Criteria</u>   In the first instance, the outgoing voltages of the analog phase of the IF can be entered into the ADCs. The signal must be sampled in such a way that with the data taken, the analog signal can be reconstructed exactly. The spectrometer can focus on obtaining the spectral information contained in the captured radiation and measuring its spectral density that corresponds to the power distribution of said signal over the different frequencies (its spectrum) employing the Fourier transform. In general, a spectrometer accumulates multiple spectra to average the output noise and improve the signal-to-noise ratio of the spectrum, so its resolution must be small and contain high temporal stability.

At the output, it can be verified that the signal coming out of each spectrometer in each channel is balanced in phase and magnitude so that it can enter the digital hybrid. The different logic gates of the FPGA can calculate the pseudo-correlation in real time. The result

must be directly proportional to the difference between the temperature of the reference load and the antenna temperature. Finally, pass this information to a computer.

ii. <u>Verification method</u>: For the incoming voltage to the ADC to be adequate, it can be verified by establishing a necessary power to ensure its operation. Measurements such as their frequency response, the SFDR (spurious free dynamic range), the SINAD (signal-to-noise and distortion ratio), and the ENOB (effective number of bits) are used to characterize the performance of ADCs.

To characterize the performance of the spectrometers, spectra are presented using input tones of different random frequencies that fall exactly in the center of the spectral channel, chosen in such a way as to allow the analysis of different important factors, such as the dynamic range (SFDR) of the spectrometer across the band and temporal stability.

To verify that the output signals of the spectrometer have been balanced, a script is made that allows knowing that both lines are balanced in phase and magnitude.

To calibrate the digital hybrid, it can be done by sweeping the RF source in frequency with a step related to the number of channels implemented in the digital spectrometer; during the frequency sweep of the RF source, the output power of the tone is measured in the IF output produced by the RF tone, then the software compares the output signals of the channels, characterizing the behavior of the analog components, this characterization allows determining the constants that compensate for the different imbalances presented in the analog part of the receiver.

To verify the demodulation, it is possible to eliminate this stage and observe at the output that the signal has an associated noise $1/f$, then perform another measurement with the demodulation included, and the change and the need to perform this mitigation will be seen. Verification for digital pseudo-correlation is done by measuring the FPGA.

B.3   Measurement altitude range

i. <u>Verification Criteria</u>: To determine the bandwidth range, as well as the spectral resolution, the same criteria established for the channel bandwidth, are used: it is taken into account where the attenuation power is minimum. The criteria for defining bandwidth is a 5 dB drop in power from the maximum. The standard establishes that the reflection coefficient within the bandwidth is the one achieved, not the expected one, and the reported point is the maximum power.

ii. <u>Verification method</u>: The way to verify the channel is to measure the output power on each channel; according to this, it can be proved where the expected center frequency per channel is. The bandwidth per channel is confirmed by measuring from the maximum power the drop of 5 dB on each side; according to that power measurement it is verified where the expected bandwidth per channel is, and that specific range is taken as the bandwidth of choice.

B.4   Bandwidth/channel

i. <u>Verification Criteria</u>: Considering a bandwidth per channel, it is taken into account where the attenuation power is minimum. The criteria for defining bandwidth is a 5 dB drop in power from the maximum. The standard establishes that the reflection coefficient within the bandwidth is the one achieved, not the expected one, and the reported point is the maximum power.

ii. <u>Verification method</u>: The way to verify the channel is to measure the output power in each channel; according to this, it is possible to verify where the expected center frequency per channel is. The bandwidth per channel is confirmed by measuring from the maximum power the drop of 5 dB on each side; according to that power measurement it is verified where the expected bandwidth per channel is, and that specific range is taken as the bandwidth of choice. Similarly, you can consider injecting a tone into the system, taking five (5) frequencies at random and verifying their location per channel.

B.5   Number of channels

i. <u>Verification criteria</u>: It will depend on the spectrometer configuration, it is defined in the FFT.

ii. <u>Verification method</u>: A tone is injected at the center frequency of each channel and the number of previously selected channels is verified.

B.6   PWV measuring range

i. <u>Verification Criteria</u>: The maximum range is defined by measuring the amount of PWV in the line of sight, according to the instrument and the physics of the measurement process.

ii. <u>Verification method</u>: The detection of water vapor in the atmosphere is based on the knowledge of the emitted power in the spectrum band that we wish to observe (62.5 kHz). Measuring this power allows detecting the shape and amplitude of the spectral lines using a model and obtaining the amount of PWV that the line produced in real time. Measurements will are made or, better said, get values of the brightness temperature T_b at the City of Concepción (12 masl), and Cerro Ventarrones (2800 masl) is intended to verify the PWV column in units of mm and determine its vertical profile.

B.7   Water vapor retrieval

i. <u>Verification Criteria</u>: To define it, a procedure must be established that can convert gloss temperature measurements to an atmospheric water vapor profile. A general design of the observation system is carried out, considering the characteristics of the instrument and an in situ observation geometry. This design must include the advanced model, the identification

of the atmospheric parameters, the a priori information, and the optimization of the proto-type, such as the noise temperature and the spectral response, among others.

ii. <u>Verification method</u>: The signal should be considered as the gross output of the instru-ment in power units before the effects of the calibration are applied. As appropriate, initial values and variances must be set for all parameters, along with covariance matrices. A priori information and a description of the previous state of the atmosphere will be needed; a sim-ulation is proposed that should be able to produce the following diagnostics of the observing system:

- Sensitivity of the measured signal to the target quantities. This includes the matrix of weighting functions.
- Sensitivity of retrieval to target quantities. This includes the average of the kernel matrix.
- The contributions to the covariance of the total retrieval error of the measurement noise and the uncertainties in each of the independent parameters of the model.
- Have a realistic a priori atmosphere source and evaluate the smoothing error.
- The information content of Shannon and the degrees of freedom for the signal.

These diagnostics allow you to determine whether the observing system can produce results with resolution and precision and identify which sources of error need further atten-tion.

B.8   Data extraction interface

i. <u>Verification Criteria</u>: The graphic interface for control and monitoring is a basic terminal that allows data to be downloaded through a command line, and through a web server, this internal address can be opened, and the data can be graphically displayed.

ii. <u>Verification method</u>: The data extraction interface can be verified by downloading and viewing it through the terminals with the use of the command line.

B.9   General characteristics

i. <u>Verification Criteria</u>: What defines the plug and play is the expected electrical energy to ensure the performance of the autonomous operation of the instrument.

ii. <u>Verification method</u>: The expected amount of electrical energy is measured, and according to that voltage (or current) when plugging in, the instrument should turn on and work.

Appendix C

Description of the mathematical analysis of the signal

Next, the mathematical analysis of the signal in its passage through each component of the radiometer is detailed, both through the analog stage and through the digital stage, until reaching the equation of interest, the pseudo-correlation equation.

C.1 Mathematical analysis: analog frontend and backend

Two signals enter the radiometer; one of them is the atmospheric T_b by the horn or antenna, and a noise or voltage signal generated by a noise diode and controlled by a commutator switch (SC) is denoted as T_L. The voltages of the input signals are expressed:

$$V_{Tb} = V_{Tb}cos\left(\omega_{RF/USB}\right)t + V_{Tb}cos\left(\omega_{RF/LSB}\right)t \tag{C.1}$$

$$V_{TL} = V_{TL}cos\left(\omega_{RF/USB}\right)t + V_{TL}cos\left(\omega_{RF/LSB}\right)t \tag{C.2}$$

Where the amplitudes of the temperatures are different, and the USB (Upper Side Band) and other LSB (Lower Side Band) components of the signal are represented by $\omega_{RF/USB}$ and $\omega_{RF/LSB}$ respectively. It is then possible to express the terms related to USB and LSB as a function of a LO mix frequency, such as:

$$\omega_{RF/USB} = \omega_{LO} + \omega_{IF/USB} \tag{C.3}$$

$$\omega_{RF/LSB} = \omega_{LO} - \omega_{IF/LSB} \tag{C.4}$$

Using the new variables, in V_{Tb} and V_{TL} the input voltages can be expressed as:

$$V_{Tb} = V_{Tb}cos(\omega_{LO} + \omega_{IF/USB})t + V_{Tb}cos(\omega_{LO} - \omega_{IF/USB})t \tag{C.5}$$

$$V_{TL} = V_{TL}cos(\omega_{LO} + \omega_{IF/USB})t + V_{TL}cos(\omega_{LO} - \omega_{IF/USB})t \tag{C.6}$$

These RF voltages are transmitted and entered in a 180° hybrid and at the output they bifurcate into two branches, figure (5.6). A 180° hybrid is a four-port network with a 180° phase shift between the two output ports, that is, the voltage outputs differ in phase by 0° or 180° depending on the port Maas (1986).
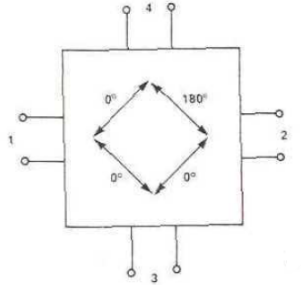
FIGURE C.1. 180° ideal hybrid, output port offset angles shown. Source: Maas (1986)

When two voltages are input to two ports in a 180° hybrid, one output port will contain the sum of the two inputs, while the other port will contain the difference between these, figure (C.2).
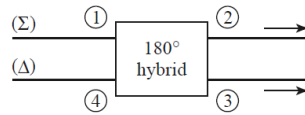
FIGURE C.2. Symbol for a 180° hybrid junction. Source: Pozar (2011)

The outputs are expressed by a single, symmetric matrix that implies the specific phase shift between the input and output of the ports.

$$[S] = \frac{-j}{\sqrt{2}} \begin{bmatrix} 0 & 1 & 1 & 0 \\ 1 & 0 & 0 & -1 \\ 1 & 0 & 0 & 1 \\ 0 & -1 & 1 & 0 \end{bmatrix}$$

The outputs are 180° out of phase and denoted as V_1 and V_2 in the general diagram, figure (C.3), they represent the sum and difference of the input signals.

$$V_1 = \frac{-j}{\sqrt{2}} \left(V_{Tb} + V_{TL} \right) \tag{C.7}$$

$$V_2 = \frac{-j}{\sqrt{2}} \left(V_{Tb} - V_{TL} \right) \tag{C.8}$$

$$V_1 = \frac{-j}{\sqrt{2}} \left[V_{Tb} cos(\omega_{LO} + \omega_{IF/USB})t + V_{Tb} cos(\omega_{LO} - \omega_{IF/LSB})t) \right.$$

$$\left. + V_{TL} cos(\omega_{LO} + \omega_{IF/USB}t) - V_{TL} cos(\omega_{LO} - \omega_{IF/LSB}) \right] \tag{C.9}$$
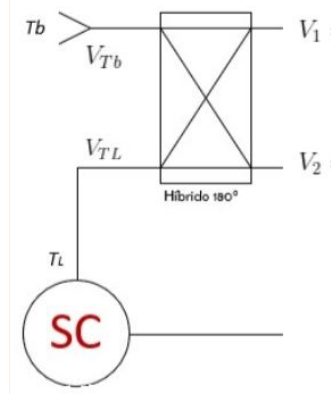
FIGURE C.3. Schematic of the 180° hybrid, input and output voltages for the 180° hybrid of the CePIA 22 GHz radiometer.

$$V_2 = \frac{-j}{\sqrt{2}} \left[V_{Tb} cos(\omega_{LO} + \omega_{IF/USB})t + V_{Tb} cos(\omega_{LO} - \omega_{IF/LSB})t \right)$$

$$-V_{TL} cos(\omega_{LO} + \omega_{IF/USB}t) + V_{TL} cos(\omega_{LO} - \omega_{IF/LSB})] \quad (C.10)$$

After the hybrid, in each of the branches it is considered to include a low noise amplifier (LNA) and a bandpass filter (BPF) considered as a block, figure (C.4), that allows to amplify the signal offering gain to the g_1 and g_2 system , and a loss is associated with it, which increases the noise temperature of the system, n_1 for the upper branch and n_2 for the lower branch. In addition, to filtering the pass frequency, this design allows to achieve a Single Side Band (SSB) configuration where a side band is eliminated.
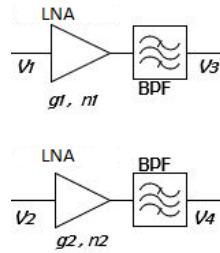
FIGURE C.4. Schematic of the amplifier block and the RF filter for each branch.

Reference noise voltages are denoted as:

$$n_1 = n_1 cos(\omega_{LO} + \omega_{IF})t \quad (C.11)$$

$$n_2 = n_2 cos(\omega_{LO} + \omega_{IF})t \quad (C.12)$$

In figure (C.4), it is noted that V_1 and V_2 are the input voltages in this block, therefore the output voltages V_3 and V_4 already they do not have a sideband according to the previous consideration, so:

$$V_3 = g_1[V_1 + n_1] = g_1 \left[\frac{-j}{\sqrt{2}} (V_{Tb} + V_{TL}) + n_1 \right] \tag{C.13}$$

$$V_4 = g_2[V_2 + n_2] = g_2 \left[\frac{-j}{\sqrt{2}} (V_{Tb} - V_{TL}) + n_1 \right] \tag{C.14}$$

$$V_3 = g_1 \left[\frac{-j}{\sqrt{2}} \left(V_{Tb} cos \left(\omega_{LO} + \omega_{IF} \right) t + V_{TL} cos \left(\omega_{LO} + \omega_{IF} \right) t \right) + n_1 cos \left(\omega_{LO} + \omega_{IF} \right) t \right] \tag{C.15}$$

$$V_4 = g_2 \left[\frac{-j}{\sqrt{2}} \left(V_{Tb} cos \left(\omega_{LO} + \omega_{IF} \right) t - V_{TL} cos \left(\omega_{LO} + \omega_{IF} \right) t \right) + n_2 cos \left(\omega_{LO} + \omega_{IF} \right) t \right] \tag{C.16}$$

After this «block», the mixers are located, one for each branch, figure (5.7), which, together with the LO and the incoming RF signal, produce a lower bandwidth signal or intermediate frequency (IF) signal.

In figure (5.7), it is possible to see a power divider, which is a component that preserves the frequency of the local oscillator but decreases the power of each branch by -3 dB.

The mixing process can change the signal phase by a constant value, so there is a phase shifter (PS) for each branch (represented by ϕ). These calculations will be 90°, so multiply by two (2) for the subharmonic mixer, which will modulate the phase and give the mixer's output a difference of 180°.

The expression for the LO voltage is:

$$V_{LO} = V_{LO} cos \left(\omega_{LO} t + \phi \right) \tag{C.17}$$

If $\phi = 180°$, using $cos(\alpha \pm \beta) = cos\alpha cos\beta \mp sen\alpha sen\beta$

$$V_{LO}^{\phi=180°} = V_{LO} cos(\omega_{LO} + \pi)t = -V_{LO} cos(\omega_{LO})t \tag{C.18}$$

If $\phi = 0°$

$$V_{LO}^{\phi=0°} = V_{LO} cos(\omega_{LO})t \tag{C.19}$$

The input voltages to the mixers are V_3 and V_4, is mixed (multiplied) with V_{LO}. Therefore, the outputs V_5 and V_6:

$$V_5 = KV_3 \times V_{LO}^{\phi=180°} \tag{C.20}$$

$$V_6 = KV_4 \times V_{LO}^{\phi=0°} \tag{C.21}$$

It is assumed that K is the mixer constant that indicates the efficiency of the element. The outputs V_5 and V_6 are:

$$V_5 = \frac{Kg_1}{\sqrt{2}} \left[V_{Tb} \left(\omega_{LO} + \omega_{IF} \right) t + V_{TL} \left(\omega_{LO} + \omega_{IF} \right) t + n_1 \left(\omega_{LO} + \omega_{IF} \right) t \right] \times V_{Tb} \left(\omega_{LO} t + \phi \right)$$
(C.22)

Using $cos\alpha cos\beta = \frac{cos(\alpha+\beta)+cos(\alpha-\beta)}{2}$,

$$V_5 = \frac{KV_{LO}g_1}{\sqrt{2}} \left[V_{Tb} \left[cos((\omega_{LO} + \omega_{IF} + \omega_{LO})t + \phi) + cos((\omega_{LO} + \omega_{IF} - \omega_{LO})t + \phi) \right] \right.$$

$$+ V_{TL} \left[cos((\omega_{LO} + \omega_{IF} + \omega_{LO})t + \phi) + cos((\omega_{LO} + \omega_{IF} - \omega_{LO})t + \phi) \right]$$

$$+ n_1 \left[cos((\omega_{LO} + \omega_{IF} + \omega_{LO})t + \phi) + cos((\omega_{LO} + \omega_{IF} - \omega_{LO})t + \phi) \right]] \quad \text{(C.23)}$$

Then,

$$V_5 = \frac{KV_{LO}g_1}{\sqrt{2}} \left[V_{Tb} \left[cos((2\omega_{LO} + \omega_{IF})t + \phi) + cos((\omega_{IF}t) + \phi) \right] \right.$$

$$+ V_{TL} \left[cos((2\omega_{LO} + \omega_{IF})t + \phi) + cos((\omega_{IF}t) + \phi) \right]$$

$$+ n_1 \left[cos((2\omega_{LO} + \omega_{IF})t + \phi) + cos((\omega_{IF}t) + \phi) \right]] \quad \text{(C.24)}$$

Selecting the frequencies directly related to ω_{IF}, since these frequencies correspond to the converted signal, in addition to that $2\omega_{LO} + \omega_{IF}$ is related to frequencies $>> 6$ GHz, higher than the bandwidth of the IF:

$$V_5 = \frac{KV_{LO}g_1}{\sqrt{2}} \left[V_{Tb} cos \left((\omega_{IF}t) + \phi \right) + V_{TL} cos \left((\omega_{IF}t) + \phi \right) + n_1 cos \left((\omega_{IF}t) + \phi \right) \right] \quad \text{(C.25)}$$

For $\phi = 180°$, V_5 is:

$$V_5^{180°} = \frac{KV_{LO}g_1}{\sqrt{2}} \left[V_{Tb} cos(\omega_{IF}t) + V_{TL} cos(\omega_{IF}t) + n_1 cos(\omega_{IF}t) \right] \quad \text{(C.26)}$$

Considering now the V_6 output:

$$V_6 = -\frac{Kg_2}{\sqrt{2}} \left[V_{Tb} \left(\omega_{LO} + \omega_{IF} \right) t - V_{TL} \left(\omega_{LO} + \omega_{IF} \right) t + n_2 \left(\omega_{LO} + \omega_{IF} \right) t \right] \times V_{Tb} \left(\omega_{LO} t + \phi \right)$$
(C.27)

Using $cos\alpha cos\beta = \frac{cos(\alpha+\beta)+cos(\alpha-\beta)}{2}$,

$$V_6 = -\frac{KV_{LO}g_2}{\sqrt{2}} \left[V_{Tb} \left[cos((\omega_{LO} + \omega_{IF} + \omega_{LO})t + \phi) + cos((\omega_{LO} + \omega_{IF} - \omega_{LO})t + \phi) \right] \right.$$
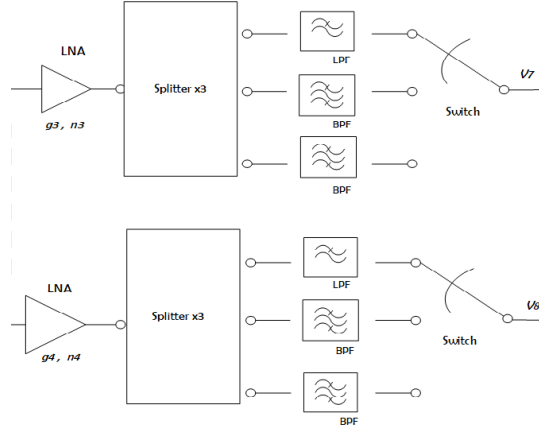
FIGURE C.5. Scheme of the analog backend stage of the radiometer.

$$-V_{TL}\left[cos((\omega_{LO}+\omega_{IF}+\omega_{LO})t+\phi)+cos((\omega_{LO}+\omega_{IF}-\omega_{LO})t+\phi)\right]$$

$$+n_2\left[cos((\omega_{LO}+\omega_{IF}+\omega_{LO})t+\phi)+cos((\omega_{LO}+\omega_{IF}-\omega_{LO})t+\phi)\right]](C.28)$$

Then,

$$V_6=-\frac{KV_{LO}g_2}{\sqrt{2}}\left[V_{Tb}\left[cos((2\omega_{LO}+\omega_{IF})t+\phi)+cos((\omega_{IF}t)+\phi)\right]\right.$$

$$-V_{TL}\left[cos((2\omega_{LO}+\omega_{IF})t+\phi)+cos((\omega_{IF}t)+\phi)\right]$$

$$+n_2\left[cos((2\omega_{LO}+\omega_{IF})t+\phi)+cos((\omega_{IF}t)+\phi)\right]](C.29)$$

Similarly, it is possible to select the frequencies directly related to ω_{IF}, leaving:

$$V_6=-\frac{KV_{LO}g_2}{2\sqrt{2}}\left[V_{Tb}cos((\omega_{IF}t)+\phi)-V_{TL}cos((\omega_{IF}t)+\phi)+n_2cos((\omega_{IF}t)+\phi)\right] \quad (C.30)$$

For $\phi=0°$, V_6 is:

$$V_6^{0°}=-\frac{KV_{LO}g_1}{\sqrt{2}}\left[V_{Tb}cos(\omega_{IF}t)-V_{TL}cos(\omega_{IF}t)+n_1cos(\omega_{IF}t)\right] \quad (C.31)$$

For the analog backend, figure (C.5), consider the IF stage amplifier and the filter selected by the switch as one block. Taking into account the amplifier gain of each branch g_3 and g_4, in addition to the noise of both branches,

$$n_3=n_3cos(\omega_{LO}+\omega_{IF})t \quad (C.32)$$

$$n_4=n_4cos(\omega_{LO}+\omega_{IF})t \quad (C.33)$$
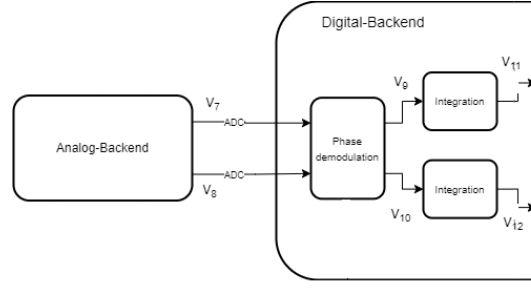
FIGURE C.6. First modules of the 22 GHz radiometer digital backend scheme. Phase demodulation and integration modules

The inputs to this block are V_5 and V_6, and the outputs are V_7 and V_8, respectively,

$$V_7 = g_3(V_5 + n_3) \tag{C.34}$$

$$V_8 = g_4(V_6 + n_4) \tag{C.35}$$

$$V_7 = \frac{KV_{LO}g_1g_3}{\sqrt{2}} \left[V_{Tb}cos(\omega_{IF}t) + V_{TL}cos(\omega_{IF}t) + n_1cos(\omega_{IF}t) + n_3cos(\omega_{IF}t) \right] \tag{C.36}$$

$$V_8 = \frac{KV_{LO}g_2g_4}{\sqrt{2}} \left[V_{Tb}cos(\omega_{IF}t) - V_{TL}cos(\omega_{IF}t) + n_1cos(\omega_{IF}t) + n_4cos(\omega_{IF}t) \right] \tag{C.37}$$

V_7 and V_8 are the respective inputs to the digital backend.

$$V_7 = \frac{KV_{LO}g_1g_3}{\sqrt{2}} \left[V_{Tb}cos(\omega_{IF}t) + V_{TL}cos(\omega_{IF}t) + (n_1 + n_3)cos(\omega_{IF}t) \right] \tag{C.38}$$

$$V_8 = -\frac{KV_{LO}g_2g_4}{\sqrt{2}} \left[V_{Tb}cos(\omega_{IF}t) - V_{TL}cos(\omega_{IF}t) + (n_2 + n_4)cos(\omega_{IF}t) \right] \tag{C.39}$$

C.2 Mathematical analysis: digital backend

V_7 and V_8 are the respective inputs to the digital backend, to the ADC. In the first phase there is the phase demodulation module of the inputs delivered by the ADC, which consists of the change of sign depending on the state of the phase shifter to mitigate the noise $1/f$, for which a change of sign is made sign. In addition, between state changes, a variable latency period is considered, where the signal stabilizes after the state change.

Then, in the integration modules, the input data is accumulated in a bank, read one by one, then averaged, and taken to the output, figure (C.6).

$$V_{11} = \frac{1}{N} \sum \frac{KV_{LO}g_1g_3}{\sqrt{2}} \left[V_{Tb}cos(\omega_{IF}t) + V_{TL}cos(\omega_{IF}t) + (n_1 + n_3)cos(\omega_{IF}t) \right] \tag{C.40}$$

$$V_{12} = \frac{1}{N} \sum \frac{KV_{LO}g_2g_4}{\sqrt{2}} \left[V_{Tb}cos(\omega_{IF}t) - V_{TL}cos(\omega_{IF}t) + (n_2 + n_4)cos(\omega_{IF}t) \right] \tag{C.41}$$
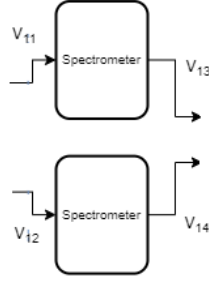
FIGURE C.7. Input and output voltages of the spectrometers in the digital stage.

The input signals in each spectrometer are V_{11} and V_{12}, figure (C.7), there the signals change from the time domain to the frequency domain by means of the Fourier transform.

$$\widetilde{f}(\omega) = \int_{-\infty}^{\infty} f(T)e^{-j\omega t}dt \tag{C.42}$$

This transform is applied to the voltage equations V_{11} and V_{12} whose outputs are:

$$V_{13} = \frac{\pi K V_{LO} g_1 g_3}{\sqrt{2}} \left[V_{Tb}\left(\delta_{IF}t\right) + V_{TL}\left(\delta_{IF}t\right) + \left(n_1 + n_3\right)\left(\delta_{IF}t\right) \right] \tag{C.43}$$

$$V_{14} = \frac{\pi K V_{LO} g_2 g_4}{\sqrt{2}} \left[V_{Tb}\left(\delta_{IF}t\right) - V_{TL}\left(\delta_{IF}t\right) + \left(n_2 + n_4\right)\left(\delta_{IF}t\right) \right] \tag{C.44}$$

The signals coming out of the analog part are digitized separately and then arithmetically recombined using calibrated weighting coefficients, which are used to implement an ideal hybrid and to compensate for phase and magnitude errors in analog components such as RF hybrid, mixers, and any other components.

The calibration of the digital backend determines the constants that represent a digital hybrid that reduces the total imbalances. This is done by injecting a test tone to measure the relative amplitude and phase of the two branches, and then determining the gain ratio or amplitude χ, and the phase terms $(\varphi_{IF} \pm \varphi_{LO})$ for all frequencies in the IF passband. The gain ratio is the square root of the time-averaged signal powers in both branches,

$$\chi = \sqrt{\frac{\left(V_{Tb}\overline{V_{Tb}}\right)}{\left(V_{TL}\overline{V_{TL}}\right)}} \tag{C.45}$$

where V_{Tb} and V_{TL} are the voltage amplitudes, and the phase term $(\varphi_{IF} - \varphi_{LO})$ can be determined from the cross product of V_{Tb} and V_{TL}:

$$\varphi = \varphi_{IF} - \varphi_{LO} = \tan^{-1}\left[\frac{Im\left(V_{Tb}\overline{V_{Tb}}\right)}{Re\left(V_{TL}\overline{V_{TL}}\right)}\right] \tag{C.46}$$

In equation (C.46) φ_{IF} and φ_{LO} are the phase imbalances at IF and LO, φ_{LO} represents the phase imbalance at the ADC input due to RF and LO components, and φ_{IF} is the relative phase mismatch of the signal due to analog components after the mixers.
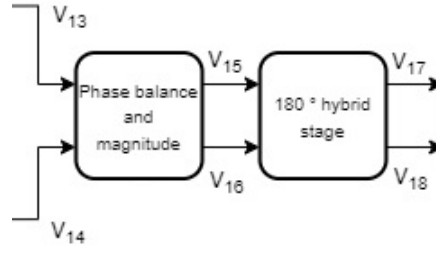
FIGURE C.8. Input and output voltages of the phase and magnitude balance and 180° digital hybrid, to obtain the pseudo-correlation equations

The signals V_{13} and V_{14} are out of phase with each other so that there is a compensation per channel or a balance in phase and magnitude, these constants or modification factors, equations (C.45) and (C.46), must be included in a branch, in such a way that they can reach the hybrid stage with the same magnitude and 180° phase.

$$V_{15} = \frac{\pi K V_{LO} g_1 g_3}{\sqrt{2}} \left[V_{Tb} \left(\delta_{IF} t \right) + V_{TL} \left(\delta_{IF} t \right) + \left(n_1 + n_3 \right) \left(\delta_{IF} t \right) \right] \tag{C.47}$$

$$V_{16} = \frac{\pi K V_{LO} g_1 g_3}{\sqrt{2}} \chi cos\varphi \left[V_{Tb} \left(\delta_{IF} t \right) - V_{TL} \left(\delta_{IF} t \right) + \left(n_1 + n_3 \right) \left(\delta_{IF} t \right) \right] \tag{C.48}$$

The passage of the signals through the ideal digital hybrid of 180° reflects in one output port the sum of the two inputs, while the other port contains the difference between them, expressed by a matrix that implies the phase change, that is the algebraic sum between both signals.

The modification factors $Xcos\varphi$ compensate for the inequalities in magnitude and phase of the signals coming from the analog stage, therefore the signals would already be compensated. Figure (C.8) shows the phase and magnitude balance modules and the 180° digital hybrid by which the signal undergoes these changes.

Considering the digital hybrid in an ideal and balanced way, that is, when $\triangle \phi = 0$, the output voltages in an ideal case, V_{17} and V_{18}:

$$V_{17} = \frac{-j}{\sqrt{2}} \left(V_{15} + V_{16} \right) \tag{C.49}$$

$$V_{18} = \frac{-j}{\sqrt{2}} \left(V_{15} - V_{16} \right) \tag{C.50}$$

Gain differences are considered as an imbalance, $G = \frac{|g_1|}{|g_2|}$, such that $\mid g_1 \mid = \mid g_2 \mid$ and therefore $G = 1$; furthermore $k = \frac{\pi K V_{LO} G}{2}$, and N as the representation of noise figures.

In the output of the digital hybrid it is possible to obtain values for the pseudo-correlation for both $\phi = 0°$ and $\phi = 180$:

For $\phi = 0°$,

$$V_{17} = 2GkV_{Tb} + N \qquad\qquad (C.51)$$

$$V_{18} = 2GkV_{TL} + N \qquad\qquad (C.52)$$

For $\phi = 180°$,

$$V_{17} = -2GkV_{Tb} + N \qquad\qquad (C.53)$$

$$V_{18} = -2GkV_{TL} + N \qquad\qquad (C.54)$$

Appendix D

AWR software operation

AWR VSS software is a system level simulator, an automation tool for a high-frequency electronic design that accelerates the development of electronic products with RF (radio frequency) recognition, has an intuitive interface and design assistance functions for knowing the theoretical performance of a receiver. Can design a system-level simulation model at the component level, such as amplifiers, mixers, or encoders (figure D.1).


```
AMP_B2
ID=A1
GAIN=32
P1DB=15
IP3=
IP2=
MEASREF=
OSAT=
OSATTYP=Total Power, dBm
NF=1.5
NOISE=RF Budget + Time Domain
RFIFRQ=
```
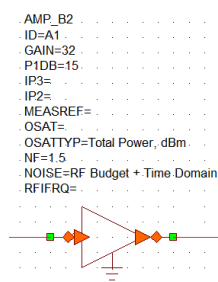
FIGURE D.1. Schematic of a block in the AWR system, in this case an amplifier is exemplified. Note the diagram and the parameters that can be included..

AWR VSS software models the effects of a system upon one or more signals which can be digital data, modulated analog signals, continuous wave (CW) tones, or other types. AWR VSS software designs start with a system diagram and are composed of interconnected blocks representing individual components in a design. The connections between the blocks describe the flow of data through the system.

Blocks typically have one or more ports, which serve as the connection points to other blocks. The connection point between ports is called a node.

There are two types of ports: input ports and output ports. Input ports are the data entry point into a block and receive data from an output port of another block. When a simulation runs, data flows from the output port of one block to one or more input ports of other blocks connected to the output port. When a block receives data, it applies its behavior to the data and generates an appropriate output.

At least one block must be a source block, which is a block that generates a signal without requiring input from another block, figure (D.2).
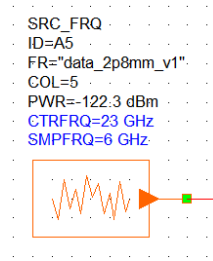
FIGURE D.2. Schematic of a source block in the AWR system, in this case a frequency response source is exemplified, which generates a repetitive waveform in the time domain from a frequency response. Note the diagram and the parameters that can be included.

To perform some of the measurements, a 'meter' block with an input port connected to the system can also be used. The most commonly used meter is the Test Point block TP which lets you monitor any signal, figure (D.3).
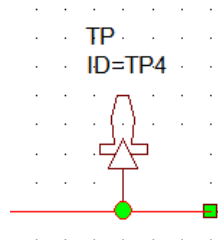
FIGURE D.3. Schematic of a TP meter block in the AWR system, which is used to take measurements of the outputs of the blocks of the system diagram.

AWR VSS software supports three types of simulations: Time Domain simulations, RF Budget Analysis simulations, and RF Inspector simulations.

The RF Budget Analysis measurements, in the System > RF Budget Analysis measurement category, invoke the RF Budget Analysis (RFB) simulator. These measurements include cascaded noise figure and gain.

The RF Inspector measurements, in the System > RF Inspector measurement category, invoke the RF Inspector (RFI) simulator.

Both RFB and RFI simulations are generally restricted to the RF components of a system design. Both simulators operate in the frequency domain and assume steady state behavior. However, Time Domain simulations are started and then run until stopped, RFB and RFI simulations occur in one step. This allows efficient use of the optimization and yield analysis features of the AWR Design Environment software.

RFB and RFI simulations are run when the Analyze command is chosen and are only run if the system diagram has been modified. In addition, they are also run when the Run/Stop System Simulators command is chosen if the system diagram has been modified.
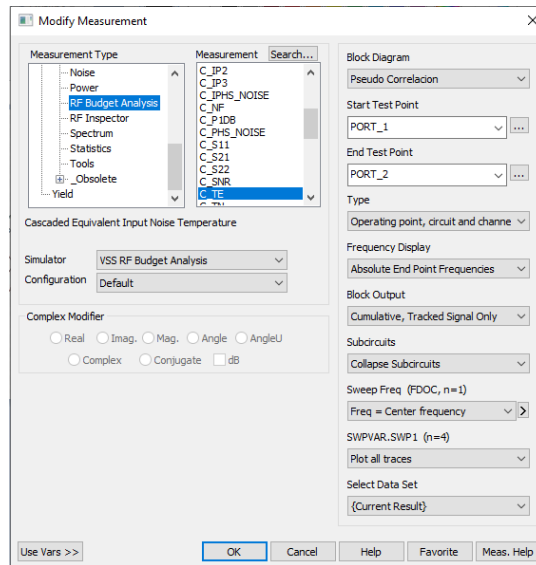
FIGURE D.4. Image of the AWR VSS software window, where the parameters are entered and the simulation mode is selected.

In a Time Domain simulation, data is represented as a stream of samples, with each sample representing the value of the signal at a specific point in time. The time difference between each sequential sample in a signal is called the time step.

In AWR VSS software, the time step is fixed during the main simulation. However, different signals may have different time steps. VSS Time Domain simulations are started by choosing Simulate > Run System Simulators. Then, a simulation runs until you pause or stop it, or it completes processing the required number of samples.

On the other hand, it is often desirable to obtain simulation results for several design parameter values. Therefore, when one or more design parameters are modified during a simulation, the simulation is swept. Each sweep consists of simulating a specific set of design parameter values. The design parameters are called the swept variables. Figure (D.4) shows an example of a window where the parameters to be measured are placed.

Appendix E

Reverse problem methodology: Retrievals

Remote sensing is a tool used to recover the physical properties of objects in the atmosphere by measuring their electromagnetic emission, absorption, or dispersion characteristics through remotely located sensors.

A wave in the microwave band interacts strongly with atmospheric particles such as water vapor, and this interaction allows the propagated wave to be used as a diagnostic tool to probe the lower atmospheric structure.

Water vapor is the most critical minor constituent that provides information for the GCM (Global Circulation Model), but it is a difficult atmospheric component to analyze. Still, the most promising technology available to perform its measurement is passive microwave radiometry, and the 22.235 GHz line is suitable primarily for ground surveys and monitoring.

Therefore, the next chapter will detail the inversion theory widely used to recover atmospheric parameters. The standard reference for this is C.D. Rodgers, 2000 "Reverse Methods for Atmospheric Soundings: Theory and Practice" Rodgers (2000), a copy can be purchased online from The World Meteorological Organization, via their website: https://library.wmo.int. Therefore, this appendix is more than anything a condensation of the most important aspects that must be taken into account for the recoveries of atmospheric parameters. In addition, at the end we find an introduction to the software that you will use after the MA, for a greater depth in the recoveries, such as ARTS and QPack.

E.1   Forward model

The inverse problem consists of configuring and solving a set of simultaneous linear or non-linear equations, in the presence of an experimental error in any of the parameters (the "measures"). The measures assembled in a vector, y, are considered, and the measure vector with its unknowns in a state vector x.

A state vector, x, can represent the quantities to be retrieval, with n elements $x_1, x_2, ...x_n$, and will often represent a profile of some given quantity over a finite number of levels. The

quantities measured to recover x can be represented by the measurement vector y, with m elements, $y_1, y_2, ... y_m$. This vector must include all measured quantities that are functions of the state vector x. The vector denotes the random error or measurement noise. The inverse problem is about finding the best representation of the required parameter given the measurements made, along with any appropriate a priori information that may be available about the system and the measurement device.

For each state vector, there is a corresponding ideal measurement vector, y_i, determined by the physics of the measurement. Can be described physics using a model $F(x)$, which is a vector-valued function of the state, and with its experimental error,

$$y = F(x + \epsilon) \tag{E.1}$$

To build an advanced model, we must, of course, know how the measuring device works and understand how the quantity measured is related to the quantity that is actually desired. In most inverse problems, the quantities that must be recovered are continuous functions, whereas the measurements are always of discrete quantities. This is simply treated by replacing the truly continuous state function, corresponding to an infinite number of variables, with a representation of a finite number of parameters and discretizing the problem before attempting to solve it, using vector and matrix algebra.

E.2   Weighting function

To examine the information content of measurement, it is convenient to consider a linear problem. A linearization of the direct model on some reference state x_0, provided that $F(x)$ is linear within the error limits of the retrieval,

$$y - F(x_0) = \frac{\partial F(x)}{\partial x}(x - x_0) + \epsilon = K(x - x_0) + \epsilon \tag{E.2}$$

defines the weighting function matrix K, $m x n$, not necessarily square, in which each element is the partial derivative of a model element forward concerning a state vector element, that is, $k_{ij} = \partial F_i(x) / \partial x_j$.

If $m < n$, the equations are described as under-found (or not well defined) because there are fewer measurements than unknowns. Similarly, if $m > n$ the equations are described as over-determined Rodgers (2000); Blackwell and Chen (2009).

The term weight function takes the form of a weighted average of the vertical profile of the Planck function. It can also be called Jacobian (it is a matrix of derivatives).

E.3   Vector spaces

The state space (or model space) is a vector space of dimension n, within which a point represents each conceivable state, or equivalently by a vector from the origin to the point

(considering that the origin is at x_0). The measurement space (or data space) is a vector space of dimension m, in which each conceivable measure is equally represented by a point or a vector (with the origin at $F(x_0)$).

The act of measurement is then equivalent to a mapping from the state space to the measurement space, and the inverse problem is to find an appropriate inverse mapping from the measurement space to the state space Rodgers (2000), and the weight function of the matrix K represents direct mapping.

Each row of K, of dimension n, can be considered vector k_i in state space, even though it is not a state, it corresponds to i-th measure y_i (value of i-th coordinate of the measurement space) for a given state vector x, is the vector product of x and k_i, plus the measurement error. Therefore, each of the rows of K corresponds to a coordinate in the measurement space, providing the mapping from the state space to the measurement space.
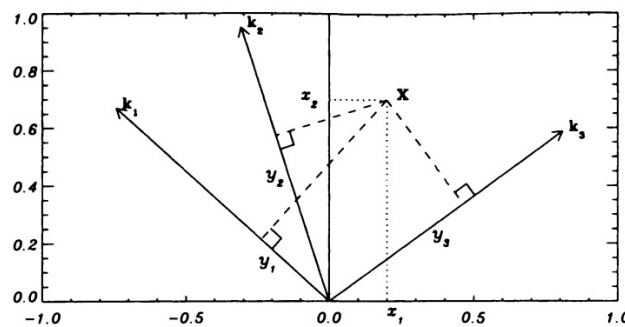
FIGURE E.1. A state space in two dimensions and a space of measures in three dimensions. Source: Rodgers (2000).

Figure (E.1), illustrates a state space in two dimensions, in which the point x represents the state, with the components x_1 and x_2. Three measurements are made, with weighting functions corresponding to the three vectors k_1, k_2, and k_3, chosen to be unit vectors and, therefore, unit length. The measures y_1, y_2, and y_3 correspond to the orthogonal projections of x in the k's, that is, the distances from the origin to the intersections of the perpendiculars with the vectors k. These three numbers define a point in three-dimensional measurement space.

Figure (E.1) also illustrates that such measurement is over-determined. Given only the weighting function vectors and the measurements, the state can be found from the intersections of the perpendiculars of the weighting function vectors. However, only two are needed to determine x, the third is superfluous, and it could be inconsistent with the other two if the measurement error prevents the three perpendiculars from intersecting at one point.

In the case of a linear problem with arbitrary numbers of dimensions in the absence of error, the problem boils down to the exact solution of linear simultaneous equations,

$$y = kx \tag{E.3}$$

which allows investigating what information can be extracted from the y measurements about the state x, mainly when there is no solution or a unique solution. Equation (E.1) will be replaced by (E.3), where y is a vector of quantities to be measured, and x is the unknown profile. The matrix K is a discrete version of the weighting functions.

Considering a subspace of the state of spaces, the vectors m of the weighting function k_i will encompass a subspace of the state space with a dimension no major than m, and maybe less than m if the vectors are not linearly independent. The dimension of this subspace is known as the rank of the matrix K, denoted by p, and is equal to the number of linearly independent rows (or columns). This subspace, encompassed by the vectors that make up the rows of K, is called the row space or range of K^T and may or may not span the entire state space if $m > n$, more measurements than unknowns, the range cannot be major than n, which may be less. K also has a column space of dimension p, a subspace of the measurement space.

It is possible to imagine an orthogonal coordinate system or a basis for the state space with p orthogonal basis vectors (coordinates) in the row space and external $n - p$ basis vectors orthogonal to the row space orthogonal to all weighting function vectors. Only the state vector components in the row space will contribute to the measurement vector due all other components are orthogonal; they will give a zero contribution to the measurement; that is, they are not measurable. This undetermined part of the state space is called the null space of K.

The problem will be undetermined if $p < n$, that is if there is a null space. In this case, the solution is not unique because there are components of the state that are not determined by the measurements and that, therefore, could take any value. Their sizes (whether they are taken as zero or something else) must be determined from other arguments, or they must be explicitly ignored, i.e., a retrieved state has components in null space, its values cannot have been obtained from the measures.

Considering only the components of the state vector in the row space, if $m > p$ and there are more measurements than the range of K, or if $m = p$, it is possible that a problem is simultaneously over-determined (in the space of the row) and is not determined (if there is a null space), this is a condition called mixed determined. It is even possible that there are more measures than unknowns, $m > n$. Moreover, a problem is not determined correctly when $p < n$. A problem is well determined only if $m = n = p$.

If the problem is well determined, a unique solution can be found by solving a set of equations pxp. If the problem is over-determined in the row space and there is no measurement error, then the measurements must be linearly related in the same way as the k_i-vectors or they are inconsistent, and there is no exact solution.

In summary, the measure represented by K provides p independent quantities or pieces of information with which the state can be described.
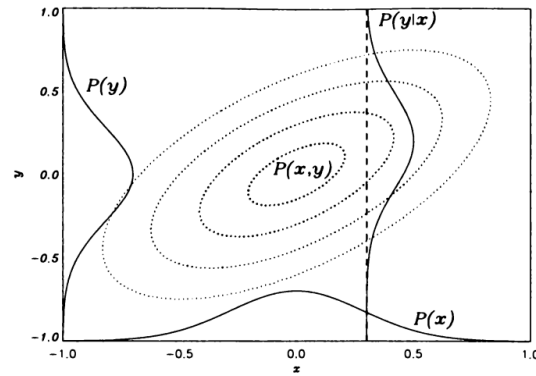
FIGURE E.2. Illustrating Bayes' theorem for a two-dimensional. The dotted ellipses represent the contours of the *pdf* $P(x,y)$ of two scalar random variables x and y. The dashed line is a cut through $P(x,y)$ at a given value of x, and the curve labeled $P(y|x)$ represents the *pdf* conditional of y given that value of x. The individual *pdf*s $P(x)$ and $P(y)$ are obtained by integrating $P(x,y)$ over the other variable. Source: Rodgers (2000).

E.4   Bayesian approach

A useful conceptual approach to the inverse problem in the presence of measurement error is the Bayesian view, a priori knowledge can be quantified as a probability density function (pdf), and measurement with experimental error can also be quantified as pdf. The Bayesian approach identifies a set of possible solutions, assigning a probability to each one.

The probability density functions that are important in the inverse problem are:

- $P(x)$: The a a priori pdf of state x, which describes what is known about the state before taking the measurement.

- $P(y)$: The a a priori pdf of the measurement, describing what is known about the measurement before it is performed.

- $P(x,y)$: The a a priori pdf articulation of x and y. Which means that $P(x,y)dxdy$ is the probability that x is in $(x, x + dx)$ and y is in $(y, y + dy)$.

- $P(y|x)$: The conditional pdf of y given x. Which means that it is the probability that y is in $(y, y + dy)$ when x has a given value.

- $P(x|y)$: The conditional pdf of x given y, which means that it is the probability that x will be found at $(x, x + dx)$ when y has a given value. This is the quantity that is of interest to solve the inverse problem Brasseur (2013).

Considering figure (E.2), shows that the conditional probabilities are related by:

$$P\left(x|y\right) = P\left(x|y\right)P\left(y\right) = P\left(y|x\right)P\left(x\right) \tag{E.4}$$

and following Bayes' theorem,

$$P\left(x|y\right) = \frac{P\left(y|x\right) P\left(x\right)}{P\left(y\right)} \tag{E.5}$$

The left side of Eq. (E.5), $P(x|y)$, is the later pdf of the state in which the measurement is provided. $P(x)$ is the updating of the a a priori knowledge of the state with the measurement. $P(y|x)$ describes the knowledge of y obtained if the state were x. Explicitly, only the direct model and the statistical description of the measurement error are required. The only remaining quantity required is the denominator, $P(y)$.

The conceptual approach to the inverse problem implies:

- Before taking a measurement, it is possible to have a a priori knowledge expressed as a previous pdf.

- The measurement process is expressed as a forward model that maps the state space into the measurement space.

- Bayes' theorem provides a formalism to reverse this mapping and calculate a later pdf by updating the previous pdf with a pdf measure.

The Bayesian approach is general, that is, it encompasses all inverse methods by providing a way to characterize the class of possible solutions, considering all possible states, and assigning a probability density to each one Rodgers (2000).

E.4.1   The Linear problem with Gaussian statistics

It is considered a linear problem in which all pdf files are Gaussian. A linear problem is one for which the direct model is linear:

$$y = F(x) + \epsilon = Kx + \epsilon \tag{E.6}$$

A pdf is the n-dimensional Gaussian distribution. A random and distributed vector y with a mean $\overline{y}$ and a covariance S_y has a given pdf,

$$- lnP(x) = \frac{1}{2}(y - \overline{y})^T S_z^{-1}(y - \overline{y}) + const \tag{E.7}$$

Gaussian statistics are usually a good approximation of errors in actual measurements, so $P(y|x)$ is expressed as:

$$- 2lnP(y|x) = (y - Kx)^T S_\epsilon^{-1}(y - Kx) + const \tag{E.8}$$

where S_ϵ is the covariance of the measurement error. Describing the a priori of x by a Gaussian pdf:

$$- 2lnP(x) = (x - x_a)^T S_a^{-1}(x - x_a) + const \tag{E.9}$$

where x_a is the a priori value of x, and S_a is the associated covariance matrix, that describes the precision with which the state vector is known before measurement,

$$S_a = \epsilon \left\{ (x - x_a)(x - x_a)^T \right\} \tag{E.10}$$

Substituting equations (E.8) and (E.9) in equation (E.5) is obtained for the posterior pdf:

$$-2lnP(x|y) = (y - Kx)^T S_\epsilon^{-1}(y - Kx) + (x - x_a)^T S_a^{-1}(x - x_a) + const \tag{E.11}$$

This quadratic form in x that describes how accurately the state is known after measurement.

Instead of the generality of a pdf of x, can be do some estimate of state $\hat{x}$, using a function of the conditional probability density $P(x|y)$,

$$\hat{x} = \int P(x|y)x dx \tag{E.12}$$

it is possible to write it:

$$-2lnP(x|y) = (x - \hat{x})^T \hat{S}^{-1}(x - \hat{x}) + const \tag{E.13}$$

By setting the quadratic terms equal in x, an expression for the covariance matrix of the subsequent pdf can be found:

$$\hat{S}^{-1} = K^T S_\epsilon^{-1} K + S_a^{-1} \tag{E.14}$$

The covariance matrix $\hat{S}$ quantitatively indicates the precision of the recovered atmospheric parameters, for example, the concentration recovered in each layer and the correlation of errors between different layers.

By equating the linear terms in x or x^T and substituting $\hat{S}^{-1}$ for the expected value of the pdf:

$$\hat{x} = (K^T S_\epsilon^{-1} K + S_a^{-1})^{-1}(K^T S_\epsilon^{-1} y + S_a^{-1} x_a) \tag{E.15}$$

If the linear equation (E.6) has some exact solution, the expected value can be written as:

$$\hat{x} = x_a + S_a K^T (K S_a K^T + S_\epsilon)^{-1}(y - Kx_a) \tag{E.16}$$

The Bayesian solution to the inverse problem is not x, but the Gaussian pdf $P(x|y)$, of which $\hat{x}$ is the expected value and $\hat{S}$ is the covariance.

It should be noted that $\hat{x}$ is a linear function of the a priori expected value and the measurement, as might be expected for a linear problem, and the inverse covariance matrix $\hat{S}^{-1}$ is
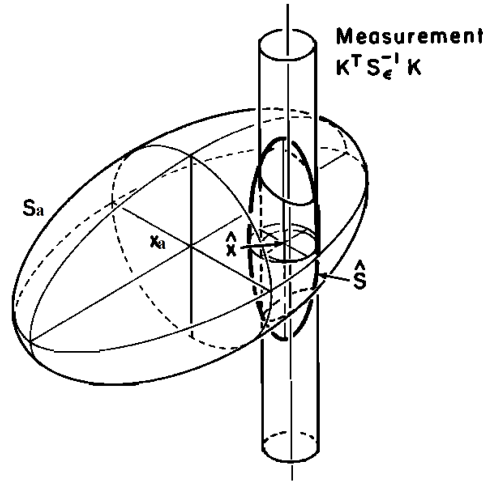
FIGURE E.3. An illustration of the relationship between the a priori covariance, the measurement covariance mapped into profile space, and the solution covariancc. Source: Rodgers (1976).

a linear function of the prior inverse covariance matrix y the inverse measurement error covariance. Equation (E.14) is known as Fisher information matrices.

Figure (E.3) provides a geometric illustration of the relationship between the prior covariance, the measurement, and the posterior covariance when the state space has three dimensions, and the measurement space has two. The large ellipsoid centered on x_a represents an a priori covariance contour, which describes the region of space within which the state is likely to lie. The cylinder represents the region in which the states coherent with the measurement could be, where the ellipsoid axis is the set of states that correspond exactly to the measurement, and the cylinder contains an experimental error. The axis direction represents the null space. The weighting functions for the two measurement items are orthogonal to the axis. The small ellipsoid describes the region consistent with the previous information and the measurement. The center of $\widehat{x}$ is not on the axis of the cylinder; that is, the expected value does not exactly fit the measure Rodgers (2000, 1976).

E.5 Analysis and characterization of errors

Retrieval is characterized by explicitly evaluating the relationship between the recovered profile, the proper atmosphere, and the various sources of error.

The total error has components due to systematic errors in the direct model and the inverse method, measurement noise in the instrument, and components of the accurate profile that cannot be reproduced in the retrieval profile Brasseur (2013); Rodgers (1976). Most error terms appear as covariance matrices rather than simple error variations. The measure y is formally a function of some unknown state x:

$$y = f(x, b) + \epsilon \qquad (E.17)$$

where y is the measurement vector of length m, x is the state vector of length n, f is the direct function that describes the physics of the measurement, b is a set of parameters of the direct

function that are considered known, and ϵ is a random measurement error with covariance S_ϵ.

The retrieval state $\widehat{x}$ is conceptually a function of the form,

$$\widehat{x} = R(y, \widehat{b}, x_a, c) \tag{E.18}$$

where R represents the retrieval method, $\widehat{b}$ is the estimate of the direct function b, c represents any parameter used in the inverse method (such as the iteration convergence limit) that does not affect the measurement, and x_a is the estimate of state a priori. Substituting (E.18) in (E.17):

$$\widehat{x} = R(f(x, b) + \epsilon, \widehat{b}, x_a, c) \tag{E.19}$$

Equation (E.19) can be considered as the transfer function of the measurement and recovery system as a whole.

The direct function f describes the actual physics of the measurement, which often needs to be approximated by a forward model F,

$$f(x, b) \simeq F(x, b) \tag{E.20}$$

The forward model should contain all the physics of the measurement, including the instrumental characteristics, usually, the b-parameters that have experimental errors (such as data from spectral lines or cross-sections) but are not a target for recovery. There may also be b' parameters of the forward function that are ignored in the forward model. This relationship is expressed as:

$$f(x, b, b') = F(x, b) + \Delta f(x, b, b') \tag{E.21}$$

The retrieved state vector can now be written:

$$\widehat{x} = R(F(x, b) + \Delta f(x, b, b') + \epsilon, \widehat{b}, x_a, c) \tag{E.22}$$

Linearizing the forward model F on some reference state, which can be the a priori state $x = x_a, b = \widehat{b}$,

$$\widehat{x} = R(F(x_a, \widehat{b}) + \frac{\partial F}{\partial x}(x - x_a) + \frac{\partial F}{\partial b}(b - \widehat{b}) + \Delta f(x, b, b') + \epsilon, \widehat{b}, x_a, c) \tag{E.23}$$

where the matrix $K_x = \partial F / \partial x$ is the sensitivity of the direct model to the state, whose rows are the weighting functions, and $K_b = \partial F / \partial b$ is the sensitivity of the direct model to the parameters of the direct model.

By linearizing the recovery method R to its first argument,

$$\widehat{x} = R(F(x_a, \widehat{b}), \widehat{b}, x_a) + \frac{\partial R}{\partial y}(K_x(x - x_a) + K_b(b - b') + \Delta f(x, b, b') + \epsilon) \tag{E.24}$$

The matrix $\frac{\partial R}{\partial y} = G_y$ is the sensitivity of the retrieval to the measurement, the *contribution function matrix*.

Doing the substitution and separating the equation into components:

$$\hat{x} - x = R(F(x_a, \widehat{b}), \widehat{b}, x_a, c)...bias$$
$$+A(x - x_a)...smoothing$$
$$+G_y \epsilon_y...retrieval \ error$$

where

$$A = G_y K_x = \frac{\partial \hat{x}}{\partial x} \tag{E.25}$$

is the *averaged kernel matrix*, which characterizes the sensitivity of the retrieval to the real state, and ϵ_y is the total error in the measurement about the model ahead,

$$\epsilon_y = K_b(b - b') + \Delta f(x, b, b') + \epsilon \tag{E.26}$$

The output of the retrieved state from the a priori can be considered as a smoothed version of the same output from the true state, with smoothing functions given by the rows of matrix A, when averaging kernels, plus error terms:

$$\hat{x} = X_a + A(x - x_a) + G_y \epsilon_y = (I - A)x_a + A_x + G_y \epsilon_y \tag{E.27}$$

The columns of matrix A can be considered as the response of the measurement and recovery to the disturbance functions. Retrieval is an estimate of a smoothed state instead of the true state, or retrieval is also considered an estimate of the true state. There is an additional term representing the smoothing error in the latter case.

If the state represents a profile, for example, of gas concentration or temperature, the average kernel is a smoothing function with a width and an area. The width is a measure of the resolution of the observing system, and the area (usually between zero and unity) is a rough measure of the amount of information about the actual profile that appears in the retrieval.

Considering the remaining parameters x_a and c in equation (E.19), the bias term must be equal to zero in the linearized case for reasonable retrieval methods, which implies that $\frac{\partial R}{\partial c} = 0$. It means that no other retrieval parameters other than a priori should affect the solution. The solution dependency of x_a is $\frac{\partial \hat{x}}{\partial x_a} = \frac{\partial R}{\partial x_a}$. Therefore, in linearized form, equation (6.27) gives:

$$\frac{\partial \hat{x}}{\partial x_a} = I - A \tag{E.28}$$

For error analysis, the different sources of errors must be identified. Assuming the bias is zero, the total error in the retrieval is:

$$\tilde{x} - x = (A - I)(x - x_a) + G_y \epsilon_y \tag{E.29}$$

where

$$\epsilon_y = K_b(b - \widehat{b}) + \Delta f(x, b, b') + \epsilon \tag{E.30}$$

Therefore, the sources of error can be divided as:

$$\widehat{x} - x = (A - I)(x - x_a)...smoothing\ \ error$$
$$+G_y K_b(b - \widehat{b})...model\ \ parameter\ \ error$$
$$+G_y \Delta f(x, b, b')...forward\ \ model\ \ error$$
$$+G_y \epsilon...retrieval\ \ noise$$

Some of the sources of error are easy to estimate, but others can be quite difficult. To estimate the actual smoothing error, the actual state must be known. To characterize the statistics of this error, its mean and covariance over some sets are needed. The covariance is:

$$S_s = (A - I)S_a(A - I)^T \tag{E.31}$$

where S_a is the covariance of a set of states on the a priori state. To estimate the smoothing error, it is necessary to know the climatological covariance matrix, and it is essential to have information on the real climatology.

If the b parameters of the forward model have been correctly estimated, their errors will be unbiased so that the mean error will be zero. However, the error can be systematic or random. The covariance matrix S_b is related to the parameters of model b. It is translated into a contribution to the retrieval error with covariance given by:

$$S_f = G_y K_b S_b K_b^T G_y^T \tag{E.32}$$

The error due to the modeling of the direct function is:

$$forward\ \ model\ \ error = G_y \Delta f = G_y(f(x, b, b') - F(x, b)) \tag{E.33}$$

This can be difficult to evaluate because it requires a model f that includes the correct physics. If F is simply a numerical approximation for efficiency reasons, it may not be too difficult, but if f is not known in detail or is so complex that no suitable model is feasible, then the modeling error may be difficult to estimate. Another difficulty arises because it must be evaluated in the true state and with the real value of b, but it is expected that its sensitivity to these quantities will not be significant. This is also a systematic error Brasseur (2013).

E.6   Estimation methods and models

The Bayesian description describes a set of possible solutions that are consistent with the available information, and allows assigning them a probability density function Brasseur (2013). However, for most purposes, it is desirable to select only one of the possible states as 'the solution' to the inverse problem and assign some error estimate to it rather than

providing the most general description. To select a method from the set as the 'optimal'
solution, we must choose what to optimize. Here are some possible approaches for optimal
inverse methods.

E.6.1   Minimum variance and maximum probability (ML) solution

Recall that the model ahead for the linear problem is $y = Kx + \epsilon$, with a constant weight-
ing function matrix *mxn*, *K*. A more general way would be $y - y_0 = K(x - x_0)$, where
(x_0, y_0) is a point of linearization. A linear problem has a linear solution, and we expect it to
be of the general form,

$$\widehat{x} = x_0 + Gy \tag{E.34}$$

where *G* is a constant *nxm* recovery gain matrix and x_0 is a constant displacement, and the
aim is to identify appropriate forms for *G* and x_0 for various types of optimality Brasseur
(2013).

In this case, it´s possible minimize the error in each element xi of $\widehat{x}$ separately, finding
the values of x_{0i} and the row g_i^T of the matrix *G* that minimize $\varepsilon\left\{(\widehat{x}_i - x_i)^2\right\}$:

$$\varepsilon\left\{(\widehat{x}_i - x_i)^2\right\} = \varepsilon\left\{(x_{0i} - x_i + g_i^T y)^2\right\} \tag{E.35}$$

Setting the derivative with respect to x_{0i} to zero

$$\varepsilon\left\{(x_{0i} - x_i + g_i^T y)^2\right\} = 0 \tag{E.36}$$

$$x_{0i} = \varepsilon\left\{x_i - g_i^T y)\right\} = x_{ai} - g_i^T y_a \tag{E.37}$$

where $y_a = Kx_a$ is the mean of the set of *y*. Setting the derivative of equation (E.35) concern-
ing to g_i to zero,

$$0 = \varepsilon\left\{(x_{0i} - x_i + g_i^T y)y^T\right\} = \varepsilon\left\{\left[x_{ai} - x_i + g_i^T(y - y_a)\right](y - y_a)\right\} \tag{E.38}$$

$$g_i^T = \varepsilon\left\{(x_i - x_{ai})(y - y_a)^T\right\}\left[\varepsilon(y - ya)(y - y_a)^T\right]^{-1} \tag{E.39}$$

Gathering the g_i's in the matrix *G* and substituting $\varepsilon = \left\{(y - ya)(y - y_a)^T\right\} = KS_aK^T + S_\epsilon, y_\epsilon\left\{(y - ya)(x - x_a)^T\right\} = S_aK^T$, it follows:

$$G = S_aK^T(KS_aK^T + S_\epsilon)^{-1} \tag{E.40}$$

then,

$$\widehat{x} = x_a + S_aK^T(KS_aK^T + S_\epsilon)^{-1}(y - Kx_a) \tag{E.41}$$

This is the same equation (6.16), but the *pdf* form has not been used here, only knowledge of x_a and S_a is required. The covariance of the recovery error is $\widehat{S} = \varepsilon\left\{(x - \widehat{x})(x - \widehat{x})^T\right\}$, we have

$$x - \widehat{x} = x - x_a - GK(x - x_a - G_\epsilon) \tag{E.42}$$

from which, assuming that the measurement error is not correlated with the state,

$$\widehat{S} = (I_n - GK)S_a(I_n - GK)^T + GS_\epsilon G^T \tag{E.43}$$

Substituting G from (6.40) reduces to

$$\widehat{S} = S_a - S_a K^T (KS_a - K^T + S_a)^1 + KS_a \tag{E.44}$$

which is also the same as for Gauss's solution.

The minimum variance solution is the conditional expected value, this is the case for an arbitrary *pdf*. Therefore, the solutions of minimum and maximum probability variance are equivalent when the expected value and the maximum probability are equal, if the probability density function is symmetric with respect to the expected value Rodgers (2000).

E.6.2   Best estimate of a function of the state vector

This estimate is taken to measure some function of the complete state vector, such as the total amount of a constituent in a column or the atmospheric thickness between two pressure levels.

In general, a linear function $h(x) = h_0 + h^T(x - x_0)$ of the underlying state vector, the total column of a constituent serving as the main example. Based on the Bayesian approach to recovery, the expected value of the function $h(x)$ is

$$\widehat{h} = \int P(x|y)\left[h_0 + h^T(x - x_0)\right]dx \tag{E.45}$$

As long as h does not depend on x, this can be rewritten as,

$$\widehat{h} = h_0 + h^T \int P(x|y)(x - x_0)dx \tag{E.46}$$

$$\widehat{h} = h_0 + h^T(x - x_0) \tag{E.47}$$

The error covariance of $\widehat{h}$ is $h^T\widehat{S}h$, its average kernel at $a^T = h^T A$, and its measurement error is $h^T S_m h$.

A common approach to retrieving a column quantity is choosing a fixed profile shape with a known column quantity and finding the scale factor that best matches the measured signal.

E.6.3 Resolution optimization

If there are not enough measurements and constraints to make the problem well-posed, or if those that exist do not reduce the solution error covariance $\widehat{S}$ sufficiently, then the original problem is not solvable, and we must look for other problems that are Rodgers (1976).

Backus and Gilbert (1970) studied the inverse problem of sounding solid earth using seismic waves to recover density as a function of depth to the core.

This is a case in which there is very little prior information available, so concepts such as the content of the information and the degrees of freedom of the signal are not helpful. Therefore, rather than trying to make the best estimate of the true density profile, they posed a somewhat different question: "What useful functions of the density profile can be derived from the measurements?" smoothing. Conrath (1972) applied the method to the atmospheric problem Conrath (1972).

In the case of the linear problem, all it can reasonably do with measurements is to take linear combinations of them. Every linear combination of measurements corresponds to a linear function of the unknown profile. However, most of the development of this method has been directed toward approximating a delta function, resulting in a singly peaked function with a width that may be specified by the user. The essence of the Backus-Gilbert method is to control the shape of this linear function so that it corresponds to some meaningful quantity.

The measures y_i, $i = 1...m$, are linear functions of the state $x(z)$, with weighting functions $K(z)$, making derivations with a continuous function

$$y_i = \int K_i(z')x(z')dz' + \epsilon_i \tag{E.48}$$

The retrieved profile $x(z)$ is a linear combination of the measures y_i expressed in terms of contribution functions $G_i(z)$:

$$\widehat{x}(z) = \sum_{i=1}^{m} G_i(z)y_i = \sum_{i=1}^{m} G_i(z)\left[\int K_i(z')x(z')dz' + \epsilon_i\right] = \int A(z,z')x(z')dz' + \sum_{i=1}^{m} G_i(z)\epsilon_i \tag{E.49}$$

where the kernel function averaging $A(z, z_0)$ corresponding to the recovered value at z is $\sum_{i=1}^{m} G_i(z)K_i(z')$.

The requirements for the Backus-Gilbert solution is that the averaged kernels must have a unit area,

$$\int A(z,z')dz' = 1 \tag{E.50}$$

Its propagation should be minimized around z, so that the retrieval resolution is as high as possible.

In order to approximate a delta function by a linear combination of weighting functions need some parameters that measure how good the approximation is, which may be minimized for the best fit. Such a quantity is the spread, which is defined as follows: The spread $S(x)$ of a function of height $A(z)$ about a height x is

$$s(z) = 12 \int \left[\sum_{i=1}^{m} G_i(z) K_i(z') \right]^2 (z - z')^2 dz' \qquad \text{(E.51)}$$

The normalizing factor 12 is included so that a boxcar function centered at x will have a spread equal to its width. the Backus-Gilbert method can be applied to cases where there is a priori information.

E.7 Information content of a measure

Fisher et al. (1921) established that a measure of information for a signal could be considered the degrees of freedom. The elements of the measurement vector are not independent functions of the state vector, nor are the errors statistically independent, making it difficult to understand the information content of measurement immediately.

To understand this and have the number of statistically independent pieces of information in measurement, it is helpful to transform the bases (coordinate systems) of the state space and the measurement space so that the measurements are independent. In general, the a priori and measurement covariance are not diagonal, but a simple transformation will diagonalize them.

If the measurement vector is transformed $\widetilde{y} = S_\epsilon^{-1/2} y$, and the state vector $\widetilde{x} = S_a^{-1/2} x$. The covariance matrix of the transformed a priori state, $\widetilde{S}_a$, and the error covariance of the transformed measure, $\widetilde{S}_\epsilon$ are now unit matrices. The model forward on this basis becomes:

$$\widetilde{y} = \widetilde{K}\widetilde{x} + \epsilon \qquad \text{(E.52)}$$

$\widetilde{K}$ is diagonalized by rotating $\widetilde{x}$ and $\widetilde{y}$ to new bases using the singular value decomposition of $\widetilde{K}$, $\widetilde{K} = U\Gamma V^T$. The transformed bases are defined by $x' = V^T \widetilde{x}$, $y' = U^T \widetilde{y}$, and $\epsilon' = U^T \widetilde{\epsilon}$. The forward model becomes:

$$y' = \Gamma x' + \epsilon' \qquad \text{(E.53)}$$

where the matrix weighting function Γ is diagonal and the prior and noise covariances are unit matrices. On this basis, the maximum probability solution is given by:

$$x' = (\Gamma^2 + I_n)^{-1}(\Gamma y' + x'_a) \qquad \text{(E.54)}$$

where I_n is a unit matrix of rank n. With each element of x' independently determined by the corresponding element of y',

$$x'_i = (\lambda_i y'_i + x'_{ai})/(\lambda_i^2 + 1) \tag{E.55}$$

In the linear Gaussian case, the information matrix is equal to the inverse covariance matrix, equation (E.14), indicating that the posterior information matrix is the sum of the previous and the measurement.

In equation (E.55), the elements for which $\lambda_i \gg 1$ or $(1 + \lambda_i^2)^{-1} \ll 1$ are well measured and the elements for which $\lambda_i \ll 1$ or $(1 + \lambda_i^2)^{-1} \simeq 1$ are badly measured. That means that the number of singular values $(1 + \lambda_i^2)^{-1} \leqslant 1$ can be considered the number of independent quantities measured. A valid statistical quantity that is closely related is the degrees of freedom of the signal (dfs),

$$dfs = \sum_i \lambda_i^2 (1 + \lambda_i^2)^{-1} \tag{E.56}$$

Elements that are well measured contribute almost 1 to the dfs, while elements that are poorly measured contribute little to the dfs.

Shannon (1948) defined that the information depends on the entropy of the probability density functions, which is closely related to the thermodynamic entropy, and therefore the content of the information is a scalar quantity. The information content of a measurement expresses the factor by which the knowledge of a quantity is improved when performing the measurement. Therefore, it is crucial to optimize the instrumental design.

The information content of a measure of x is the entropy change of the pdf of x over the measure. Entropy is defined as:

$$S\{P\} = -P(x)log(P(x)/M(x))dx \tag{E.57}$$

where $M(x)$ is a measurement function (null information state) that is taken as a constant.

The information content of measurement is the change in entropy between the probability density functions before and after the measurement,

$$H = S\{P(x)\} - S\{P(x|y)\} \tag{E.58}$$

In the case of a Gaussian distribution with covariance S, the entropy is $log|S|^{1/2}$ plus a constant. However, since the volume enclosed by some particular contour of $P(x)$ is proportional to $|S|^{1/2}$, the entropy is related to a 'volume of uncertainty in the state space. For a linear problem and Gaussian distributions,

$$H = \frac{1}{2}log|S_a| - \frac{1}{2}log|\widehat{S}| \tag{E.59}$$

The information content of measurement is the logarithm of the ratio of the uncertainty volumes before and after taking a measurement. The information content of a measurement can be defined qualitatively as the factor by which the knowledge of a quantity is improved when performing the measurement. In practice, the logarithm of the factor is used, with the base of the logarithm depending on the application and the determination of the dimension-less units. In information theory, it is often convenient to use base two when the units are "bits".

In the transformed system where everything is independent, equation (E.53), the Shannon information becomes:

$$H = S\left\{S'_a\right\} - S\left\{\widehat{S'}\right\} = \sum_i \frac{1}{2}log(1 + \lambda_i^2) \tag{E.60}$$

It is shown that there is a close relationship between the content of the information and the degrees of freedom of the signal. Each element of x'_i or y'_i independently contributes $\frac{1}{2}log(1 + \lambda_i^2)$ to the information content and $\lambda_i^2(1 + \lambda_i^2)^{-1}$ to the dfs.

An element with $\lambda_i = 0$ does not contribute anything to the information content and the dfs. The basis of the state space formed by vectors with zero singular values is described as the null space of K. Any component of the state in the null space is assigned to the origin in the measurement space, or equivalently, different states that cannot be distinguished by the measurement corresponding to points that are assigned to the same point in the measurement space.

The part of the metering space that can be seen covers the weighting functions. This observable space is defined by the vectors with $\lambda_i > 0$, but some observable components can in principle have contributions close to zero of the measurement and can be thought of as forming an "almost null space". Vectors with $\lambda_i \ll 1$ are in this almost null space.

E.8   Non-linear analysis

An inverse problem is generally solved by maximizing a cost function for which the forward model provides only one term. In general, a linear problem is one in which the cost function is quadratic in the state vector so that the equations to be solved are then linear. A non-quadratic term due to a prior constraint would result in a nonlinear problem even if the direct model were linear. Any non-Gaussian pdf as background information will lead to a nonlinear problem Rodgers (2000).

For non-linear problems, is considered the maximal a posteriori approach. The Bayesian solution for the linear problem, equation (E.11), can be directly modified for an inverse problem in which the direct model is a general function of the state, the measurement error is Gaussian, and there is a previous estimate with a Gaussian error:

$$-2lnP(x|y) = [y - F(x)]^T S_\epsilon^{-1} [y - F(x)] + [x - x_a]^T S_a^{-1} [x - x_a] + const \tag{E.61}$$

In the non-linear case, as in the linear case, the best estimate x and an error characteristic must be found that describes this pdf well enough for practical purposes. To find the state of maximum probability x the derivative of equation (E.61) is equated to zero:

$$\nabla_x \left\{ -2lnP(x|y) \right\} = \left[\nabla_x F(x) \right]^T S_\epsilon^{-1} \left[y - F(x) \right] + S_a^{-1} \left[x - x_a \right] + const \qquad \text{(E.62)}$$

The ∇_x gradient of a vector-valued function is a matrix-valued function. Letting $K(x) = \nabla_x F(x)$, this gives the following implicit equation for x:

$$- \widetilde{K}^T(\widehat{x}) S_\epsilon^{-1} \left[y - F(\widehat{x}) \right] + S_a^{-1}(\widehat{x} - x_a) = 0 \qquad \text{(E.63)}$$

This equation must be solved numerically. Newtonian iteration is a numerical method of finding the zero of the cost function gradient, that is, the first two terms of Eq. (E.61). For the general vector equation $g(x) = 0$, the iteration is analogous to Newton's method for the scalar case and can be written:

$$x_{i+1} = x_i \left[-\nabla_x g(x_i) \right]^{-1} g(x_i) \qquad \text{(E.64)}$$

where the inverse is an inverse matrix. Using the (E.63) for g, the matrix is:

$$\nabla_x g = S_a^{-1} + K^T S_\epsilon^{-1} K - \left[\nabla_x K^T \right] S_\epsilon^{-1} \left[y - F(x) \right] \qquad \text{(E.65)}$$

The function g is the derivative of the cost function (E.61), and $\nabla_x g$ is the second derivative, known as the *Hessian*. Consequently, this is also known as the inverse Hessian method. This last term is complicated because it is a vector whose elements are matrices, but the resulting product is small in the moderately linear case. If the term is ignored, the Gauss-Newton method is obtained, which is obtained by substituting equations (E.63) and (E.65) in the Newtonian iteration (E.64) and omitting this term,

$$x_{i+1} = x_i + \left(S_a^{-1} + K_i^T S_\epsilon^{-1} K_i \right)^{-1} \left[K_i^T S_\epsilon^{-1} (y - F(x_i)) - S_a^{-1}(x_i - x_a) \right] \qquad \text{(E.66)}$$

where $K_i = K_{xi}$. It is convenient to start the iteration with $x_0 = x_a$.

This method finds the one-step minimum for a cost function that is precisely quadratic at x, and will approach it if the function is nearly quadratic. For the non-linear least-squares problem, Levenberg (1944) proposed the iteration:

$$x_{i+1} = x_i + \left(KK^T + \gamma_i I \right)^{-1} K^T \left[y - F(x_i) \right] \qquad \text{(E.67)}$$

where γ is an empirically known constant chosen close to unity, and γ_i is chosen to minimize the cost function at each step. To $\gamma_i \to 0$, the step tends to Gauss-Newton. The cost function will initially decrease as γ_i decreases from infinity; therefore, an optimal value (possibly zero) maximizes the cost function.

Unfortunately, the computation required to choose γ_i is significant since $F(x)$ must be evaluated for every attempt at γ_i. Marquardt (1963) simplified the choice of γ_i; it is not

precisely looking for the best γ_i for each iteration but starting a new iteration step as soon as a value is found for which the cost function is reduced. An arbitrary initial value of γ is updated on each iteration.

The Marquardt strategy uses test χ^2, which tests whether a particular random vector belongs to a given Gaussian distribution. If a vector z is assumed to be a member of a Gaussian set with zero mean and covariance S_z, then the quantity considered is $\chi^2 = z^T S_z^{-1} z$ that is, twice the exponent in the Gaussian distribution.

Test χ^2 asks the question: "What fraction of members of the Gaussian distribution have a lower (or higher) probability density than the vector being tested?" If the fraction, f, is small, the vector is an outlier. The test is generally used to look for cases where χ^2 is too large. It is helpful to look at the real distribution of χ^2 for a large set of vectors Rodgers (2000). This can provide more information on the source of the problems, perhaps indicating that the assumed distribution is correct, but there is a small population of outliers (faulty measurements) that do not belong or something wrong with the assumed distribution.

The iteration starts by setting x_a as the state vector and continues until the cost function χ^2 derived from Bayes' theorem is minimized Eriksson et al. (2005),

$$\chi^2 = [y - F(xi)]^T S_\epsilon^{-1} [y - F(xi)] + [x_i - x_a]^T S_x^{-1} [x_i - x_a] \qquad \text{(E.68)}$$

  – If χ^2 increases due to one step: increase γ, do not update x_i, and try again.
  – If χ^2 decreases due to one step: update x_i and decrease γ for the next step.

The factor by which γ increases or decreases is a matter for experimentation in particular cases, and since the elements of the state vector can have different magnitudes and dimensions; they must be scaled.

E.9   A priori restrictions

The 'a a priori restrictions' refers to any constraints on the solution; they are of the same nature as direct measurements, they indicate something about the unknown profile just as the measurements do, and together with the measurements, they determine if we finally have a problem well-posed. If there are no availability restrictions, or if the available restrictions are insufficient, the problem cannot be solved.

Any retrieval method must use a restrictions, either by imposing a grid spaced such that the problem becomes too constrained or by using an explicit a priori pdf. A representation with a finite number of coefficients, such as a grid with a specific interpolation rule, is a priori restrictions that states that any structure that cannot be represented on this grid has zero amplitude. The main objective of a previous restrictions is to restrict the components of the solution that are in the null space or the almost null space of the matrix of the weighting function; therefore, to retain all the measured information, an acceptable representation is

needed and an explicit a priori Rodgers (1990).

Establishing a prior restrictions is not straightforward, as the real prior information is often quite vague and is not amenable to formalization; for example, what can be had is a reasonable expectation that the temperature of the mesosphere varies by more than approximately 100 K. Statistically, the mean climatological profile and its covariance are considered as a measure and its uncertainty.

The profile is mainly specified by a 'complete state vector' x in a fine grid. Using a representation, the a priori restrictions is expressed in terms of a 'reduced state vector' z involving a complete state vector $x = Wz$, where W is an interpolation matrix. The averaging kernel matrix relates $\hat{x}$ to x, rather than $\hat{z}$ to z, so the effect of the restrictions can be seen explicitly and on the same basis for all solution types.

An objective way of choosing grids with an appropriate number and level locations is necessary. In the case of the method of minimum variance and maximum probability (ML), for which there are fewer elements of the state vector than the range of the problem, the previous restriction consists of the representation used. The sensitivity of the solution to measurement noise will increase with the number of elements since less determined state-space components are included. Fewer elements reduce the sensitivity to noise but increase the rendering error, so there will be an optimal number of elements that minimizes the total error.

For climate studies, one must consider what type of results the user wants and then decide which is the best type of product a priori. The user should be able to take an adequately characterized retrieval, and the data provider should consider providing a range of standard products, as well as individual retrievals, such as:

(i) Best estimates of mean profiles for specific regions of space/time.

(ii) Variations of error (or covariances) of the means.

(iii) Variances (or covariances) of set profiles on the means.

(iv) Best estimates of the Fourier coefficients for the length variation.

(v) Best estimates of the Fourier coefficients for the annual variation.

E.10   Observation system design

The design of retrievals methods is an integral part of the overall design of an observing system. The first step is to select an appropriate instrument type and observation geometry. The display geometry for thermal emission or scattering can be from the surface, in situ. The design and optimization process should include:

– Design an advanced model for the instrument, algebraically.

– Identify the parameters of the direct model and the elements of the state vector.

– Construct a direct numerical model and the corresponding derived model.

– Build a numerical retrieval method.

– Select a priori information, both atmospheric and instrumental.

– Determine if the proposed measurements are adequate to determine the proposed target parameters.

– Optimization of the retrieval characteristics concerning the design of the instrument.

The parameters of the direct model should include everything that can affect the signal detected by the instrument in the three main categories:

1. <u>Instrument parameters</u>: such as spectral response, temperature dependencies, detector noise, and others.

2. <u>Atmospheric parameters</u>: include temperature and component distributions, including target quantities.

3. <u>Physical parameters</u>: as spectral data for the relevant gases.

At this stage, the signal should be considered the gross output of the instrument in engineering units before the calibration effects are applied. Initial values, and variances must be set for all parameters, along with covariance matrices.

One of the objectives of the design and optimization of the instrument is to determine which parameters of the model ahead should be objective for retrieval and which are known enough a priori to be considered constant. The simulation should be able to produce the following observing system diagnostics:

– Sensitivity of the measured signal to the target quantities. This includes the matrix of weighting functions.

– Sensitivity of recovery to target amounts. This includes the average of the kernel matrix.

– The contributions to the signal covariance of uncertainties in each of the independent parameters of the direct model.

– The contributions to the covariance of the total retrieval error of the measurement noise and the uncertainties in each of the independent parameters of the direct model. If it has a realistic source atmosphere a priori, evaluate the smoothing error.

– The information content of Shannon and the degrees of freedom for the signal. These diagnostics will determine if the observation system can produce results with resolution and precision and identify what sources of error.

An initial estimate of the viability of an observing system will depend on a comparison between the total error variance of the retrieval and the original requirement and whether the average kernels can provide the required spatial resolution.

Any observing system can be described in terms of many design parameters that can include aspects such as spectral resolution, number, and location of channels, size and design of the input optics, scan patterns, spatial resolution, integration times, and frequency.

Often the only way to objectively optimize the design is to numerically simulate the observing system, select some quality (scalar) characteristic, which may include retrieval accuracy, information content, degrees of freedom for the signal, and the spatial resolution, according to the scientific requirements of the measurement, and optimize it for the design parameters.

There are several ways to describe the vertical distribution of the air mass. The basic parameters are temperature, pressure, density, and height, and either of these two, together with the gas equation and the hydrostatic equation, will determine the other two. Other parameters, such as potential temperature, can also be used as long as they are related to the basic parameters in a known way.

Typically, only three vertical coordinates are considered: pressure (or equivalent, lnp), absolute height relative to the geoid, or height relative to a pressure level. Thus, mass distribution can be described as temperature, density, or height on a pressure scale or as temperature, density, or pressure on a height scale.

The profile can be discretized in terms of a set of values in discrete levels or layers, regularly or irregularly spaced in height or pressure, along with an interpolation rule between the values. Some possibilities are:

(i) A set of pressure levels, separated by layers of constant temperature. Between levels, density is proportional to pressure. A level can have an absolute height.

(ii) A set of pressure levels with temperature given in the levels and linearly interpolated in lnp.

(iii) Density at a set of height levels, with ln linearly interpolated in height.

(iv) Temperature at a set of heights, linearly interpolated and with pressure given at one level.

he amount of a target species can be expressed as a mixing ratio, a gas density, a layer amount, or, in the case of water vapor, as specific humidity. It can also transform these quantities, for example, using the logarithm of the mixing ratio. The linearity of the model forward should be considered as a function of the parameter (mixing ratio, density, or layer amount), and the bias when calculating the statistics of the retrieved quantities if the state vector is a non-linear function of the quantity, since that the error would be significant.

E.11   ARTS/QPack software

The atmospheric radiative transfer simulator (ARTS) is a public domain radiative transfer model for thermal radiation in planetary atmospheres Buehler et al. (2005); Eriksson et al. (2011). It is freely available on the Internet.

ARTS is a physical model that calculates absorption coefficients line-by-line from spectroscopic catalogs. ARTS numerically integrates the monochromatic radiative transfer equation (RTE) for a discrete set of frequencies. The model is applicable to frequencies from the microwave to the thermal infrared. Areas of application include the simulation of remote measurements and the calculation of Jacobians for remote measurement inversion Buehler et al. (2011).

ARTS, that together with Qpack, which is a software tool to complement atmospheric sensors, constitutes a complete and general environment for forward modelling and retrieval work. QPack contains functions for sensor modeling, data reduction, inversion of observed spectra, error characterization, optimization of calculation grids, and random realization of measurements Eriksson et al. (2005).

The indirect nature of the observations requires that a forward model and retrieval environment be available in addition to the actual instrument. Together, these three components can be treated as indispensable parts of the observing system.

It covers data reduction options such as spectral averaging, offers sensitivity to the bands generated by the mixers, gives an angular response of the antenna to weight the spectra of the beam from different directions, and others.

A large number of variables affect a remote sensing measurement. It is not common to retrieve all these variables simultaneously. In Qpack this is achieved by setting the "run level". The levels have a numerical code.

Also, some of the following retrieval and error amounts are handled by Qpack:

- Thermal noise measurement [MEASNOISE_DO].
- Calibration thermal noise [CALINOISE_DO].
- Atmospheric species [RETRIEVAL_TAGS].
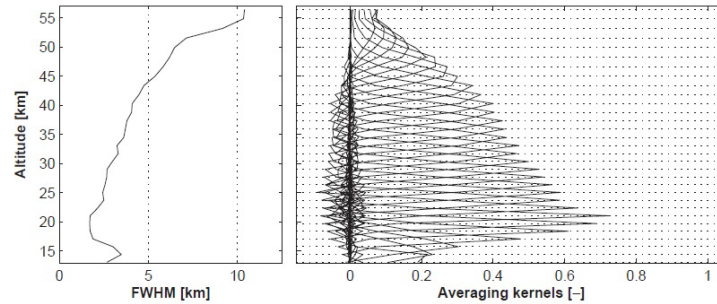
FIGURE E.4. An example of a general investment characterization chart created by $qpcls-invchar$. The example shows the ozone inversion performance for a hypothetical limb sensor measuring emission in the range of 501.18 to 501.58 GHz. Graphs like this are generated if the function is called without output arguments. Otherwise, the function returns the data shown in the figure. Source: Eriksson et al. (2005).

- Temperature [TEMPERATURE_DO].

- Pointing out of set [POINTING_DO].

- Frequency offset [FREQUENCY_DO].

- Continuous absorption [CONTABS_DO].

- Terrestrial broadcast [EGROUND_DO].

- Calibration load temperatures [TB_REFLOADS_DO].

- Proportional calibration error [PROPCAL_DO].

It provides conditional simulations, which generate a set of atmospheric and sensor states, and their corresponding spectral values conditioned to some given statistical assumptions.

It contains functions for configuring input files, such as the $qpopt\_fmono$ function that selects the grid to be used for monochrome calculations in ARTS, and the spectra are treated as piece wise linear functions between the points of monochrome frequencies.

Implementing Qpack has shown that it is possible to combine a high level of generality, flexibility, and computational speed in a retrieval environment, as it handles a relatively high number of retrievals and amounts of error. As well as, it allows general investment characterization graphs created by $qpcls\_invchar$. Figure (E.4) shows an example of the retrieval on ozone investment.

Appendix F

Models AM and Python scripts

The AM files used to achieve the OEM water vapor recoveries are shown in this appendix, as well as the Python code for the simplest example based on a simple 5-layer atmospheric model.

```python
# Generate a simulated calibrated brightness temperature spectrum.

from numpy.random import default_rng
rng = default_rng()

Trx = 300. # Assumed receiver noise temperature [K]
snr = 250. # Assumed signal-to-noise ratio sqrt(BW * tint)
file = open('simulated.out')
for line in file:
    tok    = line.split()
    f      = float(tok[0]) # GHz
    Tsky   = float(tok[1]) # K
    Tsys   = Trx + Tsky
    Tnoise = Tsys / snr
    Tcal   = Tsky + Tnoise * rng.standard_normal(1)[0]
    print("{:.6e} {:.6e} {:.6e}".format(f, Tcal, Tnoise))
```

FIGURE F.1. Python script to add Gaussian noise to the simulated spectrum. Source: Collaboration of Harvard University-Scott Paine.

```
# File prior.amc - Prior profiles for a simple retrieval of a 5-layer
# water vapor profile.  Jacobians are computed for the water vapor
# concentrations on each layer.  The temperature profile is assumed
# fixed.
#
f 20 GHz  26 GHz  10 MHz
output f GHz Trj
jacobian Trj

za 0 deg

T0 2.7 K

layer
Pbase 0 mbar
Tbase 217 K

layer
Pbase 200 mbar
Tbase 217 K
column dry_air hydrostatic
column h2o hydrostatic 9.0e-05 9.0e-5

layer
Pbase 400 mbar
Tbase 241 K
column dry_air hydrostatic
column h2o hydrostatic 1.7e-4 1.7e-4

layer
Pbase 600 mbar
Tbase 261 K
column dry_air hydrostatic
column h2o hydrostatic 1.1e-3 1.1e-3

layer
Pbase 800 mbar
Tbase 275 K
column dry_air hydrostatic
column h2o hydrostatic 3.1e-3 3.1e-3

layer
Pbase 1000 mbar
Tbase 288 K
column dry_air hydrostatic
column h2o hydrostatic 6.3e-3 6.3e-3
```

FIGURE F.2. AM file "prior.amc" that indicates the parameters that an a priori must have, where it indicates some data on water proportions, pressure, temperature and others. Source: Collaboration of Harvard University-Scott Paine (example 2.4) Paine (2012)

```
# File simulated.amc - Atmospheric state to generate a simulated
# calibrated Trj spectrum to test a simple OEM retrieval.
#
f 20 GHz  26 GHz  0.1 MHz
output f GHz Trj

za 0 deg

T0 2.7 K

layer
Pbase 0 mbar
Tbase 217 K

layer
Pbase 200 mbar
Tbase 217 K
column dry_air hydrostatic
column h2o hydrostatic 7.0e-05

layer
Pbase 400 mbar
Tbase 241 K
column dry_air hydrostatic
column h2o hydrostatic 1.0e-4

layer
Pbase 600 mbar
Tbase 261 K
column dry_air hydrostatic
column h2o hydrostatic 8.0e-4

layer
Pbase 800 mbar
Tbase 275 K
column dry_air hydrostatic
column h2o hydrostatic 2.0e-3

layer
Pbase 1000 mbar
Tbase 288 K
column dry_air hydrostatic
column h2o hydrostatic 5.0e-3
```

FIGURE F.3. AM file of the simulated spectrum, "simulated.amc" with proportions drier than the a priori and with added Gaussian noise. Source: Collaboration of Harvard University-Scott Paine.

```
# Basic linear OEM retrieval example.  Notation follows
# C. D. Rodgers 2004, "Inverse Methods for Atmospheric
# Sounding, Theory and Practice."  World Scientific.

import numpy as np
from scipy import linalg


#
# Prior state vector xa and its inverse covariance matrix Sa_inv.
#
# For this example, we're assuming a fixed temperature profile.
# The only elements of the state vector to be retrieved are
# the water vapor mixing ratios on the 5 model layers, arranged
# in top-down order:
#
#   0 h2o vmr on 0   -  200 mbar layer
#   1 h2o vmr on 200 -  400 mbar layer
#   2 h2o vmr on 400 -  600 mbar layer
#   3 h2o vmr on 600 -  800 mbar layer
#   4 h2o vmr on 800 - 1000 mbar layer
#
# The prior state for this example was constructed assuming
# approximately 50% relative humidity on all the layers.  For
# simplicity, we'll (unrealistically) assume that there is
# no correlation between the water vapor concentrations, so
# that the prior covariance matrix is diagonal.  Further, we'll
# assume the humidities might vary from 25% - 75%, so we'll
# set the stardard deviations to half the prior value.  The
# diagonal elements of the inverse covariance matrix will
# be 1 / (std dev)^2 for the corresponding prior state
# vector element.
#
xa      = np.array([9.0e-5, 1.7e-4, 1.1e-3, 3.1e-3, 6.3e-3]).reshape(5,1)
Sa_inv =  np.diag([ 4.9e8,  1.4e8,  3.3e6,  4.2e5,  1.0e5])


#
# For this example, the model will be linearized about the prior
# state.  That is, the reference state x0 for the linearized
# model is identical to the a priori state xa.  Nevertheless,
# we'll keep them distinct in case we want to change that.
#
x0 = xa


#
# The reference spectrum y0 for the linearized forward model is
# the model spectrum computed by am  at the reference state x0.
# Read y0 and the jacobian matrix K at x0 out of the file
# computed by am.
#
am_linearized_model = np.loadtxt("prior.out")
y0 = am_linearized_model[:,1]
y0 = y0.reshape(len(y0), 1)
K  = am_linearized_model[:,2:]
```

```python
#
# Read the simulated measured spectrum y and its standard deviation,
# and compute the (diagonal) inverse error covariance matrix Se_inv.
#
simulated_spec = np.loadtxt("simulated_Tcal")
y         = simulated_spec[:,1]
y         = y.reshape(len(y), 1)
y_stddev  = simulated_spec[:,2]
y_inv_var = np.square(np.reciprocal(y_stddev))
Se_inv    = np.diag(y_inv_var)


#
# Compute the gain matrix G (cf. Rodgers Eq. 2.45)
#
try:
    G = linalg.inv(K.T.dot(Se_inv.dot(K)) + Sa_inv).dot(K.T.dot(Se_inv))
except LinAlgError as e:
    print(e)
    print(e.args)
    exit()


#
# Compute the retrieved state vector xret its covariance
# matrix Sret, and the averaging kernel matrix Aret.
# Print them out.
#
xret = xa + G.dot((y - y0) - K.dot(xa - x0))
try:
    Sret = linalg.inv(K.T.dot(Se_inv.dot(K)) + Sa_inv)
except LinAlgError as e:
    print(e)
    print(e.args)
    exit()

Aret = G.dot(K)

np.set_printoptions(precision=3)
print("\nRetrieved H2O vmrs:")
print(xret)
print("\nStatistical uncertainties:")
print((np.sqrt(np.diag(Sret))).reshape(5,1))
print("\nFull covariance matrix for retrieved vmrs:")
print(Sret)
print("\nDegrees of freedom for signal:")
print("{:.3f}".format(np.trace(Aret)))
print("\nFull averaging kernel matrix:")
print(Aret)
```

FIGURE F.4. Python script taking into account the recovery equations in Rodgers (1976), and the corresponding parameters of the 5 layers of the model. Source: Collaboration of Harvard University-Scott Paine.

```
# File simulated.amc - Atmospheric state to generate a simulated
# calibrated Trj spectrum to test a simple OEM retrieval.
#
f 20 GHz  26 GHz  0.1 MHz
output f GHz Trj

za 0 deg

T0 2.7 K

layer
Pbase 0 mbar
Tbase 217 K

layer
Pbase 200 mbar
Tbase 217 K
column dry_air hydrostatic
column h2o hydrostatic 6.079e-05

layer
Pbase 400 mbar
Tbase 241 K
column dry_air hydrostatic
column h2o hydrostatic 1.413e-04

layer
Pbase 600 mbar
Tbase 261 K
column dry_air hydrostatic
column h2o hydrostatic 7.349e-04

layer
Pbase 800 mbar
Tbase 275 K
column dry_air hydrostatic
column h2o hydrostatic 1.859e-03

layer
Pbase 1000 mbar
Tbase 288 K
column dry_air hydrostatic
column h2o hydrostatic 5.165e-03
```

FIGURE F.5. AM file where the recovered water vapor data is substituted to evaluate the recovered spectrum.

```
?
? Usage:
?    am this_file f_min f_max df zenith_angle trop_h2o_scale_factor
? Example:
?    am this_file  0 GHz  300 GHz  10 MHz  0 deg  1.0
?
f %1 %2   %3 %4   %5 %6
?output   f GHz   tau   tx   Trj K   Tb K


output   f GHz   Tb K L m


za %7 %8
tol 1e-4


Nscale troposphere h2o %9


T0 2.7 K


layer   mesosphere
     Pbase                                0.100000000000        mbar
     Tbase                                220.764924242424          K
 lineshape   Voigt-Kielkopf
    column      dry_air         vmr
    column          h2o         vmr   0.000006620654


     layer   mesosphere
     Pbase                                0.300000000000        mbar
     Tbase                                242.836590909091          K
 lineshape   Voigt-Kielkopf
    column      dry_air         vmr
    column          h2o         vmr   0.000006852264


     layer   mesosphere
     Pbase                                0.400000000000        mbar
     Tbase                                248.851136363636          K
 lineshape   Voigt-Kielkopf
    column      dry_air         vmr
    column          h2o         vmr   0.000006839736


     layer   mesosphere
     Pbase                                0.500000000000        mbar
     Tbase                                254.266590909091          K
 lineshape   Voigt-Kielkopf
    column      dry_air         vmr
    column          h2o         vmr   0.000006813565


     layer   mesosphere
     Pbase                                0.700000000000        mbar
     Tbase                                261.955909090909          K
 lineshape   Voigt-Kielkopf
    column      dry_air         vmr
    column          h2o         vmr   0.000006746007
```

```
    layer   stratosphere
    Pbase                                     1.000000000000          mbar
    Tbase                                   265.041742424242             K
lineshape   Voigt-Kielkopf
   column       dry_air         vmr
   column           h2o         vmr    0.000006627161


    layer   stratosphere
    Pbase                                     2.000000000000          mbar
    Tbase                                   256.211893939394             K
   column       dry_air         vmr
   column           h2o         vmr    0.000006281857


    layer   stratosphere
    Pbase                                     3.000000000000          mbar
    Tbase                                   248.493636363636             K
   column       dry_air         vmr
   column           h2o         vmr    0.000006002964


    layer   stratosphere
    Pbase                                     4.000000000000          mbar
    Tbase                                   243.797878787879             K
   column       dry_air         vmr
   column           h2o         vmr    0.000005756627


    layer   stratosphere
    Pbase                                     5.000000000000          mbar
    Tbase                                   239.935909090909             K
   column       dry_air         vmr
   column           h2o         vmr    0.000005551667


    layer   stratosphere
    Pbase                                     7.000000000000          mbar
    Tbase                                   234.096212121212             K
   column       dry_air         vmr
   column           h2o         vmr    0.000005249776


    layer   stratosphere
    Pbase                                    10.000000000000          mbar
    Tbase                                   229.281969696970             K
   column       dry_air         vmr
   column           h2o         vmr    0.000004999467


    layer   stratosphere
    Pbase                                    20.000000000000          mbar
    Tbase                                   221.430000000000             K
   column       dry_air         vmr
   column           h2o         vmr    0.000004698992


    layer   stratosphere
    Pbase                                    30.000000000000          mbar
    Tbase                                   216.446287878788             K
   column       dry_air         vmr
   column           h2o         vmr    0.000004595865
```

```
layer   stratosphere
Pbase                                   40.000000000000        mbar
Tbase                                   212.461287878788         K
column        dry_air        vmr
column            h2o        vmr    0.000004506262

layer   stratosphere
Pbase                                   50.000000000000        mbar
Tbase                                   208.821590909091         K
column        dry_air        vmr
column            h2o        vmr    0.000004438529

layer   stratosphere
Pbase                                   70.000000000000        mbar
Tbase                                   201.186590909091         K
column        dry_air        vmr
column            h2o        vmr    0.000004405389

layer   troposphere
Pbase                                  100.000000000000        mbar
Tbase                                   199.648030303030         K
column        dry_air        vmr
column            h2o        vmr    0.000005107609

layer   troposphere
Pbase                                  200.000000000000        mbar
Tbase                                   219.061590909091         K
column        dry_air        vmr
column            h2o        vmr    0.000060213962

layer   troposphere
Pbase                                  250.000000000000        mbar
Tbase                                   229.449621212121         K
column        dry_air        vmr
column            h2o        vmr    0.000145898932

layer   troposphere
Pbase                                  300.000000000000        mbar
Tbase                                   238.889015151515         K
column        dry_air        vmr
column            h2o        vmr    0.000243371591

layer   troposphere
Pbase                                  350.000000000000        mbar
Tbase                                   247.150530303030         K
column        dry_air        vmr
column            h2o        vmr    0.000347577727
```

```
 layer   troposphere
  Pbase                                 400.000000000000        mbar
  Tbase                                 254.156969696970          K
column        dry_air        vmr
column            h2o        vmr   0.000499802803

 layer   troposphere
  Pbase                                 450.000000000000        mbar
  Tbase                                 260.362196969697          K
column        dry_air        vmr
column            h2o        vmr   0.000712503712

 layer   troposphere
  Pbase                                 500.000000000000        mbar
  Tbase                                 265.909015151515          K
column        dry_air        vmr
column            h2o        vmr   0.000989594545

 layer   troposphere
  Pbase                                 550.000000000000        mbar
  Tbase                                 270.952272727273          K
column        dry_air        vmr
column            h2o        vmr   0.001281536591

 layer   troposphere
  Pbase                                 600.000000000000        mbar
  Tbase                                 275.503181818182          K
column        dry_air        vmr
column            h2o        vmr   0.001592767954

 layer   troposphere
  Pbase                                 650.000000000000        mbar
  Tbase                                 279.540000000000          K
column        dry_air        vmr
column            h2o        vmr   0.002070358182

 layer   troposphere
  Pbase                                 700.000000000000        mbar
  Tbase                                 283.181893939394          K
column        dry_air        vmr
column            h2o        vmr   0.002741484394

 layer   troposphere
  Pbase                                 715.000000000000        mbar
  Tbase                                 284.194696969697          K
column        dry_air        vmr
column            h2o        vmr   0.002997028030
```

FIGURE F.6. AM file with the water vapor parameters of 31 atmospheric layers for Cerro Ventarrones. Its outputs, layer type, pressure, Nscale and others are included. This file will be used for the recoveries of the different spectra in the three proposed models.

Bibliography

Anderson, G. P., Clough, S. A., Kneizys, F., Chetwynd, J. H., and Shettle, E. P. (1986). "Afgl atmospheric constituent profiles (0.120 km)." Tech. rep., Air Force Geophysics Lab Hanscom AFB MA.

Asaki, Y., Kobayashi, H., Hagiwara, N., and Ishiguro, M. (2000). "Novel method to compare tropospheric path delay fluctuations with 22-ghz water vapor line emissions." In *Radio Telescopes*, vol. 4015, 589–596, SPIE.

Backus, G., and Gilbert, F. (1970). "Uniqueness in the inversion of inaccurate gross earth data." *Philosophical Transactions of the Royal Society of London. Series A, Mathematical and Physical Sciences*, *266*(1173), 123–192.

Barber, R., Tennyson, J., Harris, G., and Tolchenov, R. (2006). "A high-accuracy computed water line list." *Monthly Notices of the Royal Astronomical Society*, *368*(3), 1087–1094.

Bernath, P. F., McElroy, C. T., Abrams, M., Boone, C. D., Butler, M., Camy-Peyret, C., Carleer, M., Clerbaux, C., Coheur, P.-F., Colin, R., et al. (2005). "Atmospheric chemistry experiment (ace): mission overview." *Geophysical Research Letters*, *32*(15).

Blackwell, W. J., and Chen, F. W. (2009). *Neural networks in atmospheric remote sensing*. Artech House.

Bleisch, R., and Kämpfer, N. (2012). "Miawara retrievals: Currently used retrievals and attempts of a combined retrieval from surface to mesosphere."

Bleisch, R., Kämpfer, N., and Haefele, A. (2011). "Retrieval of tropospheric water vapour by using spectra of a 22 ghz radiometer." *Atmospheric Measurement Techniques*, *4*(9), 1891–1903.

Brasseur, G., Orlando, J. J., Tyndall, G. S., et al. (1999). *Atmospheric chemistry and global change*. Oxford University Press.

Brasseur, G. P. (2013). *The stratosphere and its role in the Climate System*, vol. 54. Springer Science & Business Media.

Braun, C. L., and Smirnov, S. N. (1993). "Why is water blue?" *Journal of Chemical Education*, *70*(8), 612.

Brekke, A. (2012). *Physics of the upper polar atmosphere*. Springer Science & Business Media.

Bruegge, C. J., Conel, J. E., Green, R. O., Margolis, J. S., Holm, R. G., and Toon, G. (1992). "Water vapor column abundance retrievals during fife." *Journal of Geophysical Research: Atmospheres*, *97*(D17), 18759–18768.

Buehler, S., Eriksson, P., Kuhn, T., Von Engeln, A., and Verdes, C. (2005). "Arts, the atmospheric radiative transfer simulator." *Journal of Quantitative Spectroscopy and Radiative Transfer*, *91*(1), 65–93.

Buehler, S., Kuvatov, M., John, V., Milz, M., Soden, B., Jackson, D., and Notholt, J. (2008). "An upper tropospheric humidity data set from operational satellite microwave data." *Journal of Geophysical Research: Atmospheres*, *113*(D14).

Buehler, S. A., Eriksson, P., and Lemke, O. (2011). "Absorption lookup tables in the radiative transfer model arts." *Journal of Quantitative Spectroscopy and Radiative Transfer*, *112*(10), 1559–1567.

Cantalloube, F., Milli, J., Böhm, C., Crewell, S., Navarrete, J., Rehfeld, K., Sarazin, M., and Sommani, A. (2020). "The impact of climate change on astronomical observations." *Nature Astronomy*, *4*(9), 826–829.

Chabrillat, S., and Fonteyn, D. (2003). "Modelling long-term changes of mesospheric temperature and chemistry." *Advances in Space Research*, *32*(9), 1689–1700.

Conrath, B. J. (1972). "Vertical resolution of temperature profiles obtained from remote radiation measurements." *Journal of Atmospheric Sciences*, *29*(7), 1262–1271.

Cortés, F., Cortés, K., Reeves, R., Bustos, R., and Radford, S. (2020). "Twenty years of precipitable water vapor measurements in the chajnantor area." *Astronomy & Astrophysics*, *640*, A126.

Cortés Guerrero, F. A., et al. (2015). "Caracterización atmosférica en zonas extremas y su relevancia en astronomía."

Deuber, B., Haefele, A., Feist, D. G., Martin, L., Kämpfer, N., Nedoluha, G. E., Yushkov, V., Khaykin, S., Kivi, R., and Vömel, H. (2005). "Middle atmospheric water vapour radiometer (miawara): Validation and first results of the lapbiat upper tropospheric lower stratospheric water vapour validation project (lautlos-wavvap) campaign." *Journal of Geophysical Research: Atmospheres*, *110*(D13).

Deuber, B., and Kämpfer, N. (2004). "Minimized standing waves in microwave radiometer balancing calibration." *Radio Science*, *39*(1), 1–8.

Deuber, B., Kampfer, N., and Feist, D. G. (2004). "A new 22-ghz radiometer for middle atmospheric water vapor profile measurements." *IEEE Transactions on Geoscience and Remote Sensing*, *42*(5), 974–984.

Dicke, R. H. (1946). "The measurement of thermal radiation at microwave frequencies." In *Classics in Radio Astronomy*, 106–113, Springer.

Eichinger, W., Cooper, D., Forman, P., Griegos, J., Osborn, M., Richter, D., Tellier, L., and Thornton, R. (1999). "The development of a scanning raman water vapor lidar for boundary layer and tropospheric observations." *Journal of Atmospheric and Oceanic Technology*, *16*(11), 1753–1766.

Elgered, G., Rönnäng, B., and Askne, J. (1982). "Measurements of atmospheric water vapor with microwave radiometry." *Radio Science*, *17*(5), 1258–1264.

Engelen, R. J., and Stephens, G. L. (1999). "Characterization of water-vapour retrievals from tovs/hirs and ssm/t-2 measurements." *Quarterly Journal of the Royal Meteorological Society*, *125*(553), 331–351.

Eriksson, P., Buehler, S., Davis, C., Emde, C., and Lemke, O. (2011). "Arts, the atmospheric radiative transfer simulator, version 2." *Journal of Quantitative Spectroscopy and Radiative Transfer*, *112*(10), 1551–1558.

Eriksson, P., Jiménez, C., and Buehler, S. A. (2005). "Qpack, a general tool for instrument simulation and retrieval work." *Journal of Quantitative Spectroscopy and Radiative Transfer*, *91*(1), 47–64.

Fisher, J., and Morgan, M. (2008). "Analysis of a single-conversion, analog/digital sideband-separating mixer prototype national radio astronomy observatory electronics division internal report no. 320."

Fisher, R. A., et al. (1921). "014: On the" probable error" of a coefficient of correlation deduced from a small sample."

Golchert, S. H., Hochschild, G., and Groß, J. (2010). "Middle-atmospheric water vapour profiles above the zugspitze obtained with a new ground-based 22 ghz spectroradiometer." In *2010 11th Specialist Meeting on Microwave Radiometry and Remote Sensing of the Environment*, 152–154, IEEE.

Golchert, S. H. W. (2009). *Stratospheric Water Vapour in the Tropics: Observations by Ground-Based Microwave Radiometry*. Ph.D. thesis, Universität Bremen.

Goldstein, S. (1955). "A comparison of two radiometer circuits." *Proceedings of the IRE*, *43*(11), 1663–1666.

Gross, E. (1955). "Shape of collision-broadened spectral lines." *Physical Review*, *97*(2), 395.

Haefele, A., De Wachter, E., Hocke, K., Kämpfer, N., Nedoluha, G., Gomez, R., Eriksson, P., Forkman, P., Lambert, A., and Schwartz, M. (2009). "Validation of ground-based microwave radiometers at 22 ghz for stratospheric and mesospheric water vapor." *Journal of Geophysical Research: Atmospheres*, *114*(D23).

Hajj, G. A., Ao, C., Iijima, B., Kuang, D., Kursinski, E., Mannucci, A., Meehan, T., Romans, L., de La Torre Juarez, M., and Yunck, T. (2004). "Champ and sac-c atmospheric occultation results and intercomparisons." *Journal of Geophysical Research: Atmospheres*, *109*(D6).

Hale, G. M., and Querry, M. R. (1973). "Optical constants of water in the 200-nm to 200-μm wavelength region." *Applied optics*, *12*(3), 555–563.

Hall, R. T., and Dowling, J. M. (1967). "Pure rotational spectrum of water vapor." *The Journal of Chemical Physics*, *47*(7), 2454–2461.

Hallgren, K., Hartogh, P., and Jarchow, C. (2012). "Climatology of middle atmospheric water vapour above the alomar observatory in northern norway." *Atmospheric Chemistry and Physics Discussions*, *12*(12), 31531–31560.

Hartmann, J.-M., Boulet, C., and Robert, D. (2021). *Collisional effects on molecular spectra: laboratory experiments and models, consequences for applications*. Elsevier.

Hartogh, P., Sonnemann, G., Grygalashvyly, M., and Jarchow, C. (2011). "Ozone trends in the mid-latitude stratopause region based on microwave measurements at lindau (51.66° n, 10.13° e), the ozone reference model, and model calculations." *Advances in space research*, *47*(11), 1937–1948.

Hartogh, P., Sonnemann, G., Grygalashvyly, M., Song, L., Berger, U., and Lübken, F.-J. (2010). "Water vapor measurements at alomar over a solar cycle compared with model calculations by lima." *Journal of Geophysical Research: Atmospheres*, *115*(D1).

Heath, D., Krueger, A., and Park, H. (1978). "The solar backscatter ultraviolet (sbuv) and total ozone mapping spectrometer (toms) experiment." *In its The Nimbus 7 User's Guide p 175-212 (SEE N79-20148 11-12*, 175–212.

Hill, R. (1986). "Water vapor–absorption line shape comparison using the 22-ghz line: The van vleck–weisskopf shape affirmed." *Radio Science*, *21*(3), 447–451.

Hirshorn, S. R., Voss, L. D., and Bromley, L. K. (2017). "Nasa systems engineering handbook." Tech. rep.

Janssen, M. A. (1994). "Atmospheric remote sensing by microwave radiometry."

Jarosik, N., Bennett, C., Halpern, M., Hinshaw, G., Kogut, A., Limon, M., Meyer, S., Page, L., Pospieszalski, M., Spergel, D., et al. (2003). "Design, implementation, and testing of the microwave anisotropy probe radiometers." *The Astrophysical Journal Supplement Series*, *145*(2), 413.

Kaatze, U., Behrends, R., and Pottel, R. (2002). "Hydrogen network fluctuations and dielectric spectrometry of liquids." *Journal of Non-Crystalline Solids*, *305*(1-3), 19–28.

Kämpfer, N. (2012). *Monitoring atmospheric water vapour: ground-based remote sensing and in-situ methods*, vol. 10. Springer.

Kämpfer, N., Deuber, B., Feist, D., Gerber, D., Mätzler, C., Martin, L., Morland, J., and Vasic, V. (2003). "Microwave remote sensing of water vapor in the atmosphere." *Geographica Helvetica*, *58*(2), 81–89.

Kaplan, L. D. (1959). "Inference of atmospheric structure from remote radiation measurements." *Josa*, *49*(10), 1004–1007.

Karmakar, P. K. (2019). *Ground-based microwave radiometry and remote sensing: Methods and applications*. CRC Press.

Kausch, W., Noll, S., Smette, A., Kimeswenger, S., Barden, M., Szyszka, C., Jones, A., Sana, H., Horst, H., and Kerber, F. (2015). "Molecfit: A general tool for telluric absorption correction-ii. quantitative evaluation on eso-vlt/x-shooterspectra." *Astronomy & Astrophysics*, *576*, A78.

Klein, B. (2014). "Back-ends for thz heterodyne systems: Fast fourier transform spectrometer (ffts)." Apex Conference.

Kooi, J. W. (2008). *Advanced receivers for submillimeter and far infrared astronomy*. Rijkuniversiteit Groningen.

Kraus, J. D., Tiuri, M., Räisänen, A. V., and Carr, T. D. (1966). *Radio astronomy*, vol. 66. McGraw-Hill New York.

Laštovička, J. (2009). "Global pattern of trends in the upper atmosphere and ionosphere: Recent progress." *Journal of Atmospheric and Solar-Terrestrial Physics*, *71*(14-15), 1514–1528.

Le Texier, H., Solomon, S., and Garcia, R. (1988). "The role of molecular hydrogen and methane oxidation in the water vapour budget of the stratosphere." *Quarterly Journal of the Royal Meteorological Society*, *114*(480), 281–295.

Le Vine, D., and Skou, N. (2006). *Microwave radiometer systems: design and analysis*. Artech.

Levenberg, K. (1944). "A method for the solution of certain non-linear problems in least squares." *Quarterly of applied mathematics*, *2*(2), 164–168.

Li, M.-S., Li, R., Wang, N., and Zheng, X.-W. (2020). "Research and application of reanalysis data for radio astronomical site testing." *Research in Astronomy and Astrophysics*, *20*(12), 200.

Li, Z., Muller, J.-P., and Cross, P. (2003). "Comparison of precipitable water vapor derived from radiosonde, gps, and moderate-resolution imaging spectroradiometer measurements." *Journal of Geophysical Research: Atmospheres*, *108*(D20).

Liverpool, U. (2023). "Chemtube3d: An internationally renowned open educational resource, project doi: 10.26303/skjx-ts11."

Maas, S. A. (1986). "Microwave mixers." *Norwood*.

Marquardt, D. W. (1963). "An algorithm for least-squares estimation of nonlinear parameters." *Journal of the society for Industrial and Applied Mathematics*, *11*(2), 431–441.

Marshall, J., McLean, I., and Casali, M. (2008). "Proc. spie conf. ser. vol. 7014, ground-based and airborne instrumentation for astronomy ii." SPIE, Bellingham.

Ménard, R., Chabrillat, S., Robichaud, A., de Grandpré, J., Charron, M., Rochon, Y., Batchelor, R., Kallaur, A., Reszka, M., and Kaminski, J. W. (2020). "Coupled stratospheric chemistry–meteorology data assimilation. part i: Physical background and coupled modeling aspects." *Atmosphere*, *11*(2), 150.

Mennella, A., Bersanelli, M., Butler, R., Maino, D., Mandolesi, N., Morgante, G., Valenziano, L., Villa, F., Gaier, T., Seiffert, M., et al. (2003a). "Advanced pseudo-correlation radiometers for the planck-lfi instrument." *arXiv preprint astro-ph/0307116*.

Mennella, A., Bersanelli, M., Seiffert, M., Kettle, D., Roddis, N., Wilkinson, A., and Meinhold, P. (2003b). "Offset balancing in pseudo-correlation radiometers for cmb measurements." *Astronomy & Astrophysics*, *410*(3), 1089–1100.

Messer, J., De Lucia, F. C., and Helminger, P. (1983). "The pure rotational spectrum of water vapor—a millimeter, submillimeter, and far infrared analysis." *International journal of infrared and millimeter waves*, *4*(4), 505–539.

Mieruch, S., Noël, S., Bovensmann, H., and Burrows, J. (2008). "Analysis of global water vapour trends from satellite measurements in the visible spectral range." *Atmospheric Chemistry and Physics*, *8*(3), 491–504.

Milz, M., Von Clarmann, T., Fischer, H., Glatthor, N., Grabowski, U., Höpfner, M., Kellmann, S., Kiefer, M., Linden, A., Mengistu Tsidu, G., et al. (2005). "Water vapor distributions measured with the michelson interferometer for passive atmospheric sounding on board envisat (mipas/envisat)." *Journal of Geophysical Research: Atmospheres*, *110*(D24).

Mohanakumar, K. (2008). *Stratosphere troposphere interactions: an introduction*. Springer Science & Business Media.

Mölders, N., and Kramm, G. (2014). *Lectures in meteorology*. Springer.

Morgan, M. A., and Fisher, J. R. (2010). "Experiments with calibrated digital sideband-separating downconversion." *Publications of the Astronomical Society of the Pacific*, *122*(889), 326.

Morland, J., Deuber, B., Feist, D., Martin, L., Nyeki, S., Kämpfer, N., Mätzler, C., Jeannet, P., and Vuilleumier, L. (2006). "The startwave atmospheric water database." *Atmospheric chemistry and physics*, *6*(8), 2039–2056.

Mote, P. W., Rosenlof, K. H., McIntyre, M. E., Carr, E. S., Gille, J. C., Holton, J. R., Kinnersley, J. S., Pumphrey, H. C., Russell III, J. M., and Waters, J. W. (1996). "An atmospheric tape recorder: The imprint of tropical tropopause temperatures on stratospheric water vapor." *Journal of Geophysical Research: Atmospheres*, *101*(D2), 3989–4006.

Müller, S. C., Kämpfer, N., Feist, D. G., Haefele, A., Milz, M., Sitnikov, N., Schiller, C., Kiemle, C., and Urban, J. (2008). "Validation of stratospheric water vapour measurements from the airborne microwave radiometer amsos." *Atmospheric chemistry and physics*, *8*(12), 3169–3183.

Murtagh, D., Frisk, U., Merino, F., Ridal, M., Jonsson, A., Stegman, J., Witt, G., Eriksson, P., Jiménez, C., Megie, G., et al. (2002). "An overview of the odin atmospheric mission." *Canadian Journal of Physics*, *80*(4), 309–319.

Nanzer, J. A. (2012). *Microwave and millimeter-wave remote sensing for security applications*. Artech House.

Naylor, D. A., Chapman, I. M., and Gom, B. G. (2002). "Measurements of atmospheric water vapor above mauna kea using an infrared radiometer." In *Atmospheric radiation measurements and applications in climate*, vol. 4815, 36–45, SPIE.

Nedoluha, G. E., Bevilacqua, R. M., Gomez, R. M., Hicks, B. C., Russell Iii, J. M., and Connor, B. J. (2003). "An evaluation of trends in middle atmospheric water vapor as measured by haloe, wvms, and poam." *Journal of Geophysical Research: Atmospheres*, *108*(D13).

Nedoluha, G. E., Bevilacqua, R. M., Gomez, R. M., Thacker, D., Waltman, W. B., and Pauls, T. A. (1995). "Ground-based measurements of water vapor in the middle atmosphere." *Journal of Geophysical Research: Atmospheres*, *100*(D2), 2927–2939.

Nedoluha, G. E., Bevilacqua, R. M., Gomez, R. M., Waltman, W. B., Hicks, B. C., Thacker, D., Russell III, J. M., Abrams, M., Pumphrey, H. C., and Connor, B. J. (1997). "A comparative study of mesospheric water vapor measurements from the ground-based water vapor millimeter-wave spectrometer and space-based instruments." *Journal of Geophysical Research: Atmospheres*, 102(D14), 16647–16661.

Nedoluha, G. E., Gomez, R. M., Hicks, B. C., Helmboldt, J., Bevilacqua, R. M., and Lambert, A. (2011). "Ground-based microwave measurements of water vapor from the midstratosphere to the mesosphere." *Journal of Geophysical Research: Atmospheres*, 116(D2).

Nedoluha, G. E., Kiefer, M., Lossow, S., Gomez, R. M., Kämpfer, N., Lainer, M., Forkman, P., Christensen, O. M., Oh, J. J., Hartogh, P., et al. (2017). "The sparc water vapor assessment ii: intercomparison of satellite and ground-based microwave measurements." *Atmospheric chemistry and physics*, 17(23), 14543–14558.

Olmi, L. (2001). "Systematic observations of anomalous refraction at millimeter wavelengths." *Astronomy & Astrophysics*, 374(1), 348–357.

Paine, S. (2012). "The am atmospheric model." *Zenodo*.

Palacios, J. (2021). "Back-end digital para radiómetros de vapor de agua de pseudo-correlación." Memoria de Título, Universidad de Concepción.

Parrish, A., Dezafra, R., Solomon, P., and Barrett, J. (1988). "A ground-based technique for millimeter wave spectroscopic observations of stratospheric trace constituents." *Radio Science*, 23(2), 106–118.

Pope, R. M., and Fry, E. S. (1997). "Absorption spectrum (380–700 nm) of pure water. ii. integrating cavity measurements." *Applied optics*, 36(33), 8710–8723.

Pozar, D. M. (2011). *Microwave engineering*. John wiley & sons.

Reeves, R. (2019). "Fundamentos de instrumentación astronómica." Apuntes de aula. Departamento de Astronomía, Universidad de Concepción.

Resch, G. (1983). "Another look at the optimum frequencies for a water vapour radiometer. tda progress report, 42–76." *Jet Propulsion Laboratory, Pasadena, California, USA*.

Rodgers, C. D. (1976). "Retrieval of atmospheric temperature and composition from remote measurements of thermal radiation." *Reviews of Geophysics*, 14(4), 609–624.

Rodgers, C. D. (1990). "Characterization and error analysis of profiles retrieved from remote sounding measurements." *Journal of Geophysical Research: Atmospheres*, 95(D5), 5587–5595.

Rodgers, C. D. (2000). *Inverse methods for atmospheric sounding: theory and practice*, vol. 2. World scientific.

Rosenlof, K. H., and Reid, G. C. (2008). "Trends in the temperature and water vapor content of the tropical lower stratosphere: Sea surface connection." *Journal of Geophysical Research: Atmospheres*, 113(D6).

Rozanov, A., Weigel, K., Bovensmann, H., Dhomse, S., Eichmann, K.-U., Kivi, R., Rozanov, V., Vömel, H., Weber, M., and Burrows, J. (2011). "Retrieval of water vapor vertical distributions in the upper troposphere and the lower stratosphere from sciamachy limb measurements." *Atmospheric Measurement Techniques*, *4*(5), 933–954.

Russell III, J. M., Gordley, L. L., Park, J. H., Drayson, S. R., Hesketh, W. D., Cicerone, R. J., Tuck, A. F., Frederick, J. E., Harries, J. E., and Crutzen, P. J. (1993). "The halogen occultation experiment." *Journal of Geophysical Research: Atmospheres*, *98*(D6), 10777–10797.

Rybicki, G. B., and Lightman, A. P. (1991). *Radiative processes in astrophysics*. John Wiley & Sons.

Salazar, L. d. l. M. B. (2018). *Desarrollo de Fuentes de Calibración Para Instrumentos de Observación Submilimétrica*. Ph.D. thesis, Universidad de Concepción.

Sapunar Opazo, R. I. (2015). "Diseño e implementación de un espectrómetro de alta resolución basado en fpga para análisis de señales radioastronómico."

Scheiben, D., Schanz, A., Tschanz, B., and Kämpfer, N. (2013). "Diurnal variations in middle-atmospheric water vapor by ground-based microwave radiometry." *Atmospheric chemistry and physics*, *13*(14), 6877–6886.

Seele, C., and Hartogh, P. (2000). "A case study on middle atmospheric water vapor transport during the february 1998 stratospheric warming." *Geophysical research letters*, *27*(20), 3309–3312.

Segelstein, D. J. (1981). *The complex refractive index of water*. Ph.D. thesis, University of Missouri–Kansas City.

Shannon, C. E. (1948). "A mathematical theory of communication." *The Bell system technical journal*, *27*(3), 379–423.

Sherwood, S., Roca, R., Weckwerth, T., and Andronova, N. (2010). "Tropospheric water vapor, convection, and climate." *Reviews of Geophysics*, *48*(2).

Silva, D. R., Peck, A. B., and Soifer, B. T. (2010). "Observatory operations: Strategies, processes, and systems iii." *Observatory Operations: Strategies, Processes, and Systems III*, *7737*.

Smith, S. W., et al. (1997). "The scientist and engineer's guide to digital signal processing."

Solomon, S., Manning, M., Marquis, M., Qin, D., et al. (2007). *Climate change 2007-the physical science basis: Working group I contribution to the fourth assessment report of the IPCC*, vol. 4. Cambridge university press.

Staelin, D., Barrett, A., Waters, J., Barath, F., Johnston, E. J., Rosenkranz, P., Gaut, N., and Lenoir, W. (1973). "Microwave spectrometer on the nimbus 5 satellite: meteorological and geophysical data." *Science*, *182*(4119), 1339–1341.

Stiller, G., Kiefer, M., Eckert, E., Von Clarmann, T., Kellmann, S., García-Comas, M., Funke, B., Leblanc, T., Fetzer, E., Froidevaux, L., et al. (2012). "Validation of mipas

imk/iaa temperature, water vapor, and ozone profiles with mohave-2009 campaign measurements." *Atmospheric Measurement Techniques*, 5(2), 289–320.

Stomp, M., Huisman, J., Stal, L. J., and Matthijs, H. C. (2007). "Colorful niches of phototrophic microorganisms shaped by vibrations of the water molecule." *The ISME journal*, 1(4), 271–282.

Straub, C., Murk, A., and Kämpfer, N. (2010). "Miawara-c, a new ground based water vapor radiometer for measurement campaigns." *Atmospheric Measurement Techniques*, 3(5), 1271–1285.

Straub, C., Murk, A., Kämpfer, N., Golchert, S. H., Hochschild, G., Hallgren, K., and Hartogh, P. (2011). "Aris-campaign: intercomparison of three ground based 22 ghz radiometers for middle atmospheric water vapor at the zugspitze in winter 2009." *Atmospheric Measurement Techniques*, 4(9), 1979–1994.

Studer, S., Hocke, K., and Kämpfer, N. (2012). "Intraseasonal oscillations of stratospheric ozone above switzerland." *Journal of atmospheric and solar-terrestrial physics*, 74, 189–198.

Susskind, J., Barnet, C. D., and Blaisdell, J. M. (2003). "Retrieval of atmospheric and surface parameters from airs/amsu/hsb data in the presence of clouds." *IEEE Transactions on Geoscience and Remote Sensing*, 41(2), 390–409.

Thompson, A. R., Moran, J. M., and Swenson, G. W. (2017). *Interferometry and synthesis in radio astronomy*. Springer Nature.

Tiuri, M. (1964). "Radio astronomy receivers." *IEEE Transactions on Military Electronics*, 8(3), 264–272.

Trimberger, S. M. S. (2018). "Three ages of fpgas: a retrospective on the first thirty years of fpga technology: this paper reflects on how moore's law has driven the design of fpgas through three epochs: the age of invention, the age of expansion, and the age of accumulation." *IEEE Solid-State Circuits Magazine*, 10(2), 16–29.

Tschanz, B., Straub, C., Scheiben, D., Walker, K., Stiller, G., and Kämpfer, N. (2013). "Validation of middle-atmospheric campaign-based water vapour measured by the ground-based microwave radiometer miawara-c." *Atmospheric Measurement Techniques*, 6(7), 1725–1745.

Ulaby, F. T., Moore, R. K., and Fung, A. K. (1981). "Microwave remote sensing: Active and passive. volume 1-microwave remote sensing fundamentals and radiometry."

Van Vleck, J. H., and Weisskopf, V. F. (1945). "On the shape of collision-broadened lines." *Reviews of Modern Physics*, 17(2-3), 227.

Wallace, J. M., and Hobbs, P. V. (2006). *Atmospheric science: an introductory survey*, vol. 92. Elsevier.

Wang, J., and Zhang, L. (2008). "Systematic errors in global radiosonde precipitable water data from comparisons with ground-based gps measurements." *Journal of Climate*, 21(10), 2218–2238.

Waters, J. W., Froidevaux, L., Harwood, R. S., Jarnot, R. F., Pickett, H. M., Read, W. G., Siegel, P. H., Cofield, R. E., Filipiak, M. J., Flower, D. A., et al. (2006). "The earth observing system microwave limb sounder (eos mls) on the aura satellite." *IEEE transactions on geoscience and remote sensing*, *44*(5), 1075–1092.

Whiteman, D., Demoz, B., Rush, K., Schwemmer, G., Gentry, B., Di Girolamo, P., Comer, J., Veselovskii, I., Evans, K., Melfi, S., et al. (2006). "Raman lidar measurements during the international h2o project. part i: Instrumentation and analysis techniques." *Journal of Atmospheric and Oceanic Technology*, *23*(2), 157–169.

Widmer, N. S., Tocci, R. J., et al. (2007). *Digital systems: Principles and applications*. Prentice Hall. Pearson Education International.

Wilheit, T. (1980). "Microwave radiometric determination of oceanographic and meteorological parameters." In *COSPAR Colloquia Series*, vol. 20, 15–20, Elsevier.

Wilheit, T. T., Chang, A., V. Rao, M., Rodgers, E., and Theon, J. (1977). "A satellite technique for quantitatively mapping rainfall rates over the oceans." *Journal of Applied Meteorology and Climatology*, *16*(5), 551–560.

Wilson, T. L., Rohlfs, K., and Hüttemeister, S. (2009). *Tools of radio astronomy*, vol. 5. Springer.

Woodhouse, I. H. (2017). *Introduction to microwave remote sensing*. CRC press.

Wulfmeyer, V., Bauer, H.-S., Grzeschik, M., Behrendt, A., Vandenberghe, F., Browell, E. V., Ismail, S., and Ferrare, R. A. (2006). "Four-dimensional variational assimilation of water vapor differential absorption lidar data: The first case study within ihop_2002." *Monthly weather review*, *134*(1), 209–230.

Xu, J., Liu, W., Bian, J., Liu, X., Yuan, W., and Wang, C. (2020). "Method for retrieval of atmospheric water vapor using oh airglow for correction of astronomical observations." *Astronomy & Astrophysics*, *639*, A29.

Yaroshenko, V. (1964). "Influence of the fluctuating factor of amplification on the measurements of weak noise-like signals." *Radiotechnica*, *7*, 749.